Electronic

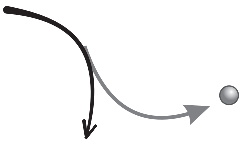

Decay

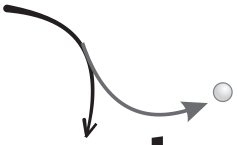

Cascades

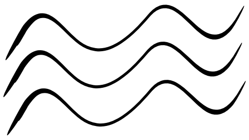

in Media
Initiated by
Resonant Absorption
of X-Ray Photons

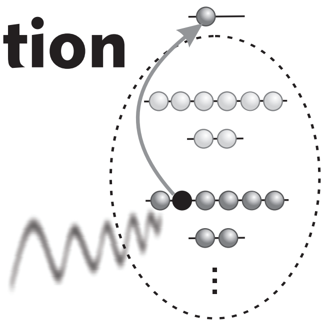

Dissertation
Tsveta Miteva
2015

Dissertation

submitted to the
Combined Faculty of Natural Sciences and Mathematics
Heidelberg University, Germany
for the degree of
Doctor of Natural Sciences (Dr. rer. nat.)

Presented by
M.Sc. in Chemistry: Tsveta Miteva
Born in: Ruse, Bulgaria
Oral examination: July 16th, 2015

Electronic Decay Cascades in Media Initiated by Resonant Absorption of X-Ray Photons

Referees: Prof. Dr. Lorenz S. Cederbaum
Prof. Dr. Jochen Schirmer

Acknowledgements

First of all, I would like to thank Prof. Lorenz Cederbaum for accepting me as a part of his group, for his guidance during my PhD, for his kind-hearted, cheerful and humorous attitude.

I thank Dr. Kirill Gokhberg for the fruitful collaboration and communication, for the numerous discussions, for his help and support throughout my PhD. I also thank him for always being patient and understanding.

I owe my deepest gratitude to Prof. Jochen Schirmer for his guidance through the scientific world, for his sincere friendship and for not missing a single day to pass by the office at 12.30 p.m. with the words "Gospojice, izglezhdash mnogo gladna." ("Miss, you look very hungry." in Bulgarian).

I thank Dr. Alex Kuleff for the scientific discussions, for his optimism, for his help, guidance, and reassurance. His easy-going and humorous personality has always been very inspiring to me.

I am much obliged to Dr. Shachar Klaiman for always generously providing his expert help and sharing his scientific knowledge at any time only in return for a chewing gum :).

The last part of my PhD project was done in collaboration with Prof. Andreas Dreuw and with Jan Wenzel. I am very grateful to them for providing me with the opportunity to be one of the first users of the CVS-ADC code developed in their group. I thank Jan for sharing his knowledge with me and for his enormous help in running the calculations and analysing the results.

I am grateful to Ghazal, Jochen, Alex, Julia, Kirill, Keyvan, Simona, and Shachar for proofreading my thesis. I would also like to thank Dr. Nicolas Sisourat, Dr. Yasen Velkov, Dr. Sören Kopelke, Dr. Ying-Chih Chiang, Vasili Stumpf, and Dr. Evgeniy Gromov. The friendly and creative atmosphere in the TC group along with the scientific expertise of all of its present and former members is unique and very stimulating. It will remain one of the best memories of my stay in Heidelberg. I am also grateful to Enzo Sconti (or "the Bellini guy" as we know him in the group) and his lovely team who have been providing the coffee essential for a PhD student.

I am very obliged to my former supervisors Prof. Alia Tadjer, Prof. Anela Ivanova and Dr. Galia Madjarova without whom I would never have come to Heidelberg. I also express my deep gratitude to my high-school chemistry teacher, Kamen Obreshkov, who stirred my enthusiasm for chemistry, and to Prof. Stefan Ivanov, from whom I've learned a lot about quantum chemistry, physics and editing scientific texts and who has always been very inspiring and supportive.

I thank Ghazal for the sincere friendship and for some of the best and most unforgettable moments during my stay in Heidelberg. I am also grateful to my friends Julia Romanova, Silviya Ninova and Momchil Ninov for their emotional support and for continuing our friendship despite the long distance between us.

Finally, I thank my mother and Kaloyan for their love, patience, understanding and support.

Abstract

The resonant-Auger – interatomic Coulombic decay (RA-ICD) cascade was recently proposed as a very efficient means of controlling the generation site and energies of slow ICD electrons. The control mechanism was verified in a series of experiments where both the energy of the photons producing the initial core excitation, and the neighbouring species were varied. The aim of this thesis is to provide a detailed theoretical investigation of the RA-ICD cascade in rare-gas dimers and give a first insight into the course of the cascade in aqueous medium.

The potential energy curves (PECs) of ionisation satellites are key ingredients in the theoretical description of electronic decay cascades. In the first chapter, we conducted a study on the PECs of the ionisation satellites of the ArHe dimer with a view to modelling such PECs in heavier dimers. Our results show that the complex valence structure in the rare-gas atom leads to the mixing of different electronic configurations of the dimer, which prevents one from assigning a single dicationic parent state to some of the ionisation satellites.

In the second part of the thesis, we present and analyse the ICD-electron and kinetic-energy-release (KER) spectra following different resonant core excitations of Ar in the rare-gas dimers Ar_2 and ArKr. We demonstrate that the manifold of ICD states populated in the resonant Auger process consists of fast- and slow-decaying ionisation satellites, and that the accurate description of nuclear dynamics in the latter ICD states is crucial for obtaining theoretical electron and KER spectra in good agreement with the experiment. We also show that by varying the neighbouring atom one can tune the energies of the emitted ICD electrons and even control the ICD yield.

Finally, as a first step towards the investigation of the RA-ICD cascade in aqueous medium, we present and discuss the X-Ray absorption spectra of micro-solvated clusters of Na^+ and Mg^{2+} at the metal 1s threshold. In this case it is important to investigate the nature of the core-excited states prior to studying the RA-ICD cascade, since in a solution the excited electron is delocalised and may ionise within the lifetime of the core hole, thus changing the course of the cascade.

Our findings show that for a complete first solvation shell, the excited electron becomes spatially extended towards the water molecules.

Kurzfassung

Ein als resonanter Auger-Interatomarer Coulombzerfall (RA-ICD) bezeichneter Kaskadenprozess wurde vor kurzem als effizienter Mechanismus für die Kontrolle der Ausgangszentren und der Energien von langsamen ICD-Elektronen vorgeschlagen. Dieser Kontroll-Mechanismus konnte in einer Reihe von Experimenten verifiziert werden, in denen sowohl die Photonenenergie zur Erzeugung der anfänglichen Core-Anregung als auch die jeweiligen Nachbar-Atome variiert wurden. In der vorliegenden Arbeit wird eine detaillierte theoretische Untersuchung der RA-ICD-Kaskade in Edelgas-Dimeren vorgestellt und ein erster Einblick in den RA-ICD-Mechanismus im flüssigen Medium gegeben.

Für die theoretische Beschreibung von elektronischen Zerfallskaskaden sind die Potentialkurven der ionischen Satellitenzustände grundlegend. Am Beispiel des ArHe-Dimers werden die Potentialkurven der Ionisierungssatelliten berechnet und analysiert, wobei auch eine Modellierung von Potentialkurven für Dimeren aus schwereren Atomen diskutiert wird. Wie unsere Ergebnisse zeigen, führt die komplexe elektronische Struktur im Valenzbereich des Edelgasatoms zu starker Mischung unterschiedlicher elektronischer Konfigurationen in den Zuständen des Dimers, so dass man einige Ionisierungssatelliten nicht einem einzigem dikationischen Ausgangszustand zuordnen kann.

Im zweiten Teil der Arbeit untersuchen wir die ICD-Elektronen- und KER-Spektren (kinetic-energy release) nach resonanter Core-Anregung von Ar in den Edelgas-Dimeren Ar_2 und ArKr. Wie wir zeigen, besteht die Vielfalt der durch den resonanten Auger-Prozess populierten ICD-Zustände in schnell oder langsam zerfallenden Ionisierungssatelliten. Eine genaue Beschreibung der Kerndynamik dieser ICD-Zustände ist erforderlich, um theoretische Elektronen- und KER-Spektren in guter Übereinstimmung mit dem Experiment zu generieren. Durch spezifische Wahl des Nachbaratoms lassen sich die Energien der emittierten ICD-Elektronen gezielt variieren und sogar die ICD-Intensitäten kontrollieren.

Als ein erster Schritt zur Untersuchung von RA-ICD-Kaskaden im flüssigen Medium werden Röntgenabsorptionsspektren von mikro-solvatiserten Na^+- und

Mg^{2+}-Clustern an der 1s-Schwelle der Metalle untersucht. Hier ist es wichtig, vor der RA-ICD-Kaskade zunächst die Core-angeregten Zustände selber zu analysieren, da in Lösung das angeregte Elektron delokalisiert und Ionisierung innerhalb der Lebenszeit des Core-Loches möglich ist. Dies ändert den Verlauf der RA-ICD-Kaskade gegenüber dem Fall der Gasphase. Unsere Resultate zeigen, dass bei vollständiger erster Solvatisierungsschale das angeregte Elektronen über die Wassermoleküle räumlich ausgedehnt ist.

Contents

1 Introduction 1

2 Theory 9

2.1 *Ab initio* methods for electronic structure calculations: application to the potential energy curves of ionisation satellites 9

2.1.1 Configuration interaction (CI) 12

2.1.2 Algebraic diagrammatic construction (ADC) 16

2.2 *Ab initio* computation of electronic decay widths 23

2.2.1 Complex absorbing potential (CAP) method 25

2.2.2 Fano-ADC-Stieltjes method 27

2.3 Time-dependent theory of wave packet propagation 31

3 Ionisation satellites of ArHe 37

3.1 Computational details 38

3.2 Results and discussion 41

3.2.1 $\mathrm{Ar}^{2+}(3p^{-2})$He parent dicationic states 41

3.2.2 $\mathrm{Ar}^{+}(3p^{-2}4s)$He ionisation satellites 43

3.2.3 Higher lying $\mathrm{Ar}^{+}(3p^{-2}5s)$He and $\mathrm{Ar}^{+}(3p^{-2}3d)$He states . . . 45

3.3 Summary and conclusions 47

4 Resonant-Auger – ICD cascade in rare-gas dimers 49

4.1 Computational details 50

4.1.1 Potential energy curves 50

4.1.2 Decay widths 52

4.1.3 Nuclear dynamics calculations 55
4.2 ICD following resonant core excitation of Ar in Ar_2 56
4.2.1 Potential energy curves of Ar_2 56
4.2.2 Nuclear dynamics during the ICD step 59
4.2.3 ICD-electron and KER spectra 62
4.3 ICD following resonant core excitation of Ar in ArKr: the role of the partner atom 70
4.3.1 Potential energy curves 70
4.3.2 Decay widths 73
4.3.3 ICD-electron and KER spectra 73
4.4 Summary and conclusions 80

5 X-Ray absorption spectra of microsolvated metal cations 85

5.1 Computational details 86
5.1.1 Geometry optimisation 86
5.1.2 Core-excitation spectra 87
5.2 Results and discussion 88
5.2.1 Bare ions (M^{q+}) 90
5.2.2 $M^{q+}(H_2O)$ clusters 92
5.2.3 $M^{q+}(H_2O)_2$ clusters 97
5.2.4 $M^{q+}(H_2O)_{3-5}$ clusters 101
5.2.5 $M^{q+}(H_2O)_6$ clusters 105
5.3 Summary and conclusions 108

Appendices 111

A Rydberg states of cations 113

A.1 General formalism 113
A.2 Spin-adapted configurations 119

B ADC(2)/ISR method for properties of dicationic states 125

B.1 Derivation of the ISR(2) equations 125

B.2 Dicationic ISR(2) expressions for one-particle operators 129

References 133

List of notations

$\|\Psi_0\rangle$	exact/correlated electronic ground state
$\|\Phi_0\rangle$	Hartree-Fock ground state
ϵ_i	Hartree-Fock orbital energies
$\|\phi_i\rangle$	one-particle Hartree-Fock states
$c_i^\dagger(c_i)$	creation (annihilation) operators related to the Hartree-Fock one-particle states $\|\phi_i\rangle$
$E_0^{(0)}$	expectation value of the Hartree-Fock Hamiltonian with respect to the Hartree-Fock ground state
E_0, E_0^N	exact ground-state energy of the N-electron system
$E_0(1)$	Hartree-Fock ground-state energy
$i, j, k \dots$	indices referring to occupied Hartree-Fock orbitals
$a, b, c \dots$	indices referring to unoccupied Hartree-Fock orbitals
$p, q, r \dots$	general indices referring to both occupied and unoccupied Hartree-Fock orbitals

Chapter 1

Introduction

Radiation with sufficiently high energy can excite or ionise an electronic system, such as an atom or a molecule. The excited or ionised system subsequently relaxes by emitting photons, electrons, or by processes involving nuclear dynamics. The relaxation pathway depends on many factors, for example, on the nature and energy of the excited state, on the available final states, on symmetry and spin selection rules, etc. In the case of core-excited or -ionised atoms and molecules, there are two possible decay channels – non-radiative Auger decay and radiative decay [1]. In the Auger process, the core hole is filled by an outer electron and an electron of high kinetic energy is emitted within femtoseconds. For heavier elements, emission of an X-Ray photon is the dominant decay channel, while the light elements usually relax via Auger decay, i.e. by emission of electrons [2].

In the case of the valence-excited or -ionised states of isolated species typically only the relaxation by emitting a photon is energetically open. Importantly, this radiative decay takes place usually on the nanosecond timescale [3]. The situation is, however, very different when the excited or ionised system is embedded in an environment, where an additional decay channel involving the neighbouring species from the environment becomes operative. This novel relaxation pathway, termed interatomic/intermolecular Coulombic decay (ICD) was first predicted theoretically by Cederbaum and co-workers in 1997 [4]. In this process, the initially excited or ionised species relaxes by transferring its excess energy to the neighbour, thus, ionising it.

Since the discovery of ICD, many experimental and theoretical studies have focused on both the systems in which it can occur and the processes which can trigger it. Thus, ICD was found to be a very general de-excitation process inherent in weakly-bound matter, like rare-gas clusters [5, 6], hydrogen-bonded clusters [4, 7, 8], endohedral fullerenes [9], or even quantum dots [10, 11]. Moreover, it was found that ICD is a very efficient process [12, 13] taking place on a femtosecond timescale [14, 15], therefore, outpacing the radiative decay and in some cases even competing with Auger decay [16, 17]. The generality of ICD is also manifested in the variety of processes that can initiate it. Thus, it was found that ICD can occur upon irradiation with photons [6], ion [18, 19] and electron bombardment [20, 21], or as one of the stages of complex decay cascades, for example, after Auger decay [22–24].

In addition to its diversity, ICD has attracted attention also with its potential applications. For example, ICD following photoionisation has already been successfully used as a spectroscopic tool to retrieve structural information [25]. This novel application of ICD relies on competing ICD processes of an inner-valence ionised species with different neighbours. Fasshauer *et al.* [25] demonstrated on the example of large clusters of Ar and Ne that the kinetic-energy distribution of the emitted slow ICD electrons following inner-valence ionisation of Ne can be used to identify the structure of the clusters.

Biology is another field where ICD can be of great importance. Living cells and tissues are constituted of a bounty of chemical species, functioning in aqueous environment and often through interaction with light. Moreover, since most of these species participate in hydrogen-bonded networks or coordination complexes, where ICD is abundant [4, 7, 8, 26, 27], they indisputably are the perfect candidates for undergoing ICD and related processes. For example, it was shown that the process behind the DNA repair function of the enzyme photolyase is ICD [13]. The authors also discuss that the quantum yield of this process is close to unity, implying the high efficiency of ICD in a biological system. Being omnipresent in hydrogen-bonded species [26], ICD, producing low-energy electrons and radical cations, naturally contributes also to the radiation-induced damage in biological matter. Indeed, the low-energy electrons and radical cations are known to be genotoxic agents effectively damaging DNA [28–30]. For this reason, a large part of the recent scientific research on ICD and ICD-like processes has been focused on their biological impact [7, 8, 13, 26, 31–33]. This interest is driven not only by the desire to understand the fundamental processes causing DNA damage, but also to learn how to control these elementary decay mechanisms. An interesting example along this line is the possibility to switch ICD on and off by varying the pH of the medium [34]. Such control schemes offer a potential use of ICD in radiation-based cancer therapies as a means of controlled radiation damage and targeted release of low-energy electrons and radicals using molecular and nanoparticle targets [29].

It has been demonstrated that radiation damage can be crucial to macromolecular crystallography, where X-Rays are employed for structural characterisation of macromolecules [30, 35]. Upon irradiation of protein crystals with X-Ray photons, the obtained photoelectrons and radicals can initiate chemical reactions [30, 35]. Usually these reactions cause specific damage such as ablation of carboxylate groups, cleavage of disulfide bonds and reduction of metal centres. In the case of enzymes, for example, different oxidation states of the metal centre result in different coordination of the ion implying that the stereochemistry of the macromolecule changes upon radiation [35]. Consequently, studying the response of loosely bound metal ions to high-energy radiation can elucidate the precise mechanisms of radiation damage. The effect of ionising radiation on solvated metal ions has already been reported in the literature [16, 17]. Pokapanich *et al.* measured the Auger spectra of aqueous K^+ and Ca^{2+}. The authors observe that the interaction of the metal ions with the surrounding medium leads not only to large chemical shifts of the peaks in the Auger spectra, but also to the appearance of additional peaks from the competing core-like ICD process, which will inevitably generate slow electrons and reactive cations.

In most of the cases discussed above, ICD is initiated by ionising radiation. In a polyatomic system, such radiation can ionise all atoms with ionisation potentials below the energy of the impacting photons, implying that one cannot selectively initiate ICD at a particular location. This poses the intriguing question whether one can exercise control over the course of ICD, its location and the energies of the emitted genotoxic radical cations and slow electrons, and thus use ICD as a source of controlled radiation damage.

A very efficient means of controlling the ICD process suggested recently by Gokhberg *et al.*, utilises resonant core excitation to trigger ICD [32]. The so-called resonant-Auger – ICD (RA-ICD) cascade (see Fig. 1.1) is very attractive for its site- and energy-selectivity. The site-selectivity of the process is achieved by adjusting the energy of the initial photon in order to excite specific atoms in a large molecule. This highly energetic core-excited state will then undergo Auger decay, whereby a valence electron fills the initial vacancy and another valence electron is emitted. The latter mechanism is called “spectator” Auger decay and it produces ionised-excited satellite final states [37]. In the alternative, “participator”, process

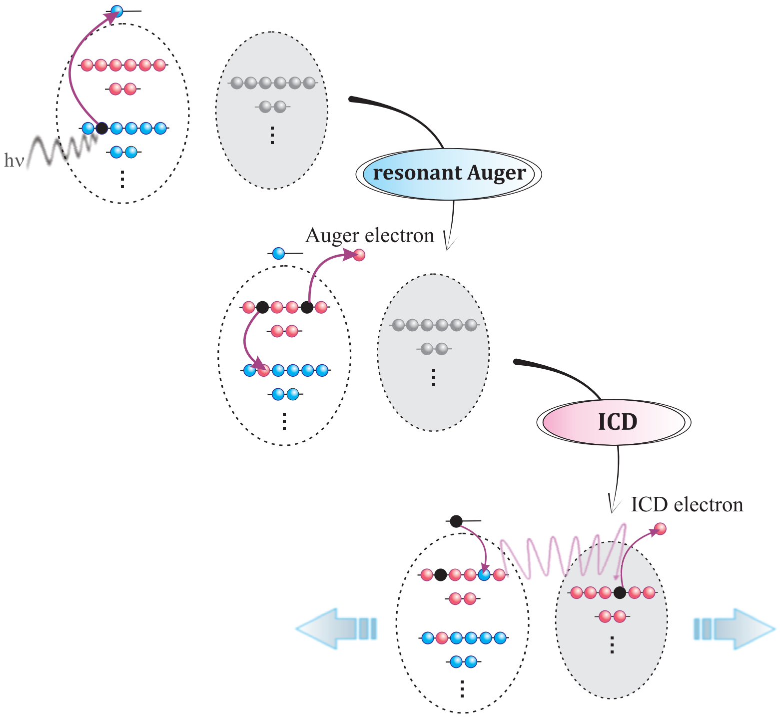

Figure 1.1: Schematic representation of the resonant-Auger – ICD decay cascade: (a) resonant core excitation of Ar, resulting in the population of Ar($2p^{-1}nl$)Ar state. (b) subsequent resonant Auger decay proceeding mostly according to the spectator model [36] in which the excited electron does not participate in the decay process. The excited electron can also hop to a higher virtual orbital (shake-up process). The final states are ionised-excited states of two-hole-one-particle (2h-1p) character: Ar($3p^{-2}n'l'$)Ar. (c) The majority of the final states of the resonant Auger process undergo interatomic Coulombic decay, in which the excited electron de-excites and the excess energy is transferred to the neighbour, thus ionising it. The final states of the ICD process are two-site dicationic states Ar^{+}($3p^{-1}$)Ar^{+}($3p^{-1}$). Due to the repulsion between the charges, the system fragments in a Coulomb explosion.

the initially excited electron participates in the decay, which results in final states with a hole in the inner- or outer-valence shell, the so-called main states [37]. For the core-excited states considered in this work, the latter process was shown to be the less efficient de-excitation pathway [37, 38], therefore, only the spectator Auger decay will be considered.

The resonant excitation of core electrons is a very sensitive probe of local electronic properties as evidenced by selective excitation of electrons localised on identical atoms placed in different chemical environment [39] and also by the X-

Ray absorption spectra of rare-gas clusters and solids at the Ne and Ar K-edges [40–42]. Hence, the photon energy deposition and the following ICD step happen at a specified location. Moreover, since the excitation proceeds resonantly, by tuning the incident photon energy a core electron can be controllably promoted to different virtual orbitals. This will result in the population of different satellite states in the resonant Auger process [38, 43], and their subsequent interatomic decay will lead to different distributions of ICD electrons.

After its prediction, the RA-ICD cascade has been experimentally observed in the nitrogen and carbon monoxide dimers following core excitation at the oxygen and nitrogen K-edges [44], and in Ar-containing rare-gas dimers following excitation from the Ar $2p$ level [45–47]. The detailed experimental studies of the process in Ar_2, ArKr, ArXe, and ArNe demonstrated the functioning of the control mechanism [45–47]. In these experiments the cascade was initiated by resonant photon excitation of a $2p$ core electron of Ar to the $4s$ or the nd $(n = 3, 4, 5)$ virtual orbital. The resulting ICD-electron spectra indeed show marked dependence on the parent core excitation. For example, the spectra obtained in Ar_2, ArKr, and ArXe following $\mathrm{Ar}(2p_{3/2} \to 4s)$ excitation show a pronounced peak between 0 and 2 eV and a weaker peak between 2.5 and 4 eV, while the spectra obtained following $\mathrm{Ar}(2p_{3/2} \to 3d)$ excitation have a characteristic double-peak structure shifted to higher energies [47]. The difference is due to the larger probability of shake-up processes in the resonant Auger decay of the $2p_{3/2} \to 3d$ excitation of Ar [36, 38, 48] leading to a noticeable population (up to 60%) of higher lying $\mathrm{Ar}^+(3p^{-2}4d, 5d)$ satellite states.

The distribution of ICD electron energies can be qualitatively obtained using a simple model, where one assumes no interaction between atoms in the satellite states, pure Coulomb repulsion in the final states, and instantaneous decay [32]. Therefore, only readily available energies of different states of Ar^+ and the ground state equilibrium distance of the corresponding dimer are necessary for computing ICD spectra. However, in Ar_2 such qualitative approach overestimates the energies of ICD electrons deriving from the decay of higher-lying satellites [45]. Moreover, the observed kinetic-energy-release (KER) spectra show a complicated structure indicative of nuclear dynamics taking place during the decay. Thus, if one wishes to achieve a more detailed understanding of the resonant-Auger – ICD cascade, both accurate potential energy curves (PECs) and accounting for the nuclear motion are indispensable.

For this reason, one of the major goals of this work is to perform a full quantum dynamical description of the RA-ICD cascade and thus to study what role the accurate interaction energies in the decaying and final states of ICD and the nuclear dynamics during the decay play in shaping the ICD-electron and KER spectra. Within this thesis such a study was performed in two rare-gas dimers, Ar_2 and ArKr. For the full quantum mechanical simulation of the dynamics one needs accurate *ab initio* potential energy curves and ICD widths as an input. The methodology used for obtaining the PECs of the investigated systems is outlined in Chapter 2. The computation of the decay widths and the theory of wave packet propagation as applied to the case of the RA-ICD cascade are presented in Chapter 2. The computational details as well as the results and discussion of the ICD-electron and KER spectra following the $Ar(2p \to 3d, 4s)$ core excitations in Ar_2 and ArKr are given in Chapter 4.

The structure of the ICD-electron and KER spectra depends not only on the specific manifold of decaying states, but also on the nature of the neighbouring species. Experimental studies of the role of the partner atom in the RA-ICD cascade confirm that the partner atom's choice can influence the ICD emission [47] and, moreover, that it can serve as a switch for particular decay channels [45]. In Chapter 4 we also present for the first time a detailed theoretical investigation of the effect of a chemically "softer" neighbour on the ICD spectra. To this end, we compare the theoretical ICD spectra of ArKr and Ar_2 produced in the RA-ICD cascade following the $2p_{3/2} \to 4s$, $2p_{1/2} \to 4s$ and $2p_{3/2} \to 3d$ core excitations of Ar. We also compared our theoretical results with the available experimental data [47, 49] and with the theoretical spectra in Ref. [32] obtained using a simple model of the cascade.

The sensitivity of the RA-ICD cascade to the energy of the initial photon as well as to the neighbours surrounding the core-excited species can be used for structural analysis of large mixed rare-gas clusters. It is known that the core-excitation energies of rare-gas clusters depend both on the cluster size and on the location of the atoms in the cluster [41, 42]. Consequently, using a resonant core excitation, it is possible to selectively trigger ICD at different sites in the clusters – on the surface, in the bulk or at interfaces. The combination of the site-selective resonant core excitation and the neighbour-dependent ICD process can find an application as a very accurate and powerful tool for spectroscopic characterisation of clusters.

In the theoretical description of the RA-ICD cascade in dimers, we assume that the resonant Auger process is of local nature, i.e. not influenced by the presence of a neighbour. Indeed, experimental studies on both the X-Ray absorption (XAS) spectra and on the RA-ICD process in dimers have confirmed that this assumption is valid [46, 50]. The situation, however, changes if the core-excited species is embedded in an environment. The effect of the surrounding medium on the core-excitation spectra and on the course of the subsequent relaxation in noble-gas clusters has been the subject of several experimental studies [40, 42]. First, it has been shown that the energies of the resonant core excitations depend on the positions of the atoms in the cluster (on the surface or in the bulk) and on the cluster-size, reaching up to ∼1 eV deviation from the atomic values [42]. Second, it has been observed that the resonant Auger spectra following the decay of higher core-excited states deviate significantly from the atomic spectra [40]. This is attributed to the delocalisation of the excited electron which occurs due to the interaction with the environment and is more probable for higher-excited states due to the larger spatial extent of the higher virtual orbitals. Thus, instead of the resonant Auger decay, normal Auger decay occurs.

In a solution, the effect of the environment on both the core-excitation spectra and on the course of the subsequent decay process is expected to be even more pronounced due to the stronger interactions between the excited species and the solvent molecules. Thus, analogously to the case of rare-gas clusters and solids, the resonant Auger decay will compete with the process of delocalisation of the excited electron. Measurements of the rate of delocalisation in liquid water and ice at the oxygen K-edge using the method of the core-hole clock, indeed evidence that the delocalisation is very fast, <500 as [51]. It is thus clear that the course of an electronic decay cascade initiated by resonant photoabsorption will be determined by the competition between the processes of delocalisation and autoionisation. Consequently, prior to studying the decay cascade, one should clarify the problem of delocalisation and subsequent solvation of the core-excited electron.

In the last part of this thesis we present a first attempt to clarify the presence of the solvent affects the properties of core-excited states. To this end, we computed and analysed the X-Ray absorption spectra of microsolvated clusters of Na^+ and Mg^{2+} with different coordination numbers $n = 1 - 6$ at the metal K-edge. The choice of two isoelectronic metal ions with different charges aims at clarifying whether the degree of delocalisation of the excited electron depends on the charge of the central ion. This idea was motivated by experimental and theoretical studies on the Auger spectra of aqueous K^+ and Ca^{2+}, which demonstrate that the chemical shifts in the Auger spectra of the solvated K^+ and Ca^{2+} ions depend strongly on the charge [17]. The authors explain the observed differences in the chemical shifts with the larger ion-dipole interactions and the influence of the second and higher solvation shells in the case of Ca^{2+}. Our analysis of the X-Ray absorption spectra of the microsolvated clusters of Na^+ and Mg^{2+} is based on comparison with the spectra of the bare metal ions. Additionally, in order to determine the character of the excited states in the solvated systems, we consider the overlaps of the singly-occupied natural orbitals occupied by the excited electron in the core-excited states of the clusters with the respective singly-occupied natural orbitals of the bare ions.

The thesis is organised as follows. In the next chapter, we present an overview of the computational methods used for the electronic-structure calculations and for the calculation of decay widths. We also outline briefly the time-dependent theory of wave-packet propagation as applied to the case of the RA-ICD cascade. In Chapter 3, we present and discuss the potential energy curves of the ionisation satellites of ArHe with a view to modelling such potential energy curves in heavier noble-gas dimers. Chapter 4 contains our theoretical study on the RA-ICD cascade in rare-gas dimers. Finally, in Chapter 5, we present and analyse the X-Ray absorption spectra of microsolvated clusters of Na^+ and Mg^{2+} at the metal 1s threshold. The conclusions are given separately at the end of each chapter.

Chapter 2

Theory

The quantitative theoretical description of the resonant-Auger – ICD cascade requires the simulation of the kinetic energy distributions of the emitted ICD electrons and ionic fragments. The ICD-electron and kinetic-energy-release (KER) spectra can be obtained by taking into account the nuclear dynamics during the ICD step. Since the resonant Auger process is much faster, it is assumed that very little nuclear dynamics take place and, therefore, the latter are not explicitly accounted for in the calculations. In order to compute the ICD-electron and KER spectra, the potential energy curves (PECs) of the ground state, the initial and final ICD states, as well as the decay widths of all decaying states have to be available. These data serve as input for the nuclear dynamics calculation. In the following sections the computational tools necessary for the description of the decay cascade will be outlined. In Sec. 2.1 an overview of the methods used for electronic structure calculations will be presented. The *ab initio* methods used for the computation of electronic decay widths are discussed in Sec. 2.2. Finally, Sec. 2.3 outlines the time-dependent theory of wave packet propagation and the calculation of ICD-electron and KER spectra.

2.1 *Ab initio* methods for electronic structure calculations: application to the potential energy curves of ionisation satellites

The theoretical description of electronically excited states can often be intricate, time-consuming and very involved, due to, e.g. the multiconfigurational character of the states, the high energy of the states, the size of the systems of interest, the need to describe short- and long-range interactions, etc. Thus, the proper description of such states requires the use of correlated methods (often multiconfigurational) and specifically designed basis sets [52].

In order to discuss the methods suitable for the description of excited states, it is instructive to discuss the Hartree-Fock (HF) method first, as it is the usual starting point of all correlated methods. Within the HF approximation the N-electron problem

$$\hat{H}|\Psi_0\rangle = E_0|\Psi_0\rangle \tag{2.1.1}$$

splits into one-electron problems

$$(\hat{h} + \upsilon^{HF}[\phi_1, \dots \phi_M])|\phi_p\rangle = \epsilon_p|\phi_p\rangle, \; p = 1, 2, \dots M \tag{2.1.2}$$

by assuming that each electron experiences an effective potential $\upsilon^{HF}[\phi_1, \dots \phi_M]$ obtained by averaging over the interactions with the other electrons [53]. Note, that the potential υ^{HF} depends on all spin orbitals $\{\phi_1, \dots \phi_M\}$, which means that the HF equations have to be solved iteratively. After solving the HF equations (Eq. (2.1.2)) one obtains a set of HF one-electron energies $\{\epsilon_p\}$ and spin orbitals $\{\phi_p\}$. The ground state of the system is then represented by a single Slater determinant formed from the energetically lowest N spin orbitals

$$|\Phi_0\rangle = |\phi_1\phi_2\phi_3 ... \phi_N\rangle \tag{2.1.3}$$

The expectation value of the HF Hamiltonian $\hat{H}_0$ with respect to $|\Phi_0\rangle$ gives a sum of the one-electron energies, ϵ_i (also called orbital energies)

$$E_0^{(0)} = \langle\Phi_0|\hat{H}_0|\Phi_0\rangle = \sum_{i=1}^{N} \epsilon_i \tag{2.1.4}$$

However, the ground state HF energy is the expectation value of the Hamiltonian $\hat{H}$ with respect to the Hartree-Fock ground state $|\Phi_0\rangle$

$$E_0(1) = \langle\Phi_0|\hat{H}|\Phi_0\rangle = E_0^{(0)} + E_0^{(1)} \tag{2.1.5}$$

and as such it includes an additional first-order term $E_0^{(1)}$. Within a given basis set, the Hartree-Fock approach provides the best (lowest-energy) Slater determinant. The method is variational, which guarantees that the energy $E_0(1)$ is higher than the exact energy E_0 within the given basis set. The difference between these two energies is termed “electron correlation energy” [53]

$$E_{corr} = E_0 - E_0(1) \tag{2.1.6}$$

Despite being only ~1% of the total energy E_0 [54], the correlation energy is crucial for the description of chemical phenomena.

Let us take a closer look at the notion of electron correlation. As implied by Eq. (2.1.6), electron correlation refers to the electron-electron interactions *ignored* in the HF method, i.e. it is a measure of the errors inherent in HF or other orbital models. To account for these effects, one has to go beyond the single-determinant representation of the electronic wave function

$$|\Psi_0\rangle = \sum_I a_I |\Phi_I\rangle \tag{2.1.7}$$

where the sum includes the HF ground state configuration $|\Phi_0\rangle$, and the remaining configurations $|\Phi_I\rangle$ are obtained from $|\Phi_0\rangle$ by replacing one, two, etc. occupied spin orbitals with virtual spin orbitals. Often electron correlation effects are divided into dynamical and static (or non-dynamical). Dynamical correlation refers to *the correlated motion of electrons induced by their instantaneous repulsion.* While the antisymmetry inherent in a single Slater determinant already makes electrons of opposite spins partially correlated, the motion of electrons of the same spin remains uncorrelated. For this reason, in the HF method the electrons appear to be closer than they actually are. The dynamic electron correlation can be accounted for by constructing the wave function as a superposition of configurations (similar to Eq. (2.1.7)) with the HF ground state as the dominant configuration [55, 56]. Among the most important quantum-chemical methods elaborated to account for the dynamical correlation are the configuration interaction (CI) method, the coupled-cluster (CC) method, Møller-Plesset perturbation theory (MP), propagator methods (e.g. the algebraic diagrammatic construction (ADC) method), etc.

There are also many cases when such methods are not useful because the HF reference configuration does not provide a qualitatively correct description of the system. Such correlation effects are known as static correlation, or near-degeneracy effect. They are not related to electron motion and the instantaneous repulsion between electrons, but rather to the *strong configuration interaction between several configurations.* As a result, the latter cannot be treated separately from each other. This effect is observed in the molecular dissociation limit, where the multi-configuration description of the system arises from the degeneracy of bonding and antibonding configurations [56]. Quantum-chemical methods specifically designed to account for static correlation are the multi-reference configuration interaction (MRCI), the multi-configurational self-consistent field (MCSCF) method, the complete active space SCF (CASSCF) method, etc.

A clear distinction between the two types of correlation, dynamical and static, cannot be drawn except in the limit of complete dissociation, where there is no Coulomb repulsion between the electrons but only static correlation. At the intermediate distances, however, the two types of correlation are already accounted for by constructing the wave function as a linear combination of several configurations [55, 56].

The focus of this work are excited states of ionised systems. The proper description of such states requires the use of methods accounting for electron correlation. The correlated methods specifically designed for the computation of excited states can be divided into three groups: single-configuration *ab initio* methods, multi-configuration *ab initio* methods and methods based on Density Functional theory (DFT). The first group comprises CI, propagator and coupled-cluster approaches. MRCI, MCSCF, and CASSCF fall into the second group. The third group includes the time-dependent DFT (TD-DFT) approaches. An overview of these approaches can be found in Ref. [52].

In the following subsections, two of the methods, namely CI and ADC will be discussed. The (MR-)CI method is suitable for the treatment of multi-reference problems, such as the description of ionised-excited states. Besides, it also allows one to compute hundreds of roots of the electronic Hamiltonian, which is necessary due to the large number and the high energy of the ionised-excited states of interest. A variant of the ADC(2)-x method for the polarisation propagator, employing the core-valence separation to the ADC(2) working equations (CVS-ADC(2)-x), is used to compute energies and properties of core-excited states.

2.1.1 Configuration interaction (CI)

Configuration interaction (CI) is a general procedure for finding approximate solutions to the electronic Schrödinger equation (Eq. (2.1.1)). It consists in expanding the N-electron wave function $|\Psi\rangle$ in a basis set of N-electron states $\{|\Phi_I\rangle\}$:

$$|\Psi\rangle = \sum_{I}^{N_{dim}} a_I |\Phi_I\rangle \tag{2.1.8}$$

where N_{dim} is the dimension of the basis $\{|\Phi_I\rangle\}$. The coefficients $\{a_I\}$ are determined variationally by requiring the expectation value of the Hamiltonian with respect to $|\Psi\rangle$ to have a minimum

$$E^{trial} = \frac{\langle\Psi|\hat{H}|\Psi\rangle}{\langle\Psi|\Psi\rangle} \tag{2.1.9}$$

The condition for a minimum

$$\frac{\partial E^{trial}}{\partial \mathbf{a}} = \mathbf{0}$$

results in the standard hermitian eigenvalue problem

$$\mathbf{H}\mathbf{a}^k = E_k \mathbf{a}^k \tag{2.1.10}$$

where $\mathbf{H}$ is the matrix of elements $H_{IJ} = \langle\Phi_I|\hat{H}|\Phi_J\rangle$. The lowest-energy solution corresponds to the ground state, whereas the higher-energy solutions correspond to the excited states.

If all possible expansion functions $\{|\Phi_I\rangle\}$ are included in the expansion Eq. (2.1.8), the full CI (FCI) wave function is obtained. The solutions to the matrix eigenvalue problem then correspond to the exact solutions of the Schrödinger equation within the chosen orbital basis set. Since the FCI expansion grows approximately as n^N for N electrons and n molecular orbitals, in practice, the FCI method is applicable only to small systems and for relatively small basis sets [57]. A remedy to this problem is to generate approximations by truncating the CI expansion Eq. (2.1.8). For this purpose, one needs to consider how the expansion functions $\{|\Phi_I\rangle\}$ are obtained.

Let us assume that a Hartree-Fock calculation for the system has been carried out and a set of optimised spin orbitals $|\phi_p\rangle$, $p = 1, 2, ..., M$ has been obtained. Let us also assume that the ground state of the system is adequately represented by the Hartree-Fock wave function $|\Phi_0\rangle$. One can obtain multiple Slater determinants from the reference configuration $|\Phi_0\rangle$ by substituting an occupied orbital with the remaining $M - N$ virtual spin orbitals. These Slater determinants can be classified as singly, doubly, triply, etc. excited, if they differ from $|\Phi_0\rangle$ by one, two, three, etc. spin orbitals. The set of all such determinants can be used as a basis in which the exact wave function $|\Psi\rangle$ can be represented. If one uses all possible determinants $\{|\Phi_I\rangle\}$, the representation is *exact* within the given atomic basis set

$$|\Psi\rangle = a_0|\Phi_0\rangle + \sum_{i,a} a_i^a|\Phi_i^a\rangle + \sum_{i<j,a<b} a_{ij}^{ab}|\Phi_{ij}^{ab}\rangle + \sum_{\substack{i<j<k,\\ a<b<c}} a_{ijk}^{abc}|\Phi_{ijk}^{abc}\rangle + \ldots \tag{2.1.11}$$

$$\begin{array}{cc} & \begin{array}{cccccc} |\Phi_0\rangle & |S\rangle & |D\rangle & |T\rangle & |Q\rangle & \cdots \end{array} \\ \begin{array}{c} \langle\Phi_0| \\ \langle S| \\ \langle D| \\ \langle T| \\ \langle Q| \\ \vdots \end{array} & \left(\begin{array}{cccccc} E_0 & \mathbf{0} & \langle\Phi_0|\hat{H}|D\rangle & \mathbf{0} & \mathbf{0} & \cdots \\ & \langle S|\hat{H}|S\rangle & \langle S|\hat{H}|D\rangle & \langle S|\hat{H}|T\rangle & \mathbf{0} & \cdots \\ & & \langle D|\hat{H}|D\rangle & \langle D|\hat{H}|T\rangle & \langle D|\hat{H}|Q\rangle & \cdots \\ & & & \langle T|\hat{H}|T\rangle & \langle T|\hat{H}|Q\rangle & \cdots \\ & & & & \langle Q|\hat{H}|Q\rangle & \cdots \\ & & & & & \ddots \end{array}\right) \end{array}$$

Figure 2.1: Structure of the full CI matrix. The matrix is hermitian, therefore, only the upper triangle is shown. The multitudes of singly, doubly, triply, etc. excited determinants are denoted as $|S\rangle$, $|D\rangle$, $|T\rangle$, etc.

The N-electron expansion functions are usually chosen to be either primitive Slater determinants or configuration state functions (CSFs). CSFs are linear combinations of Slater determinants which have the same spatial orbital occupations and are eigenfunctions of the total spin operator $\hat{S}^2$, and the spin projection along the z-axis $\hat{S}_z$

$$\hat{S}^2|k; S, M_S\rangle = S(S+1)|k; S, M_S\rangle \tag{2.1.12}$$

$$\hat{S}_z|k; S, M_S\rangle = M_S|k; S, M_S\rangle, \ M_S = -S, -S+1, \ldots, S \tag{2.1.13}$$

where $|k; S, M_S\rangle$ is the k-th CSF characterised by the spin quantum number S and the magnetic spin quantum number M_S [53, 57]. Both the determinantal and the CSF expansions are used in different CI implementations. An overview of the differences between the two formulations can be found in Ref. [57].

Eq. (2.1.11) gives the form of the FCI wave function. Using this expansion one can construct the FCI matrix of the Hamiltonian (see Fig. 2.1). As can be seen on Fig. 2.1, there is no coupling between the ground state and the singly excited states (Brillouin's theorem). Also according to the rules for evaluation of matrix elements (known as Slater-Condon rules), the elements $\langle\Phi_I|\hat{H}|\Phi_J\rangle$ vanish if the two configurations $|\Phi_I\rangle$ and $|\Phi_J\rangle$ differ by more than two spin orbitals. Therefore, some of the blocks of the CI matrix are very sparse, and others vanish completely. Successive truncations of the wave function can be obtained by neglecting all excitations beyond a given excitation class. If only singly-excited determinants (or CSFs) are included, the method is termed Configuration Interaction Singles (CIS); the inclusion of singles (S) and doubles (D) leads to CISD, etc. Apart from neglecting some of the correlation energy, the truncated CI methods are not size-consistent, i.e. the energy of a molecule dissociated into two or more parts, treated as one system, does not equal the sum of the energies of the subsystems computed with the same method [57, 58]. In the case of CISD, various corrections accounting for this shortcoming were elaborated. Very widely used is the Davidson correction, which estimates the contribution of the missing quadruple excitations. It is calculated as

$$E_{DC} = (1 - a_0^2)(E_{CISD} - E_{HF}) \tag{2.1.14}$$

where a_0 is the weight of the HF wave function in the CISD expansion. A comprehensive description of the various corrections can be found in Ref. [57]. An advantage of the truncated CI methods is that the approximate energies, obtained using a truncated CI method, are always higher than the FCI solutions, and the convergence to the exact values occurs monotonically with increasing wave function expansion (N_{dim})

$$E_k^{(\mathrm{FCI})} \leq E_k^{(N_{dim})} \tag{2.1.15}$$

$$E_k^{(N_{dim})} \leq E_{k+1}^{(N_{dim}+1)} \leq E_{k+1}^{(N_{dim})} \tag{2.1.16}$$

where N_{dim} is the size of the basis set (see Eq. (2.1.8)), and the eigenvalues are ordered in increasing energy. These properties of the CI methods are satisfied at each molecular conformation, thus they apply not only to the particular conformation, but also to the behaviour of the entire potential energy surface [57].

In the discussion so far it was assumed that the ground state of the system is well represented by a single Slater determinant. However, in many cases an adequate description of the ground state is achieved by taking several determinants as reference configurations. The multi-reference CI (MRCI) does not use a single Hartree-Fock reference, but a suitably chosen set of configurations. They can be generated either in a preceding MCSCF calculation or simply using Hartree-Fock Slater determinants. The general form of the multi-reference wave function is

$$|\Psi\rangle = \sum_m a_m |\Phi(m)\rangle + \sum_m \sum_{i,a} a_i^a |\Phi(m)_i^a\rangle + \ldots \tag{2.1.17}$$

where $\{|\Phi(m)\rangle,\ m = 1, \ldots, N_{ref}\}$ represent the set of reference functions. The expansion space is generated from this set by applying the excitation operators to every single reference configuration. Similarly to the CI method, the wave function can be truncated to reduce the sizes of the configuration spaces. The methods used in this work are MRCI-SD and MRCI-SDT with Hartree-Fock Slater determinants as reference configurations.

2.1.2 Algebraic diagrammatic construction (ADC)

An alternative approach to the description of excited states are the Green's function or propagator methods [59]. Within these methods the energies of the excited states represent the poles of the Green's function, and the spectral intensities are obtained from the corresponding residues. There exist perturbation expansions for the Green's function **G** in terms of Feynman diagrams. These expansions can be used for the construction of approximation schemes. One such scheme is the algebraic diagrammatic construction (ADC) method which will be discussed in the following.

Consider the electron propagator, also known as one-particle Green's function, which is a means of calculating the electron ionisation and attachment spectra of finite electronic systems [59, 60]. In order to derive its ADC form [61], let us start with its matrix in the basis of one-particle states $|\phi_q\rangle$

$$G_{pq}(t,t') = -i\langle\Psi_0|\hat{T}[c_p(t)c_q^\dagger(t')]|\Psi_0\rangle \tag{2.1.18}$$

Here, $|\Psi_0\rangle$ is the exact ground state of the considered N-particle system; $c_q^\dagger(t) = e^{i\hat{H}t}c_q^\dagger e^{-i\hat{H}t}$ ($c_q(t) = e^{i\hat{H}t}c_q e^{-i\hat{H}t}$) denote creation (annihilation) operators in the Heisenberg representation associated with the one-particle states $|\phi_q\rangle$; $\hat{T}$ is a time-ordering operator. The Fourier transform of the electron propagator can be written as

$$\begin{aligned}G_{pq}(\omega) &= \langle\Psi_0|c_p(\omega - \hat{H} + E_0^N + i\eta)^{-1}c_q^\dagger|\Psi_0\rangle + \langle\Psi_0|c_q^\dagger(\omega + \hat{H} - E_0^N - i\eta)^{-1}c_p|\Psi_0\rangle \\ &= G_{pq}^+(\omega) + G_{pq}^-(\omega)\end{aligned} \tag{2.1.19}$$

Here, $i\eta$ is an imaginary infinitesimal ensuring the convergence of the Fourier transforms between time and energy representations. By inserting the complete sets of $(N \pm 1)$-particle states on both sides of the two terms in Eq. (2.1.19) one obtains the spectral representation of the electron propagator

$$G_{pq}(\omega) = \sum_n \frac{\langle\Psi_0|c_p|\Psi_n^{N+1}\rangle\langle\Psi_n^{N+1}|c_q^\dagger|\Psi_0\rangle}{\omega - E_n^{N+1} + E_0^N + i\eta} + \sum_m \frac{\langle\Psi_0|c_q^\dagger|\Psi_m^{N-1}\rangle\langle\Psi_m^{N-1}|c_p|\Psi_0\rangle}{\omega + E_m^{N-1} - E_0^N - i\eta} \tag{2.1.20}$$

Here, $E_n^{N\pm1}$ and $|\Psi_n^{N\pm1}\rangle$ denote the energies and the states of the $(N\pm1)$-particle systems, E_0^N is the ground-state energy. The electron propagator is a sum of two contributions $\mathbf{G}^-(\omega)$ and $\mathbf{G}^+(\omega)$ which contain information about the processes of electron ionisation and electron attachment. The poles of $\mathbf{G}(\omega)$ give the exact ionisation energies and electron affinities

$$\begin{aligned}\mathrm{IP}_n &= E_n^{N-1} - E_0^N \\ \mathrm{EA}_n &= E_0^N - E_n^{N+1}\end{aligned} \tag{2.1.21}$$

The transition amplitudes can be obtained from the residues of $\mathbf{G}(\omega)$

$$\begin{aligned}x_p^n &= \langle\Psi_n^{N-1}|c_p|\Psi_0\rangle \\ y_p^n &= \langle\Psi_n^{N+1}|c_p^\dagger|\Psi_0\rangle\end{aligned} \tag{2.1.22}$$

There is a well-defined perturbation expansion for the electron propagator in terms of Feynman diagrams [59]. It utilises the partitioning of the Hamiltonian

$$\begin{aligned}\hat{H} &= \hat{H}_0 + \hat{H}_I \\ \hat{H}_0 &= \sum_p \epsilon_p c_p^\dagger c_p \\ \hat{H}_I &= \hat{W} + \hat{V} = \sum_{pq} w_{pq} c_p^\dagger c_q + \frac{1}{2}\sum_{pqrs} V_{pqrs} c_p^\dagger c_q^\dagger c_s c_r\end{aligned} \tag{2.1.23}$$

into a diagonal one-particle part $\hat{H}_0$ and an interaction part $\hat{H}_I$ consisting of the non-diagonal one-particle part $\hat{W}$ and the electron-electron interaction $\hat{V}$. Normally, it is assumed that $\hat{H}_0$ is the Hartree-Fock Hamiltonian.

In the following, only the $(N-1)$-particle part of the electron propagator $\mathbf{G}^-(\omega)$ will be considered. The treatment of the $(N+1)$-particle part $\mathbf{G}^+(\omega)$ is completely analogous. As discussed earlier, starting from the Fourier transform of the electron propagator and inserting the complete set of the exact $(N-1)$-particle states $\{|\Psi_m^{N-1}\rangle\}$, one obtains the spectral representation (Eq. (2.1.20)), which in matrix form reads

$$\mathbf{G}^-(\omega) = \mathbf{X}^\dagger(\omega\mathbf{1} - \mathbf{\Omega})^{-1}\mathbf{X} \tag{2.1.24}$$

Here, $\mathbf{\Omega}$ is the diagonal matrix of the exact ionisation potentials, and $\mathbf{X}$ is the matrix of transition amplitudes

$$X_{m,p} = x_p^{(m)} \tag{2.1.25}$$

The central point of the ADC approximation is the observation that the exact $(N-1)$-particle part $\mathbf{G}^{-}(\omega)$ can be written as the general non-diagonal algebraic form

$$\mathbf{G}^{-}(\omega) = \mathbf{f}^{\dagger}(\omega\mathbf{1} - \mathbf{M})^{-1}\mathbf{f} \tag{2.1.26}$$

where $\mathbf{M}$ is a hermitian secular matrix. The configuration space of $\mathbf{M}$ is the space of all $(N-1)$-particle configurations, which may be classified as 1h, 2h-1p, 3h-2p, etc. The matrix $\mathbf{f}$ is the matrix of modified (effective) transition amplitudes $f_{J,p}$. The matrix inversion in Eq. (2.1.26) can be performed after solving the hermitian eigenvalue problem

$$\mathbf{MY} = \mathbf{Y\Omega}, \mathbf{Y}^{\dagger}\mathbf{Y} = \mathbf{1} \tag{2.1.27}$$

where $\mathbf{Y}$ is the eigenvector matrix and $\mathbf{\Omega}$ is the diagonal matrix of eigenvalues Ω_m. Solving the eigenvalue problem, one can obtain the diagonal form Eq. (2.1.24), where the matrix of transition amplitudes $\mathbf{X}$ is calculated as

$$\mathbf{X} = \mathbf{Y}^{\dagger}\mathbf{f} \tag{2.1.28}$$

In order to solve the eigenvalue problem Eq. (2.1.27), first one needs to construct the effective quantities $\mathbf{f}$ and $\mathbf{M}$. In the ADC approximation this is accomplished by using their perturbation expansions

$$\mathbf{M} = \mathbf{M}^{(0)} + \mathbf{M}^{(1)} + \mathbf{M}^{(2)} + \ldots \tag{2.1.29}$$

$$\mathbf{f} = \mathbf{f}^{(0)} + \mathbf{f}^{(1)} + \mathbf{f}^{(2)} + \ldots \tag{2.1.30}$$

to generate a perturbation expansion for the one-particle Green's function

$$\begin{aligned}\mathbf{G}^{-}(\omega) &= \mathbf{f}^{(0)\dagger}(\omega\mathbf{1} - \mathbf{M}^{(0)})^{-1}\mathbf{f}^{(0)} \\ &+ \mathbf{f}^{(0)\dagger}(\omega\mathbf{1} - \mathbf{M}^{(0)})^{-1}\mathbf{M}^{(1)}(\omega\mathbf{1} - \mathbf{M}^{(0)})^{-1}\mathbf{f}^{(0)} \\ &+ \mathbf{f}^{(1)\dagger}(\omega\mathbf{1} - \mathbf{M}^{(0)})^{-1}\mathbf{f}^{(0)} + \mathbf{f}^{(0)\dagger}(\omega\mathbf{1} - \mathbf{M}^{(0)})^{-1}\mathbf{f}^{(1)} + \ldots\end{aligned} \tag{2.1.31}$$

This expansion is then compared with the diagrammatic perturbation series for $\mathbf{G}^{-}(\omega)$ through a given order of perturbation theory and the terms in the perturbation expansions of $\mathbf{f}$ and $\mathbf{M}$ are successively determined. Thus, a set of systematic approximations for $\mathbf{G}^{-}(\omega)$ referred to as ADC(n) schemes is obtained. These approximations represent infinite partial summations for the perturbation series of $\mathbf{G}(\omega)$ and are complete through order n. Analogous ADC approximations have been derived for the polarisation propagator [62] and for the two-particle propagator [63].

An alternative pathway to the ADC secular matrix is provided by the intermediate state representations (ISR) [64, 65]. Here the ADC form of the electron propagator can be rationalised as deriving from a representation in terms of a basis set of "intermediate states" $|\tilde{\Psi}_J^{N-1}\rangle$ [64]

$$G_{pq}^{-}(\omega) = \mathbf{f}_q^{\dagger}(\omega\mathbf{1} - \mathbf{M})^{-1}\mathbf{f}_p \tag{2.1.32}$$

In this basis set, the secular matrix $\mathbf{M}$ and the transition amplitudes are

$$\begin{aligned}(\mathbf{M})_{IJ} &= -\langle\tilde{\Psi}_I^{N-1}|\hat{H} - E_0^N|\tilde{\Psi}_J^{N-1}\rangle \\ f_{J,p} &= \langle\tilde{\Psi}_J^{N-1}|c_p|\Psi_0\rangle\end{aligned}$$

where $\mathbf{M}$ can be viewed as a representation of the "shifted" Hamiltonian $\hat{H} - E_0^N$. The excitation spectrum is obtained from the solution of the eigenvalue problem Eq. (2.1.27). In this case, the matrix $\mathbf{Y}$ denotes the matrix of eigenvectors and it can be considered as the representation of the exact states in the basis of intermediate states

$$Y_{Jn} = \langle\tilde{\Psi}_J^{N-1}|\Psi_n^{N-1}\rangle \tag{2.1.33}$$

From it one can obtain the spectroscopic amplitudes

$$x_p^{(m)} = \sum_I Y_{Im}^{*} f_{I,p} \tag{2.1.34}$$

and also the wave functions of the ionised states

$$|\Psi_n^{N-1}\rangle = \sum Y_{Jn}|\tilde{\Psi}_J^{N-1}\rangle \tag{2.1.35}$$

The intermediate states $|\tilde{\Psi}_J^{N-1}\rangle$ derive from the so-called correlated excited (CE) states, which are obtained by applying the "physical" excitation operators ($\hat{C}_J$) to the exact ground state $|\Psi_0\rangle$

$$|\Psi_J^0\rangle = \hat{C}_J|\Psi_0\rangle \tag{2.1.36}$$

In the case of the electron propagator, the manifold of excitation operators comprises the "classes" of 1h, 2h-1p, 3h-2p, etc. excitations

$$\{\hat{C}_J\} = \{c_i;\ c_a^{\dagger}c_ic_j, i<j;\ c_a^{\dagger}c_b^{\dagger}c_ic_jc_k, a<b, i<j<k;\ \dots\} \tag{2.1.37}$$

Provided that the basis set of one-particle states used in the construction of the excitation operators $\hat{C}_J$ is complete, the CE states are also complete, however, not orthonormal. In order to orthonormalise them, a Gram-Schmidt orthogonalisation procedure of the successive classes of CE states, (μ+1)h-μp, $\mu = 1, 2, \ldots$ is applied. The first step of this procedure is orthogonalisation with respect to the already constructed lower intermediate-state classes, which results in a set of "precursor" states $\{|\Psi_K^\#\rangle\}$

$$|\Psi_K^\#\rangle = |\Psi_K^0\rangle - \sum_{[J]<\mu} \langle\tilde{\Psi}_J|\Psi_K^0\rangle|\tilde{\Psi}_J\rangle \tag{2.1.38}$$

Here, the subscript K refers to the states of the μ-th excitation class, and $[J]$ denotes the class of excitation labelled by J. Note that in the case of the first excitation class, the "precursor" states coincide with the CE states

$$|\Psi_i^\#\rangle = c_i|\Psi_0\rangle \equiv |\Psi_i^0\rangle \tag{2.1.39}$$

The second step of the Gram-Schmidt procedure is a symmetric orthonormalisation of the precursor states within a given excitation class, as a result of which the intermediate states $\{|\tilde{\Psi}_I\rangle\}$ are obtained

$$|\tilde{\Psi}_I\rangle = \sum_{[J]=\mu} |\Psi_J^\#\rangle(\mathbf{S}^{-1/2})_{JI} \tag{2.1.40}$$

Here, $\mathbf{S}$ stands for the overlap matrix of the precursor states

$$(\mathbf{S})_{IJ} = \langle\Psi_I^\#|\Psi_J^\#\rangle \tag{2.1.41}$$

which in the case of the first excitation class has the following form

$$S_{ij} = \langle\Psi_0|c_i^\dagger c_j|\Psi_0\rangle \tag{2.1.42}$$

An important feature of the Gram-Schmidt orthogonalisation procedure is that it preserves the properties of the ADC matrix, namely compactness and separability [65]. The ISR approach to electronic excitation, single and double ionisation is presented in Refs. [66–68].

Using the intermediate states constructed as explained above, one can recover the perturbation expansions for $\mathbf{M}$ and $\mathbf{f}$ by assuming the usual partitioning of the Hamiltonian Eq. (2.1.23) and by applying Rayleigh-Schrödinger perturbation theory to the ground state $|\Psi_0\rangle$ and to the ground-state energy E_0^N. However, this procedure is quite cumbersome for the ADC schemes beyond second order. Therefore, so far it has been used only up to second order [64, 66–68].

The ISR approach overcomes some limitations of the propagator methods. On the one hand, it contains the physical information on the ionisation and attachment (or excitation) energies and transition moments. On the other hand, it has the flexibility of a wave function method and allows one to determine various properties of the final states (excited or ionised-excited states), such as transition dipole moments, for example [66–68]. Let $\hat{D}$ denote the dipole operator. Then, the corresponding ionic-state expectation value can be obtained according to

$$\begin{aligned} D_m &= \langle \Psi_m^{N-1} | \hat{D} | \Psi_m^{N-1} \rangle \\ &= \boldsymbol{Y}_m^{\dagger} \tilde{\boldsymbol{D}} \boldsymbol{Y}_m \end{aligned} \tag{2.1.43}$$

where $\boldsymbol{Y}_m$ denotes the m-th ADC eigenvector (m-th column of $\boldsymbol{Y}$), and $\tilde{\boldsymbol{D}}$ is the ISR of the operator $\hat{D}$,

$$\tilde{D}_{IJ} = \langle \tilde{\Psi}_I^{N-1} | \hat{D} | \tilde{\Psi}_J^{N-1} \rangle \tag{2.1.44}$$

In a similar way, transition moments involving two distinct final $(N-1)$-electron states,

$$\begin{aligned} D_{mn} &= \langle \Psi_m^{N-1} | \hat{D} | \Psi_n^{N-1} \rangle \\ &= \boldsymbol{Y}_m^{\dagger} \tilde{\boldsymbol{D}} \boldsymbol{Y}_n \end{aligned} \tag{2.1.45}$$

can be obtained [67]. A detailed explanation of the derivation of the ISR(2) of a general one-particle operator describing properties of singly-ionised states is presented in Ref. [67]. The respective derivation for doubly-ionised states can be found in Appendix B and Ref. [68].

Another option offered by the ADC/ISR method is to augment the ADC secular matrix by an arbitrary one-particle operator, say $\hat{U}$, and thus treat the problem of the extended Hamiltonian $\hat{H}+\hat{U}$. In this simple way, the ADC method can be extended to the computation of lifetimes of electronic states using the complex absorbing potential (CAP) method which will be discussed in the next section (Sec. 2.2).

Finally, after introducing the concept of intermediate states, the usefulness of the ADC approach can be outlined. It stems from its properties: compactness and separability (or size-consistency). Compactness means that a consistent treatment of the primary states through order $2m$ and $2m+1$ only requires one to take the configuration classes $\mu = 1, 2, ...m + 1$ into account [65]. In other words, the configuration space increases by one class with every even order n of perturbation theory. In contrast, a comparable CI expansion comprises the first $2m+1$ excitation classes. The separability of the secular matrix lies in the decoupling of local (on the separate fragments) and non-local (mixed) excitations. This means that if one considers local excitations on a separate fragment, the results for the excitation of interest obtained from the treatment of the fragment alone, and of the entire system are identical. The same refers to excited-state properties. This ensures that the ADC approach is size-consistent [65, 69].

The ADC method for the polarisation propagator can be specialised to the computation of core-excitation spectra by means of an additional core-valence separation (CVS) approximation [70]. This approximation is based on the observations that the core holes are strongly localised on the corresponding atomic sites and that there is a large difference in both energy and localisation in space between core and valence orbitals. As a consequence of the localisation of the core orbitals, one can treat the spectrum of a specific core-level vacancy separately from the spectra of other core holes [71, 72]. Additionally, due to the differences in energy and localisation between core and valence orbitals, the coupling between valence- and core-excited states is small. This allows one to separate the valence and core excitations. Consequently, terms in the Hamiltonian which do not conserve the hole occupation number can be neglected, e.g. the following two-electron integrals are set to zero [70]

$$\begin{aligned}
&V_{cijk} = V_{icjk} = V_{ijck} = V_{ijkc} = 0\\
&V_{cc'c''j} = V_{cc'jc''} = V_{cjc'c''} = V_{jcc'c''} = 0\\
&V_{ijcc'} = V_{cc'ij} = 0
\end{aligned}$$

Here, the indices i, j, k (c, c', c'') denote valence (core) one-electron orbitals. The indices c, c' in the last set of two-electron integrals may also refer to core-level vacancies of the same electronic shell, but located on different atoms (e.g. K-shell of C-atoms in benzene). As a result of this approximation, the configuration space is split into valence excitations, single-core excitations and double-core excitations, etc. Hence, the configuration space in the CVS-ADC(2) approximation reduces to

$$\text{p-h: } (j, c)$$

$$\text{2p-2h: } (i, j, c, k)$$

The ADC matrix is constructed in this reduced space, which leads to significant computational savings.

So far only the strict version of the ADC(2) method, ADC(2)-s, was discussed. Within the ADC(2)-s scheme for the polarisation propagator, the 2h-2p block of the ADC matrix is constructed only up to zeroth-order of perturbation theory. However, in order to provide a better description of double excitations, the 2h-2p block can be augmented by adding the first-order terms [73]. Raising the accuracy of the double-excitation calculation does not formally change the accuracy of a single-excitation description, but it provides a better description of excited states which are characterised by mixing of singly- and doubly-excited configurations [74]. The extended ADC(2) method, ADC(2)-x, has been shown to yield excellent results for core-excited states [74–76].

The CVS-ADC(2) method neglects the relativistic corrections [70]. Consequently, in order to obtain experimentally comparable excitation energies, one needs to account for the relativistic shifts, by adding a correction to the energies.

An alternative method for the computation of potential energy curves of Rydberg states is presented in Appendix A [77]. It makes use of the characteristic properties of these states, namely, that they can be considered as an electron interacting with a positively-charged ion. The wave functions of such states can be approximated as a product of the wave function of the electron and a state, representing the ionic “core”. The latter wave function can be constructed from correlated ionised states, obtained for example in an ADC calculation.

2.2 *Ab initio* computation of electronic decay widths

Resonances are metastable states with a finite lifetime and sufficient energy to break up into subsystems. These states possess a discrete energy, which in contrast to the energies of bound states, is a complex quantity [78]

$$E_{res} = E_R - i\frac{\Gamma}{2} \tag{2.2.1}$$

The real part of the resonance energy, E_R, is called the resonance position. The imaginary part of E_{res}, $\Gamma/2$ is the decay width associated with the lifetime of the resonance by $\tau = \hbar/\Gamma$. Most generally, resonances can be classified according to their origin as shape resonances and Feshbach resonances (also denoted as Fano resonances) [79, 80]. The former result from the shape of the potential which leads to the "particle" being temporarily trapped inside a potential well. This quantum phenomenon is known as tunnelling [81]. The temporary trapping of the particle inside the potential well can also occur when the energy of the particle is larger than the height of the potential barrier [82]. Feshbach resonances, on their turn, are formed whenever a bound state is coupled to one or more continua of states. The resonance state decays into the continuum of the open channel. Unlike shape resonances, the decay channels in this case belong to states of the reference Hamiltonian, which are different from the state supporting the bound state. The initial ICD states, considered in this work, fall into the group of Feshbach resonances.

The theoretical description of resonances requires the computation of the resonance position E_R and the decay width Γ. This is a difficult task due to the intrinsic properties of these states. For example, their wave functions are divergent at asymptotic distances [78, 79, 82], i.e. they behave as

$$\phi^{res}(r \to \infty) \propto e^{k_I r} \tag{2.2.2}$$

Therefore, the states are not square-integrable and cannot be treated using standard $\mathcal{L}^2$-methods in quantum mechanics [79]. Alternative methods designed specifically for resonance states are based on the analytic continuation of the Hamiltonian into the complex energy plane. In the complex scaling method [82, 83] this is carried out by replacing the electron coordinates $\mathbf{x}$ by $\mathbf{x}e^{i\theta}$. This enables one to associate the resonance phenomenon with a single square-integrable eigenfunction of the scaled Hamiltonian, rather than a multitude of continuum eigenstates of the unscaled Hamiltonian. Upon increasing the angle θ, resonances corresponding to higher-energy eigenstates of the unscaled Hamiltonian are uncovered and the associated eigenfunctions are transformed into square-integrable wave functions [84, 85].

A similar approach, which will be discussed in detail Sec. 2.2.1, is the complex absorbing potential (CAP) method [86]. It is much easier to use in electronic resonance problems since it does not rely on the usage of complex coordinates.

A different approach applicable to Feshbach (or Fano) resonances is the Fano-

Stieltjes method. It does not rely on complex continuation of the Hamiltonian but is rather based on the observation that the wave functions of this type of resonances can be presented as a linear combination of a bound part and a continuum part [87]. This is the main method used in this work for the calculation of ICD widths. It is presented in Sec. 2.2.2

2.2.1 Complex absorbing potential (CAP) method

The idea underlying the CAP method is to use an absorbing boundary condition in the exterior region of the molecule. The absorbing condition is a complex potential added to the molecular Hamiltonian $\hat{H}$, rendering it non-hermitian

$$\hat{H}(\eta) = \hat{H} - i\eta\hat{W} \tag{2.2.3}$$

Here, η is a real, positive scalar, controlling the CAP strength, and $\hat{W}$ is a local, positive, semi-definite operator. The CAP "absorbs" the outgoing wave and thus, makes the resonance wave function square-integrable. For a relatively large range of CAPs satisfying certain requirements [86], $\hat{H}(\eta)$ defines an analytic continuation of $\hat{H}$ in the limit $\eta \to 0^+$ if the basis set is *complete*. In this case, for every resonance state there exists an eigenvalue $E(\eta)$ of $\hat{H}(\eta)$ which satisfies the condition

$$\lim_{\eta \to 0^+} E(\eta) = E_R - i\frac{\Gamma}{2}$$

The difference $E(\eta) - E_R$ is termed expansion error. It originates from the perturbation caused by the CAP and is proportional to the CAP strength η [86].

In a *finite* basis set, the limit $\eta \to 0^+$ is not meaningful since the truncation of the basis set causes an additional error, which decreases as η grows. This error results from the fact that as η decreases, the wave function becomes more delocalised, and, therefore, the resonance can no longer be represented using an $\mathcal{L}^2$-basis set [86]. Yet the identification of resonances in this case is done by minimising the total error, which is a sum of the error originating from the finite basis set, on the one hand, and that originating from the perturbation caused by the CAP, on the other hand (as mentioned above, the two errors have opposite dependence on the CAP strength η). Thus, by increasing η starting from 0, the eigenvalues of $\hat{H}(\eta)$ move to the lower complex energy plane (see e.g. Refs. [86, 88]). The resonance states exhibit a stabilisation, i.e. for some state i ($1 \leq$

$i \leq N$) the eigenvalue $E_i(\eta)$ accumulates as a function of η in a region of the complex plane. The optimal point of stabilisation is determined by minimizing the derivative $\left|\eta \frac{dE(\eta)}{d\eta}\right|$. The optimal CAP strength $\tilde{\eta}$, determines an approximation to the resonance energy

$$E_{res} \approx E(\tilde{\eta}) \tag{2.2.4}$$

$$E_R = \mathrm{Re}(E(\tilde{\eta})) \tag{2.2.5}$$

$$\Gamma = -2\,\mathrm{Im}(E(\tilde{\eta})) \tag{2.2.6}$$

By contrast to resonances, the discretised continuum states (also called pseudo-continuum states) do not show such a behaviour – their trajectories are structureless.

What makes the CAP method so attractive is that it can easily be combined with practically any electron correlation method. This has already been done for CI (CAP/CI) [89], ADC (CAP/ADC) [90, 91] and recently also in the framework of the equation-of-motion CCSD method (EOM-CCSD) [92, 93]. The basic idea behind the CAP-extended methods is the diagonalisation of the non-hermitian matrix of the CAP-modified Hamiltonian $\hat{H}(\eta)$ for different values of η. The usual choice of a way to vary η is a power relation [86, 88]

$$\eta_n = \delta \frac{\sigma^n - 1}{\sigma - 1} \tag{2.2.7}$$

(δ and σ are parameters), and not a linear one. This is justified by the fact that the absorption length of the CAP scales roughly as $1/\sqrt[4]{\eta}$. Consequently, if η is varied linearly, many CAP steps are needed until the resonance wave function is completely absorbed by the CAP [88].

In order to construct the CAP-modified Hamiltonian, the matrix representation of the CAP operator in the atomic orbital basis set has to be obtained. The elements of the CAP matrix are calculated according to the scheme presented in Ref. [88]. Afterwards, the matrix is transformed into the Hartree-Fock molecular orbital basis. A derivation of CAP matrix elements (or more generally, of a one-particle operator) in the framework of the ADC/ISR(2) method is presented in Appendix B.

A major drawback of the CAP method is its significant numerical overhead. In order to reveal the resonances, large basis sets including diffuse functions need to be used [86, 94]. This results in large complex symmetric matrices, which have to be diagonalised repeatedly for different values of the CAP strength η. This was overcome in the subspace-CAP method [95] in combination with the parallel filter diagonalisation algorithm [88, 96]. It was shown that a small number of eigenstates of the real Hamiltonian is sufficient to expand the resonance wave function. The states are selected based on two criteria – their energy and the overlap with the reference state. The part of the CAP-modified Hamiltonian $\hat{H}(\eta)$ corresponding to the selected basis set is then used to obtain the CAP trajectory. Thus, the most time-consuming step of the CAP method is restricted to a single diagonalisation of the full Hamiltonian $\hat{H}(\eta)$ and multiple diagonalisation steps of the reduced Hamiltonian [95]. Another disadvantage of the CAP method is that the obtained results are very sensitive to the basis set and the box size chosen for the calculation [86, 97].

2.2.2 Fano-ADC-Stieltjes method

An alternative *ab initio* computational technique for decay rates of metastable electronic states is the Fano-ADC-Stieltjes approach [98]. It was first tested on atomic Auger and Coster-Kronig processes, and then used for the calculation of ICD and ETMD widths [98]. The Fano-ADC-Stieltjes method is based on the approach introduced by Fano [87], and later adapted to the case of Auger decay by Howat *et al.* [99]. Within this approach the exact wave function of a continuum state $|\Psi_E\rangle$ in the vicinity of the resonance is expressed as a superposition of one discrete state and N_c continua, describing the distinct decay channels. At large internuclear distances, $|\Psi_E\rangle$ coincides with the exact scattering wave function. The interaction between the discrete and continuous parts determines the shape of the resonance [99] and is also responsible for the finite lifetime of this state. Moreover, due to the interaction with the continuum, the energy of the discrete state is shifted. An expression for the energy shift and the decay width of the continuum state in the vicinity of the resonance was derived by Fano [87] and a summary of the derivation will be given in the following. Let us consider the case of a single discrete state $|\Phi\rangle$ and one continuum of states $|\chi_{\epsilon'}\rangle$. The part of the Hamiltonian belonging to these states is

$$\langle\Phi|\hat{H}|\Phi\rangle = E_\Phi \tag{2.2.8a}$$

$$\langle\Phi|\hat{H}|\chi_{\epsilon'}\rangle = V_{\epsilon'} \tag{2.2.8b}$$

$$\langle\chi_{\epsilon'}|\hat{H}|\chi_{\epsilon''}\rangle = \epsilon'\delta(\epsilon'-\epsilon'') \tag{2.2.8c}$$

where E_Φ denotes the energy of the "unperturbed" discrete state, $V_{\epsilon'}$ is the coupling between the discrete state $|\Phi\rangle$ and the continuum. Additionally, it is assumed that the submatrix belonging to the states $|\chi_{\epsilon'}\rangle$ has been diagonalised as a first approximation.

The eigenvector corresponding to the part of the Hamiltonian Eq. (2.2.8) has the form

$$|\Psi_E\rangle = a(E)|\Phi\rangle + \int d\epsilon' b_{\epsilon'}(E)|\chi_{\epsilon'}\rangle \tag{2.2.9}$$

It represents a continuum state of energy E in the vicinity of the resonance. It is a solution to the Schrödinger equation

$$\hat{H}|\Psi_E\rangle = E|\Psi_E\rangle \tag{2.2.10}$$

Finding a solution of the above equation comes down to determining the coefficients $a(E)$ and $b_{\epsilon'}(E)$. This is done by inserting the ansatz (2.2.9) into Eq. (2.2.10) and multiplying successively by $\langle\Phi|$ and $\langle\chi_{\epsilon'}|$. As a result, the following system of equations is obtained

$$E_\Phi a(E) + \int d\epsilon' V^*_{\epsilon'} b_{\epsilon'}(E) = E_\Phi a(E) \tag{2.2.11a}$$

$$V_{\epsilon'} a(E) + \epsilon' b_{\epsilon'}(E) = E b_{\epsilon'}(E) \tag{2.2.11b}$$

from which the coefficients $a(E)$ and $b_{\epsilon'}(E)$ can be determined (see Ref. [87] for a detailed derivation of the expressions)

$$a(E) = \frac{\sin\Theta}{\pi V_E} \tag{2.2.12a}$$

$$b_{\epsilon'}(E) = \frac{V_{\epsilon'}}{\pi V_E}\frac{\sin\Theta}{E-\epsilon'} - \cos\Theta\,\delta(E-\epsilon') \tag{2.2.12b}$$

where $\Theta = -\arctan(\frac{\pi|V_E|^2}{E-E_\Phi-\Delta(E)})$ and $\Delta(E) = P\int d\epsilon' \frac{|V_{\epsilon'}|^2}{E-\epsilon'}$ represent the phase shift of the scattered electron and the energy shift of the discrete state, respectively, resulting from the interaction with the continuum of states. Due to this interaction the discrete state $|\Phi\rangle$ becomes a band of actual stationary states represented by a resonance curve of half-width $\pi|V_E|^2$, i.e. the state $|\Phi\rangle$ autoionises with the mean lifetime

$$\tau = \frac{\hbar}{2\pi|V_E|^2} \tag{2.2.13}$$

and a decay width

$$\Gamma = \frac{\hbar}{\tau} = 2\pi|V_E|^2 \tag{2.2.14}$$

In the above approach, the interaction between the continuum states is not accounted for (see Eq. (2.2.8c)). Besides, the orthogonality of $|\Phi\rangle$ and $|\chi_{\epsilon'}\rangle$ is also assumed [87]. However, as shown in Ref. [99], the same result for the partial decay width (2.2.14) can be obtained without these two assumptions.

In the case of ICD, the discrete state is usually coupled to a multitude of continua (N_c). Each of these continua is defined by the quantum numbers of the final dicationic states. Upon the assumption that the latter interact weakly, the total decay width of the resonance state can be written as [99]

$$\Gamma = \sum_{\beta=1}^{N_c} \Gamma_\beta = \sum_{\beta=1}^{N_c} |\langle \Phi | \hat{H} - E | \chi_{\beta,\epsilon_\beta} \rangle|^2 \tag{2.2.15}$$

For the calculation of ICD widths, one needs to provide sensible approximations for the multielectron bound $|\Phi\rangle$ and continuum $|\chi_{\beta,\epsilon_\beta}\rangle$ wave functions. In the Fano-ADC-Stieltjes method the latter are constructed as an expansion in the basis of intermediate states generated in an ADC calculation (the ADC method is outlined in Sec. 2.1). This is accomplished by applying a suitable selection of the states entering the expansion of $|\Phi\rangle$ and $|\chi_{\beta,\epsilon_\beta}\rangle$. In the case considered in Ref. [98], the initial ICD state is singly-ionised. It is designed such that it does not include any component corresponding to the possible final states of the decay. This imposes a restriction on the physical excitation operators used in the construction of the CE states. The “allowed” operators are those which satisfy the condition

$$\begin{aligned} |\Psi_J^0\rangle =& \hat{C}_J |\Psi_0\rangle \qquad (2.2.16) \\ \{\hat{C}_J\} =& \{c_i; c_a^\dagger c_i c_j, i<j, E_{ij}^{(N-2)} > E_\Phi; \\ & c_a^\dagger c_b^\dagger c_i c_j c_k, i<j<k, a<b, E_{ijk}^{(N-3)} > E_\Phi, E_{aijk}^{(N-2)} > E_\Phi, E_{bijk}^{(N-2)} > E_\Phi, \dots\} \end{aligned}$$

An alternative way of constructing the bound part $|\Phi\rangle$, which is not exactly equivalent to Eq. (2.2.16), is to use a spatial criterion for selecting the configurations. Thus, $|\Phi\rangle$ will be constructed only out of the configurations residing on one of the subunits, e.g. A (which is initially ionised)

$$\begin{aligned} \{\hat{C}_J\} =& \{c_i; c_a^\dagger c_i c_j, i<j, |\phi_{i,j}\rangle \in A; \\ & c_a^\dagger c_b^\dagger c_i c_j c_k, i<j<k, a<b, |\phi_{i,j,k}\rangle \in A; \dots\} \end{aligned} \tag{2.2.17}$$

This procedure is expected to work very well in case of small overlap between the orbitals belonging to the different cluster subunits. Under this condition, the two schemes (2.2.17) and (2.2.16) are expected to give almost identical results. If the investigated system has inversion symmetry (e.g. homogeneous rare gas clusters), Eq. (2.2.17) is no longer applicable. Then $|\Phi\rangle$ can be identified as the state possessing the largest overlap with the cluster orbital representing the initial vacancy. Usually the bound states are constructed by performing a Hartree-Fock calculation and then selecting the physical operators according to one of the two schemes. Then using the restricted physical space, an ADC(n) calculation is performed to determine E_Φ. The final ICD states are constructed from the ADC 2h-1p states

$$|\chi_{\beta,\epsilon_\beta}\rangle \sim |\Psi_q^{2h1p}\rangle = \sum_i \sum_{[J]=i} Y_{q,J}|\tilde{\Psi}_J\rangle \qquad 1 - \sum_{[J]=i} |Y_{q,J}|^2 \ll 1 \tag{2.2.18}$$

This is done by performing an additional ADC calculation without any restriction on the physical operators and subsequently choosing all states $|\Psi_q^{2h1p}\rangle$ in an interval of energies around E_Φ.

After constructing the bound $|\Phi\rangle$ and the continuum $|\Psi_q^{2h1p}\rangle$ parts of the wave function, one can compute the couplings

$$\gamma_q = 2\pi|\langle\Phi|\hat{H} - E_\Phi|\Psi_q^{2h1p}\rangle|^2 \tag{2.2.19}$$

These couplings mimic the actual partial decay rates. The justification for using these couplings is not straightforward and will be discussed in detail below.

First of all, the true continuum wave functions $|\chi_{\beta,\epsilon_\beta}\rangle$ are energy normalised, unlike the states $|\Psi_q^{2h1p}\rangle$. Besides, they do not vanish outside the interaction region since they satisfy the scattering boundary conditions (at a large distance from the interaction region they represent a free particle). However, the coupling between the bound and the continuum components of the wave function is non-zero only in the interaction region, which is determined by the bound component $|\Phi\rangle$. Thus, the states $|\Psi_q^{2h1p}\rangle$ can be used to approximate the true continuum states in the interaction region provided they are

(1) renormalised to equal the true continuum wave functions in the interaction region

(2) interpolated in energy such that $E_q^{2h1p} = E_\Phi$

This can be achieved using the Stieltjes imaging technique [100, 101] which relies on the fact that the spectral moments of the quantities Γ_β obtained using the pseudospectrum are a good approximation to the true spectral moments. In this method the conditions (1) and (2) are accounted for, by computing the spectral moments of the quantities (2.2.15) using the pseudospectrum $|\Psi_q^{2h1p}\rangle$

$$\sum_\beta \int dE\, E^k |\langle\Phi|\hat{H} - E|\chi_{\beta,\epsilon_\beta}\rangle|^2 \approx \sum_q (E_q^{2h1p})^k |\langle\Phi|\hat{H} - E|\Psi_q^{2h1p}\rangle|^2 \qquad (2.2.20)$$

The true decay width can then be recovered by increasing the order k of the spectral moments until a stationary behaviour of Γ is reached. In order to obtain a reliable result, a high density of the pseudospectrum around the resonance energy is required. This is attained by employing large Gaussian basis sets with distributed Gaussians [98, 102].

The Fano-ADC-Stieltjes approach has already been successfully applied to the study of interatomic decay processes in ionised and excited clusters (see e.g. [98, 102–106]). In the current work it is used to calculate the ICD widths of various ionised-excited states of rare-gas dimers (for the computational details see Chapter 4).

2.3 Time-dependent theory of wave packet propagation

The ICD-electron and KER spectra measured in the experiment can be theoretically computed from the wave packets of all final states $|\Psi_{f_k}(E_e, t)\rangle$ propagated for a sufficiently long time [107]. The time evolution of these wave packets can be obtained by solving the time-dependent Schrödinger equation for the total wave function. To this end, the potential energy curves of all electronic states populated in the cascade, as well as the lifetimes of the decaying states have to be computed. In the previous subsections, the methods for the calculation of these quantities were presented. The current subsection focuses on the time-dependent theory of wave packet propagation, and more precisely, on its extension to the case of decay cascades [107–112]. A meticulous description of the theory can be found in Refs. [113, 114].

Let us consider a general decay cascade consisting of two stages and initiated by a resonant excitation. The system is in the initial state $|i\rangle$ (see Fig. 2.2). Upon resonant excitation, the intermediate state $|d_1\rangle$ is populated. This state decays to the intermediate states $|d_2\rangle$, which subsequently decay to the manifold of final states $|f\rangle$. The process can therefore be described with the following equation

$$|i\rangle + h\nu \rightarrow |d_1\rangle \rightarrow |d_2\rangle + e_1^- \rightarrow |f\rangle + e_1^- + e_2^- \tag{2.3.1}$$

The decay cascade considered in this work is initiated by a resonant core excitation. The first stage is the resonant Auger process, followed by ICD as the second stage.

The ansatz for the total wave function of the system in the Born-Oppenheimer approximation reads [113]

$$\begin{aligned}|\psi(t)\rangle = |\Psi_i(t)\rangle|\Phi_i\rangle + |\Psi_{d_1}(t)\rangle|\Phi_{d_1}\rangle + \sum_m \int dE_{e_1}|\Psi_{d_{2,m}}(E_{e_1},t)\rangle|\Phi_{d_{2,m}},E_{e_1}\rangle \\ + \sum_k \iint dE_{e_1}\,dE_{e_2}|\Psi^m_{f_k}(E_{e_1},E_{e_2},t)\rangle|\Phi_{f_k},E_{e_1},E_{e_2}\rangle\end{aligned} \tag{2.3.2}$$

Here, $|\Phi_i\rangle$, $|\Phi_{d_1}\rangle$, $|\Phi_{d_{2,m}},E_{e_1}\rangle$, and $|\Phi_{f_k},E_{e_1},E_{e_2}\rangle$ denote the electronic wave functions of the electronic states involved in the process. The intermediate and final electronic states are constituted of the ionised system and the emitted electrons e_1^-, and e_1^- and e_2^-, respectively. Since these states depend on the kinetic energies of the emitted electrons E_{e_1} and E_{e_2}, they can be parameterised with these energies. The associated wave functions represent an antisymmetrised product of the electronic states $|\Phi_{d_{2,m}}\rangle$ and $|\Phi_{f_k}\rangle$ of the singly- and doubly-ionised systems, and the continuum free electrons, respectively. Furthermore, as is evident from Fig. 2.2, the energies of the emitted primary and secondary electrons depend on the particular decaying state $d_{2,m}$, populated in the first step of the cascade. Therefore, the final state wave functions will also depend on the decaying state $d_{2,m}$ through the energies of the emitted secondary electrons, E_{e_2}. In Eq. (2.3.2) $|\Psi_i(t)\rangle$, $|\Psi_{d_1}(t)\rangle$, $|\Psi_{d_{2,m}}(E_{e_1},t)\rangle$, and $|\Psi^m_{f_k}(E_{e_1},E_{e_2},t)\rangle$ denote the nuclear wave functions, which describe the nuclear dynamics in the initial, decaying (d_1 and d_2) and final electronic states and are therefore time-dependent. All of the nuclear wave functions are also functions of the nuclear coordinates. Additionally, $|\Psi_{d_{2,m}}(E_{e_1},t)\rangle$ and $|\Psi^m_{f_k}(E_{e_1},E_{e_2},t)\rangle$ are parameterised with the energies of the emitted electrons. This accounts for the fact that depending on the kinetic energies of the emitted electron, the ionised molecule reaches the respective final state

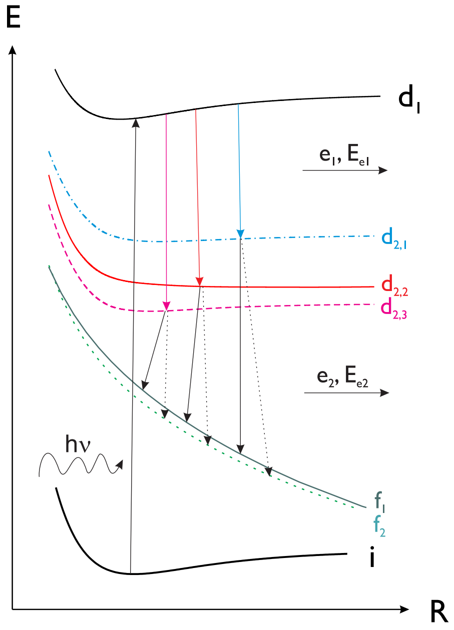

Figure 2.2: A two-step decay cascade initiated by a resonant excitation. Before the excitation the system is in the initial state i. Upon excitation the decaying state d_1 is populated. Subsequently the system decays to the intermediate states $d_{2,m}, m = 1, 2, 3$ (only three states are considered for simplicity) and emits an electron e_1^- of energy E_{e_1}, which depends on the partial decay channel. Then, each of the states $d_{2,m}$ decays to each of the final states $f_k, k = 1, 2$ by emitting an electron e_2^-. The energy of the secondary electron, E_{e_2}, depends both on the decaying and on the final state.

($|d_{2,m}\rangle$ or $|f_k\rangle$) with a different energy and therefore, different nuclear dynamics take place.

The total wave function $|\psi(t)\rangle$ (Eq. (2.3.2)) obeys the time-dependent Schrödinger equation with the Hamiltonian

$$\hat{H}(t) = \hat{T}_{\text{nuc}} + \hat{H}_{el} + \hat{\mathbf{D}} \cdot \mathbf{E}(t) \tag{2.3.3}$$

where $\hat{H}_{el}$ is the electronic Hamiltonian, $\hat{T}_{\text{nuc}}$ is the nuclear kinetic energy operator and $\hat{\mathbf{D}}$ is the dipole operator; the term $\hat{\mathbf{D}} \cdot \mathbf{E}(t)$ describes the interaction with the electromagnetic field $\mathbf{E}(t)$ [115].

The RA-ICD cascade considered here is initiated by a broad resonant excitation, which can be assumed to be instantaneous, therefore allowing one to separate the excitation from the subsequent decay. During the instantaneous excitation process the ground-state wave packet is transferred vertically to the PES of a specific core-excited state. Consequently, only the shape of the initial wave packet at time $t = 0$ is of relevance, while its time evolution is ignored. As a result, the following set of initial conditions is adopted [109, 115]

$$|\Psi_{d_1}(t=0)\rangle = \hat{W}_{i\to d_1}|\Psi_i(t=0)\rangle = \hat{W}_{i\to d_1}|\nu=0\rangle \tag{2.3.4a}$$

$$|\Psi_{d_{2,m}}(E_{e_1}, t=0)\rangle = 0 \tag{2.3.4b}$$

$$|\Psi^m_{f_k}(E_{e_1}, E_{e_2}, t=0)\rangle = 0 \tag{2.3.4c}$$

and the total Hamiltonian of the system (Eq. (2.3.3)) becomes time-independent

$$\hat{H} = \hat{T}_{\text{nuc}} + \hat{H}_{el} \tag{2.3.5}$$

The differential equations describing the motion of the nuclear wave packets on the corresponding electronic PECs can be derived from the time-dependent Schrödinger equation for the total wave function by projecting it onto the bras of the electronic states. As a result, one obtains the following system of coupled differential equations

$$i|\dot{\Psi}_{d_1}(t)\rangle = \hat{H}_{d_1}|\Psi_{d_1}(t)\rangle + \sum_m \int dE_{e_1}\hat{W}^\dagger_{d_1\to d_{2,m}}(E_{e_1})|\Psi_{d_{2,m}}(E_{e_1},t)\rangle \tag{2.3.6a}$$

$$\begin{aligned} i|\dot{\Psi}_{d_{2,m}}(E_{e_1},t)\rangle &= (\hat{H}_{d_m} + E_{e_1})|\Psi_{d_{2,m}}(E_{e_1},t)\rangle + \hat{W}_{d_1\to d_{2,m}}(E_{e_1})|\Psi_{d_1}(t)\rangle \\ &\quad + \sum_k \int dE_{e_2}\hat{W}^\dagger_{d_{2,m}\to f_k}(E_{e_2})|\Psi^m_{f_k}(E_{e_1},E_{e_2},t)\rangle \end{aligned} \tag{2.3.6b}$$

$$\begin{aligned} i|\dot{\Psi}^m_{f_k}(E_{e_1},E_{e_2},t)\rangle &= (\hat{H}_{f_k} + E_{e_1} + E_{e_2})|\Psi^m_{f_k}(E_{e_1},E_{e_2},t)\rangle \\ &\quad + \hat{W}_{d_{2,m}\to f_k}(E_{e_2})|\Psi_{d_{2,m}}(E_{e_1},t)\rangle \end{aligned} \tag{2.3.6c}$$

Here, $\hat{W}_{x\to y}$ denote the matrix elements $\langle\Phi_x|\hat{H}_{el}|\Phi_y\rangle$ responsible for the transitions between the electronic states x and y (note that they depend on the kinetic energies of the emitted electrons, see Ref. [114] for a derivation); $\hat{H}_{i/d_1/d_{2,m}/f_k}$ are the Hamiltonians for the nuclear motion on the corresponding electronic PECs and represent a sum of the nuclear kinetic energy operator $\hat{T}_{\text{nuc}}$ and the potential energy operators $\hat{V}_{i/d_1/d_{2,m}/f_k} = \langle\Phi_{i/d_1/d_{2,m}/f_k}|\hat{H}_{el}|\Phi_{i/d_1/d_{2,m}/f_k}\rangle$. In the decay cascade under consideration, the initial ICD states, i.e. the states $\{d_{2,m}\}$ are assumed to be non-interacting. Therefore, the ICD step can be considered as a separable multi-channel process [114], and Eqs. (2.3.6b) and (2.3.6c) are solved for each partial ICD channel, i.e. for each pair of decaying and final states ($d_{2,m}$, f_k).

The system (2.3.6) can be further simplified if one takes into account the time scale of the resonant Auger step following the initial excitation. It is known from the literature that the lifetime of core-excited states of different atoms and molecules is of the order of a few fs [116, 117]. Therefore, the transition between the intermediate state $|d_1\rangle$ and the manifold of intermediate states $|d_2\rangle$ is very fast so that in most cases, and in those considered in this work, the resonant Auger decay will be nearly unaffected by the nuclear dynamics on the core-excited PEC (the PEC of the intermediate state $|d_1\rangle$). Therefore, the time evolution of $|\Psi_{d_1}\rangle$ can be replaced by the following initial conditions [109, 115]

$$\begin{aligned}|\Psi_{d_{2,m}}(E_{e_1}, t=0)\rangle &= \hat{W}_{d_1\to d_{2,m}}(E_{e_1})|\Psi_{d_1}(t=0)\rangle \\ &= \hat{W}_{d_1\to d_{2,m}}(E_{e_1})\hat{W}_{i\to d_1}|\nu=0\rangle \qquad (2.3.7a)\\ |\Psi^m_{f_k}(E_{e_1}, E_{e_2}, t=0)\rangle &= 0 \qquad (2.3.7b)\end{aligned}$$

where in Eq. (2.3.7a) the initial condition for $|\Psi_{d_1}\rangle$ (Eq. (2.3.4a)) has been used. Consequently, the system (2.3.6) reduces to [115, 118]

$$\begin{aligned}i|\dot{\tilde{\Psi}}_{d_{2,m}}(t)\rangle &= (\hat{H}_{d_{2,m}} - i\frac{\hat{\Gamma}_{d_{2,m}}}{2})|\tilde{\Psi}_{d_{2,m}}(t)\rangle \qquad (2.3.8a)\\ i|\dot{\tilde{\Psi}}^m_{f_k}(E_{e_2}, t)\rangle &= (\hat{H}_{f_k} + E_{e_2})|\tilde{\Psi}^m_{f_k}(E_{e_2}, t)\rangle + \hat{W}_{d_{2,m}\to f_k}|\tilde{\Psi}_{d_{2,m}}(t)\rangle \qquad (2.3.8b)\end{aligned}$$

where the effective Hamilton operators $\hat{\mathcal{H}}_{d_{2,m}} = \hat{H}_{d_{2,m}} - i\frac{\hat{\Gamma}_{d_{2,m}}}{2}$ have been introduced allowing one to decouple the equations for the decaying wave packets (Eq. (2.3.8a)) from these of the final wave packets (Eq. (2.3.8b)) (for a derivation see Ref. [115]). Note that the introduction of the initial conditions (Eqs. (2.3.7)) allows one to use the so-called *dressed states* [114, 119], in which the energy E_{e_1} appears as a phase of the wave packets. The dressed nuclear wave functions are indicated in Eqs. (2.3.8) as $|\tilde{\Psi}_{d_{2,m}}(t)\rangle$ and $|\tilde{\Psi}^m_{f_k}(E_{e_2}, t)\rangle$. In the current work, the transition operators $\hat{W}_{i\to d_1}$ and $\hat{W}_{d_1\to d_{2,m}}$ have been assumed to be the unity operators similarly to previous nuclear dynamics calculations [111, 113, 115, 118].

The effective Hamiltonians in Eqs. (2.3.8a) contain the decay width operators $\hat{\Gamma}_{d_{2,m}}$, which are in general non-local and depend on the energies of the emitted electrons. However, in cases when the decaying and final states are energetically well separated, the so-called local approximation can be adopted [107, 115, 120–122]. Within this approximation the decay widths $\hat{\Gamma}_{d_{2,m}}$, as well as the partial decay widths $\hat{\Gamma}_{d_{2,m}\to f_k}$ and the transition elements $\hat{W}_{d_{2,m}\to f_k}$, can be considered as functions of the nuclear coordinates alone, and not of the energy of the emitted electron E_{e_2}. Consequently, the relation between the transition elements $\hat{W}_{d_{2,m}\to f_k}$

and the partial decay widths $\hat{\Gamma}_{d_{2,m}\to f_k}$ takes the following form

$$\hat{\Gamma}_{d_{2,m}\to f_k}(R) = 2\pi|\hat{W}_{d_{2,m}\to f_k}(R)|^2 \tag{2.3.9}$$

The local approximation has been used in previous calculations of ICD dynamics, which shows that the interactions between the decaying and the final states can indeed be neglected [111, 112, 118, 123].

The kinetic energy distributions of the emitted electrons following the decay in a particular channel can be obtained from the nuclear wave packets on the corresponding final state at large times, at which the decay is essentially complete [115]

$$\sigma^m_{f_k}(E_{e_2}) = \lim_{t\to\infty}\langle\Psi^m_{f_k}(E_{e_2},t)|\Psi^m_{f_k}(E_{e_2},t)\rangle \tag{2.3.10}$$

The ICD electron spectrum of a particular decaying state is then the sum of the partial intensities $\sigma^m_{f_k}(E_{e_2})$ which correspond to all possible decay channels

$$\sigma^m(E_{e_2}) = \sum_k \sigma^m_{f_k}(E_{e_2}) \tag{2.3.11}$$

As a result of energy conservation during the ICD process, the sum of the kinetic energy of the emitted particles (electrons and ions) is constant [124]

$$E_{KER} + E_{e_2} = E_m(R_e) - E_f(\infty) = \text{const} \tag{2.3.12}$$

Therefore, the KER spectra of the nuclei originating from the decay of a particular state, e.g. d_m, can be obtained from the respective ICD-electron spectra as follows

$$\sigma^m_{KER}(E_{KER}) = \sigma^m_{ICD}(E_m(R_e) - E_f(\infty) - E_{e_2}) \tag{2.3.13}$$

Here, E_{KER} is the kinetic energy of the nuclei, $E_m(R_e)$ is the electronic energy of the decaying state at R_e, and $E_f(\infty)$ is the asymptotic energy of the final states. Eq. (2.3.13) is known as the mirror image principle [124–126].

The total ICD-electron and KER spectra of a cascade initiated by a particular core excitation are calculated as weighted sums of the spectra $\sigma^m(E_{e_2})$ belonging to a particular decaying state $d_{2,m}$ populated in the RA step

$$\sigma(E_{e_2}) = \sum_m w_m \sigma^m(E_{e_2}) \tag{2.3.14}$$

In the case of the RA-ICD cascade, the respective weights w_m can be obtained from experimental branching rations of the resonant Auger process.

Chapter 3

Ionisation satellites of ArHe

To model the spectra of the ICD electrons and ions emitted in the resonant-Auger – ICD cascade, one has to compute the nuclear dynamics during the ICD step. This, in turn, requires the knowledge of the potential energy curves of the ionisation satellites populated in the resonant Auger step. An accurate *ab initio* description of ionisation satellites for heavy dimers such as Ar_2 and ArKr is extremely challenging. First, since these states have comparatively high energies and often lie in the electronic continuum their determination involves calculating many excited states (usually >100) and the use of large diffuse basis sets. This results in large Hamiltonian matrices which make the computation extremely time consuming. Second, once the excited states have been calculated, the construction of PECs is further complicated by a high density of states at the energies in question. This can even make the construction of the PEC in the case of higher-lying satellites outright impossible.

This implies that in some cases one needs an alternative way of constructing the PECs of such systems, for which one has to understand the bonding in Ar–RG satellite states. Thus, for diatomic complexes of an alkaline earth metal (M) and a rare-gas atom (RG) (M–RG) accurate *ab initio* calculations of the PECs corresponding to the lowest satellites located on the metal ion have been reported in the literature [127–129]. The results suggest that a one-electron picture for the satellites based on the parent dicationic species can qualitatively reproduce some of the PECs in these systems. The substantial difference in the electronic structure between the satellite states of RG–RG and M–RG demands, however, a closer look at the former before any development of the model potential methods is attempted. In the satellite of an alkaline earth metal atom both holes occupy a ns orbital and are coupled to form a non-degenerate term of $^1\Sigma^+$ symmetry. In this case one can straightforwardly construct a model potential in which the Rydberg electron moves. In the case of satellite states of a rare-gas atom, the holes occupy a degenerate *np* shell and are coupled to form ^3P, ^1D, and ^1S multiplets. Starting from these hole configurations one can construct several parent dicationic states of the diatomic. As a result, in a satellite state there exist two possibilities for the excited electron. It may either move in the field of a single dicationic parent state or the parent states might become mixed by configuration interaction resulting in a more complicated potential.

In order to understand the bonding in Ar–RG satellite states, we carried out *ab initio* calculations for the simplest member of the family, ArHe. To simplify the comparison between the satellite and dicationic PECs, we constructed the diabatic states from the adiabatic ones obtained in the calculation. We then analysed the PECs of the lowest members of the $\mathrm{Ar}^+(3p^{-2}ns)\mathrm{He}$ and $\mathrm{Ar}^+(3p^{-2}nd)\mathrm{He}$ Rydberg series to see the effect of configuration interaction on the parent states mixing. We further compare the PECs to those of the corresponding parent dication $\mathrm{Ar}^{2+}(3p^{-2})\mathrm{He}$ and discuss the plausibility of using a one-electron model for such systems.

The chapter is organised as follows. In the next section, we give the details of the *ab initio* computational methodology. The results of the calculations are presented and discussed in Sec. 3.2, while the conclusions follow in Sec. 3.3. The discussion of the PECs is done in terms of diabatic states unless indicated otherwise.

3.1 Computational details

The satellite states of ArHe were computed using the MRCI approach (see Sec. 2.1). Specifically, the reference space involved five one-hole (1h) electron configurations that comprised all possible (spin-free) occupations of the 5 "valence" orbitals of ArHe with 9 electrons; at the dissociation limit these orbitals correlated with the $1s$ orbital of He and $3s$ and $3p$ orbitals of Ar. The final CI expansion was constructed by allowing all single, double and triple excitations (MRCI-SDT) out of the reference configurations. In the resulting CI-matrix the maximum number of holes thus equalled 4 while the maximum number of excited electrons was 3, with respect to the neutral ground state of ArHe. The resulting 1h, 2h-1p, 3h-2p and 4h-3p CI-space is expected to provide fairly accurate description of the satellite (2h-1p) states. To find all states of interest the 45 lowest roots of the resulting CI

Table 3.1: Excitation energies (E, eV) of some $Ar^+(3p^{-2}4s)$He and $Ar^+(3p^{-2}3d)$He satellites computed using the MRCI-SDT method and their deviation ($\Delta E = E - E(\mathrm{NIST})$, eV) from the corresponding atomic values taken from the NIST database [130]. The mean absolute error (MAE, eV) and the standard deviation (SD, eV) are given for each set of states.

	$Ar^+(3p^{-2}4s)$He state			$Ar^+(3p^{-2}[^1D]3d)$He state				
	^2P	^2D	^2S	^2G	^2F	^2D	^2P	^2S
E	17.365	18.698	20.988	19.629	20.775	21.801	22.056	23.212
ΔE	0.183	0.255	0.245	0.512	0.514	0.409	0.415	0.388
MAE		0.227				0.448		
SD		0.0318				0.0541		

matrices in each irreducible representation of the C_{2v} point group were computed.

Besides the satellite states, the PECs of the parent doubly-ionised states are also considered. These were computed using MRCI-SD (i.e. all single and double excitations out of the reference) in order to be consistent with the description of the satellite states. The reference space here involved all possible configurations with two “unpaired” holes in the $3s$ and $3p$ orbitals of Ar and $1s$ of He (overall 10 configurations). Because of different spin multiplicity of the dicationic states (two singlets and one triplet) two sets of the reference space were constructed. In all CI calculations, for satellites as well as parent dications, the canonical Hartree-Fock orbitals of the neutral ArHe obtained at a corresponding interatomic distance were used in the CI expansions. The advantage of the neutral molecular orbitals (MOs) here has to do with their correct description of degeneracy of the $3p$ orbitals as well as facilitating the comparison between different states. The large number of states to be calculated and the fast growth of the CI matrix with the number of one-electron basis functions imposes severe restrictions on the size of the atomic basis sets. For the PECs of the $Ar^+(3p^{-2}4s, 3d)$He states the following Gaussian type orbitals (GTO) basis set was used. The cc-pVTZ basis set [131] augmented by two s, two p and two d diffuse GTOs, and a compact d GTO was used on Ar [132]. The compact GTO was added to improve the description of Rydberg electrons in the field of the Ar^{2+} ion. The analogous basis set [133] (without the compact GTO) was used on He. The molecular orbitals corresponding to the $1s$, $2s$, and $2p$ electrons of Ar were frozen in all CI calculations. At the asymptotic interatomic distance the excitation energies of the satellite states relative to the ground state of Ar$^+$He were compared to the corresponding atomic values for Ar listed in the NIST database [130]. The calculations reproduce the correct order of the lower excited states. The mean absolute error for the energies of the $4s$ ($3d$) satellites is 227 meV (448 meV), while the standard deviation of the error is 32 meV (54 meV) (see Table 3.1). The same basis set and number of frozen core orbitals as described above was used in the calculations of the dicationic states.

All CI calculations were performed employing the Unitary Group CI package based on the Graphical Unitary Group Approach (GUGA) as implemented in the GAMESS-US suite of programs [134]. The average size of the CI matrix in our calculations was $\sim 5 \cdot 10^6$.

For plotting the PECs of the satellite and dicationic states the plain CI energies were used. A correction for the size-consistency has not been applied because it could not be reliably computed for all the states under consideration. However, for the present results, the error related to the lack of size-consistency for a restricted CI expansion is expected to be small. This follows from the high level of excitation in the final CI matrices (up to triples) and a relatively small number of correlated electrons (9 for satellites and 8 for dications).

The PECs of the low lying Ar$^+$($3p^{-2}4s$, $3d$)He states were also computed using the computationally cheaper, though less accurate, MRCI-SD (i.e. all single and double excitations out of the reference configurations) method. The order of the states for the energy range considered is reproduced correctly at large interatomic distances. Also the PECs obtained by the MRCI-SD method do not deviate significantly from the MRCI-SDT PECs at shorter interatomic distances. This supports the estimation that the error related to the lack of size-consistency is small. It also indicates that the inclusion of the complete three-hole two-particle (3h-2p) configuration space is sufficient to obtain an adequate description of the bonding in certain ionised-excited states.

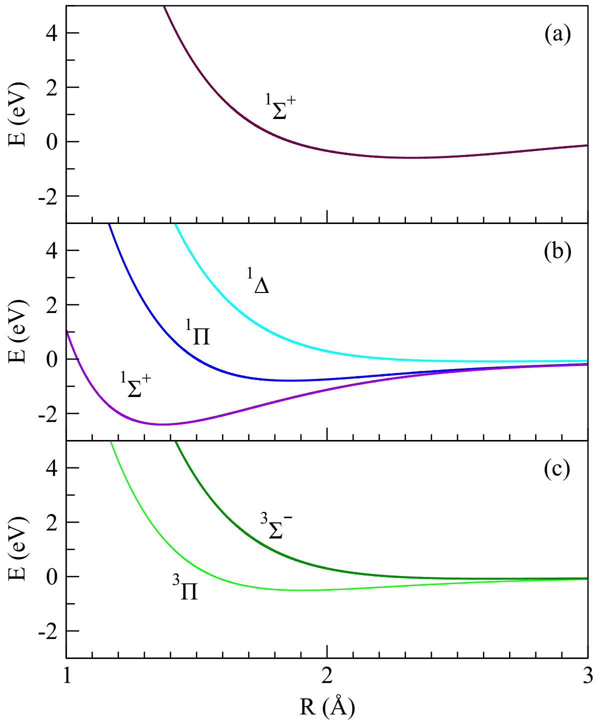

Figure 3.1: PECs of the doubly-ionised states of ArHe correlating at large interatomic distances with (a) $Ar^{2+}(3p^{-2}[^1S])$ dication and the ground state He atom; (b) $Ar^{2+}(3p^{-2}[^1D])$ dication and the ground state He atom; (c) $Ar^{2+}(3p^{-2}[^3P])$ dication and the ground state He atom.

3.2 Results and discussion

3.2.1 $Ar^{2+}(3p^{-2})$He parent dicationic states

A picture of a satellite state as a dicationic state perturbed by interaction with the Rydberg electron offers an appealing way of understanding and characterising its potential energy curve. However, whether this picture remains valid for the $Ar^+(3p^{-2}nl)$RG satellite states is by no means obvious. Since the holes occupy a degenerate $3p$ shell, several dicationic parent states correspond to the satellites in question. If the configuration interaction in the satellite state mixes these parent states, there will be no simple correspondence between the satellite and dicationic states.

To clarify the above point, the dicationic curves corresponding to the Ar^{2+}He doubly-ionised states were computed first. The three multiplets, ^3P, ^1D, ^1S, of $Ar^{2+}(3p^4)$ cation split into a number of molecular terms in Ar^{2+}He. The corresponding PECs are shown in Fig. 3.1 and exhibit markedly different bonding behaviour. Let us consider first the $^1\Sigma^+$, $^1\Pi$, and $^1\Delta$ states originating from the $Ar^{2+}(3p^{-2}[^1D])$He multiplet (Fig. 3.1(b), Table 3.2). The $^1\Sigma^+$ state is exceptionally strongly bound ($D_e = 2.4\,\mathrm{eV}$, $R_e = 1.37\,\text{Å}$) and its minimum is shifted to

Table 3.2: The equilibrium distance (R_e, Å) and the dissociation energy (D_e, meV) of the $\mathrm{Ar}^{2+}(3p^{-2})\mathrm{He}$ dicationic states.

	$^3\Sigma^-(^3P)$	$^3\Pi(^3P)$	$^1\Sigma^+(^1D)$	$^1\Pi(^1D)$	$^1\Delta(^1D)$	$^1\Sigma^+(^1S)$
R_e	2.64	1.90	1.37	1.86	2.64	2.33
D_e	80	503	2400	792	80	595

small interatomic distances. The $^1\Delta$ state is only weakly bound ($D_e = 0.08\,\mathrm{eV}$, $R_e = 2.64\,\text{Å}$), while the bonding in the $^1\Pi$ state ($D_e = 0.79\,\mathrm{eV}$, $R_e = 1.86\,\text{Å}$) lies between these two extremes.

This varying bonding strength can be understood from the following considerations. The leading electronic configuration in the $^1\Sigma^+$ is of $3p_z^{-2}$ character and both holes on Ar are localised along the interatomic axis. Since the He atom lacks a filled p-shell and the four remaining $3p$ electrons of the Ar atom are localised off the interatomic axis, their mutual repulsion is minimised. Therefore, the He atom can approach the ionised core of the neighbour more closely. Analysing this state we observed that at the equilibrium interatomic distance the $1s$ orbital of He mixes strongly with the empty $3p_z$ orbital of Ar. The resulting delocalisation of charge leads to the significant lowering of the orbital energy, and may explain the exceptionally strong bonding in this state. Similarly, the leading configuration in the $^1\Pi$ state is of the $3p_{x,y}^{-1}3p_z^{-1}$ character with only one hole localised along the interatomic axis. The repulsion between a $3p_z$ electron and He results in a PEC whose interaction energy is three times lower and whose minimum is shifted to larger distances than in the case of the $^1\Sigma^+$ state. In the $^1\Delta$ case the holes described by the $3p_x^{-1}3p_y^{-1}$ configuration are localised off the interatomic axis leading to large electron repulsion and, consequently, exceptionally weak binding in this state.

The PECs corresponding to the ^3P and ^1S multiplets can be understood analogously. In particular, the $^3\Sigma^-$ term is seen to be only slightly bound at large interatomic distances (Fig. 3.1(c)). The depth and the minimum of its PEC are very similar to those of the $^1\Delta$ state (Table 3.2). This is explained by the fact that the leading electronic configuration of the state is of $3p_x^{-1}3p_y^{-1}$ character with both holes localised off the interatomic axis. The PEC corresponding to the $^3\Pi$ term has one hole localised on the interatomic axis, the corresponding configuration is $3p_{x,y}^{-1}3p_z^{-1}$. Therefore, it is expected to be more bound than the $^3\Sigma^-$ state and resemble the $^1\Pi$ state (see Table 3.2). The $^1\Sigma^+$ molecular term stemming from the ^1S parent dicationic state differs appreciably from the $^1\Sigma^+$ state of the ^1D multiplet (Fig. 3.1(a)). Although both states are linear combinations of the $3p_x^{-2}$, $3p_y^{-2}$ and $3p_z^{-2}$ hole configurations, the $[^1D]$ $^1\Sigma^+$ state is characterised by the leading hole configuration which is $3p_z^{-2}$, whereas for the $[^1S]$ $^1\Sigma^+$ state the three hole configurations contribute equally. Therefore, the $[^1S]$ $^1\Sigma^+$ PEC has a smaller binding energy and a minimum shifted to a larger interatomic distance.

3.2.2 Ar$^+(3p^{-2}4s)$He ionisation satellites

The computed PECs of the Ar$^+(3p^{-2}[^3P,\,^1D,\,^1S]4s)$He ionisation satellites having the total spin $S = 1/2$ are presented in Fig. 3.2. Analysis of the CI vectors of these satellites shows that these states are obtained by adding a Rydberg electron to some specific dicationic state of ArHe. Since the excited electron occupies an orbital of s symmetry, the number of such satellites equals the number of the parent dicationic states, and their molecular symmetry is determined by the symmetry of the latter states. Consider for example the PEC of the Ar$^+(3p^{-2}[^1D]4s)$He $^2\Sigma^+$ state (see Fig. 3.2(b)). It has $D_e = 2.33\,\text{eV}$ and $R_e = 1.30\,\text{Å}$ which are close to the corresponding values of the Ar$^{2+}(3p^{-2}[^1D])$He $^1\Sigma^+$ dicationic state (see Table 3.2, 3.3). The shift of the satellite PEC minimum to a smaller distance compared with the doubly-ionised curve has been also observed for Mg$^+(3s^{-2}3p\pi)$He [129]. It has been ascribed to the effect of an additional dispersive attractive interaction due to the presence of a Rydberg electron in the satellite state.

The interaction of the He atom with the $4s$ Rydberg electron leads to a number of differences between the satellite and the parent dicationic PECs. First, the potential well of the satellite is narrower than the well of the dication. Second, the satellite PEC exhibits a small maximum of $52\,\text{meV}$ at $R = 2.76\,\text{Å}$ (see inset of Fig. 3.2(b)), and has a shallow minimum at $4.82\,\text{Å}$ absent in the dicationic PEC. Indeed, the natural orbital of the $4s$ electron (Fig. 3.2(b$'$)) has considerable density at distances between $1.0\,\text{Å}$ and $4.0\,\text{Å}$ from the Ar atom peaking at $1.7\,\text{Å}$. Thus, at large interatomic distances charge-induced dipole interaction results in the gentle decrease in the PEC. Approximately at $R = 5.5\,\text{Å}$ the repulsion between the electrons of He and the Rydberg electron sets in, leading to the appearance of a shallow minimum and then of a maximum in the PEC. The latter roughly coincides

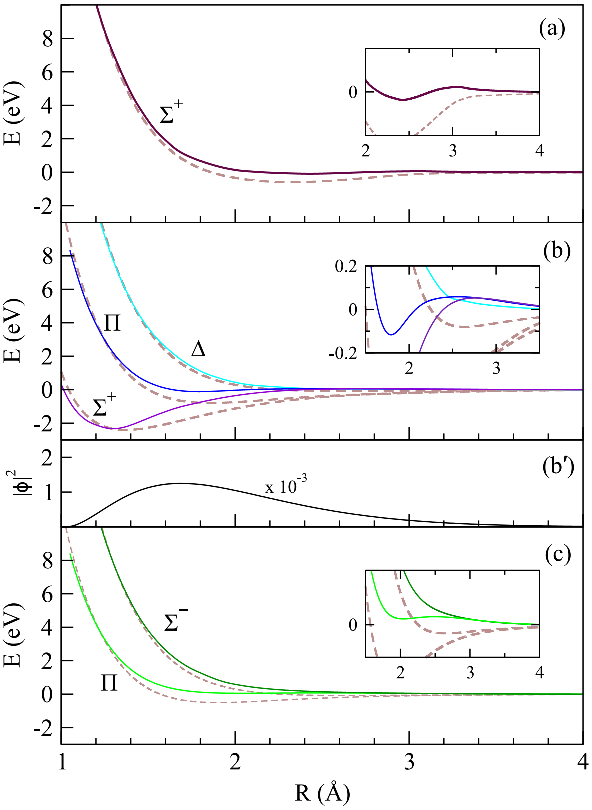

Figure 3.2: Comparison of the PECs of $\text{Ar}^+(3p^{-2}4s)$He spin doublet ionisation satellites with the PECs of the corresponding dicationic parent states (broken lines) (see Fig. 3.1). (a) satellite state correlating with $\text{Ar}^{2+}(3p^{-2}[^1S]4s)$ and the ground state He atom; (b) satellite states correlating with $\text{Ar}^{2+}(3p^{-2}[^1D]4s)$ and the ground state He atom; (b′) natural orbital density of the $4s$ electron in the $\text{Ar}^+(3p^{-2}[^1D]4s)$ atomic state; (c) satellite states correlating with $\text{Ar}^{2+}(3p^{-2}[^3P]4s)$ and the ground state He atom. The insets show the parts of satellite PECs exhibiting a maximum which appears due to the interaction between $4s$ Rydberg electron and the He atom.

with the maximum in the density of the $4s$ orbital. This repulsion continues to be effective down to 1.5 Å resulting in the narrower well of the satellite. An interesting point is that the occurrence of a maximum in the satellite PEC is not due to an avoided crossing with a higher-lying PEC, but it is the result of interaction of the $4s$ electron with the He atom. This explanation has also been offered for a similar structure observed in the case of doubly-excited states of CaAr [135]. Appearance of maxima in a PEC coinciding with the maxima in the electron density of a Rydberg electron has also been predicted in neutral Rydberg molecules such as dimers of the alkali metals. In these systems the PECs of highly-excited Rydberg states show oscillations mimicking the density variation of the corresponding Rydberg orbitals (see e.g. Ref. [136]).

The minimum of the dicationic $\text{Ar}^{2+}(3p^{-2}[^1D])\text{He}\ ^1\Sigma^+$ state lies at the interatomic distance where the density of the $4s$ electron is small. This explains the similarity between its PEC and the PEC of the $\text{Ar}^+(3p^{-2}[^1D]4s)\text{He}\ ^2\Sigma^+$ state. As is evident from Table 3.3 the minima of the other dicationic states of interest lie in the region where the $4s$ electron density is considerable. Thus, although the

Table 3.3: The minima (R_e, Å) and the corresponding depths (D_e, meV) of the $\mathrm{Ar}^+(3p^{-2}4s)\mathrm{He}$ ionisation satellite states. Note the appearance of a double well structure for the $^2\Sigma^+(^1D)$, $^2\Pi(^1D)$ and $^2\Sigma^+(^1S)$ states.

	$^2\Sigma^-(^3P)$	$^2\Pi(^3P)$	$^2\Sigma^+(^1D)$		$^2\Pi(^1D)$		$^2\Delta(^1D)$	$^2\Sigma^+(^1S)$	
R_e	4.83	4.86	1.30	4.82	1.79	4.77	4.41	2.43	4.76
D_e	2.3	2.4	2330	2.4	117	2.4	3.2	92	2.56

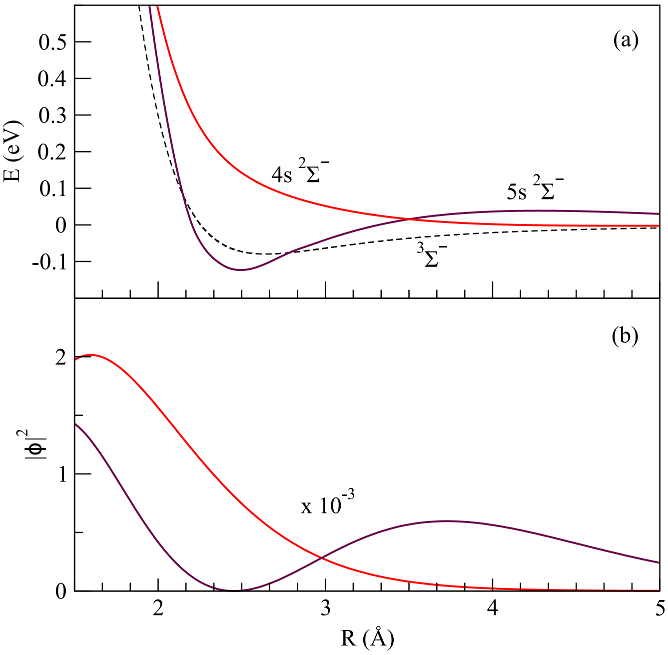

Figure 3.3: (a) Comparison of the PECs of $^2\Sigma^-$ symmetry of $\mathrm{Ar}^+(3p^{-2}[^3P]4s)\mathrm{He}$ (red) and $\mathrm{Ar}^+(3p^{-2}[^3P]5s)\mathrm{He}$ (brown) satellite states with the PEC of the parent dicationic $\mathrm{Ar}^{2+}(3p^{-2}[^3P])\mathrm{He}$ state (see Fig. 3.1(c)). (b) Natural orbital density of the Rydberg electron in the $\mathrm{Ar}^+(3p^{-2}[^3P]4s)$ (red) and $\mathrm{Ar}^+(3p^{-2}[^3P]5s)$ (brown) states.

satellite PECs bear a broad resemblance to the PECs of the parent dication, their bonding character is strongly influenced by the 4*s* Rydberg electron. The potential wells in the satellite PECs are either much shallower than in the dicationic PECs or are absent altogether. In addition, all satellite curves exhibit a shallow minimum of about 2 meV at 4.4 – 4.9 Å, whose appearance was explained above. Whenever the satellite PEC has the double-well character, the barrier separating the wells is located between 2.5 Å and 3.1 Å and has a height between 52 meV and 74 meV (see insets to Fig. 3.2). The position of the barrier again broadly corresponds to the maximum in the density of the 4*s* electron.

3.2.3 Higher lying $\mathrm{Ar}^+(3p^{-2}5s)$He and $\mathrm{Ar}^+(3p^{-2}3d)$He states

If an electron is excited to a higher Rydberg orbital, the electron density spreads towards larger distances from the Ar atom (see Fig. 3.3(b) for the difference between the $4s$ and $5s$ natural orbital densities). Therefore, the repulsion between the He atom and the Rydberg electron in the bonding region diminishes and one can expect a better correspondence between satellite and dicationic PECs in this region. We were able to identify the $^2\Sigma^-$ Ar$^+$($3p^{-2}[^3P]5s$)He state higher in the spectrum. The PECs of the Ar$^+$($3p^{-2}[^3P]4s$)He $^2\Sigma^-$, Ar$^+$($3p^{-2}[^3P]5s$)He $^2\Sigma^-$, and Ar^{2+}($3p^{-2}[^3P]$)He $^3\Sigma^-$ states are plotted in Fig. 3.3(a). The satellite PECs clearly show the variation in the bonding strength with the state of the Rydberg electron. The $5s$ satellite curve has a well at $R_e = 2.50\,\text{Å}$ of $D_e = 123\,\text{meV}$ which is almost identical to the well in the PEC of the doubly-ionised parent state. One can also see that the maximum due to the interaction of the Rydberg electron with the He atom is shifted to larger interatomic distances (4.28 Å) reflecting the larger size of the $5s$ orbital (Fig. 3.3(b)). Therefore, the PECs of satellites obtained from a single parent dication and having the electron on a higher virtual orbital have indeed similar bonding properties to the PECs of the corresponding dication.

We consider next the spin doublet satellites of Ar$^+$($3p^{-2}[^1D]3d$)He character. Fifteen molecular terms can be constructed from the $[^1D]\Sigma^+$, $[^1D]\Pi$, $[^1D]\Delta$ states of Ar^{2+}He by adding to them a $3d$ Rydberg electron. If several of these terms are of the same symmetry, they may become mixed by configuration interaction. In this case, the corresponding satellite state can no more be viewed as a Rydberg electron in the field of a single parent dication. Alternatively, terms of the same symmetry may not be coupled by the configuration interaction. It can also happen that only a single term can be found for certain molecular symmetries. In such case, the corresponding satellite state can be uniquely assigned to a parent dicationic state.

For example, there are three terms of $^2\Delta$ symmetry which can be constructed from the $[^1D]\Sigma^+$, $[^1D]\Pi$, $[^1D]\Delta$ dicationic Ar^{2+}He states by adding to them a $3d\delta$, $3d\pi$, and $3d\sigma$ Rydberg electron. Analogously to the case of the Ar$^+$($3p^{-2}[^1D]4s$)He satellites considered above one would expect a strongly bound, a moderately bound, and an unbound (or very weakly bound) PEC corresponding to these terms. However, it is evident from Fig. 3.4(a) that all three PECs are only weakly bound and their shapes bear no resemblance to the dicationic PECs. The analysis of the CI wave functions shows that configuration interaction mixes different two-hole configurations, and, therefore, the Rydberg electron moves in a potential corresponding to some weighted average of the dicationic states potentials. On the contrary, the two terms of the $^2\Sigma^-$ symmetry corresponding to the same

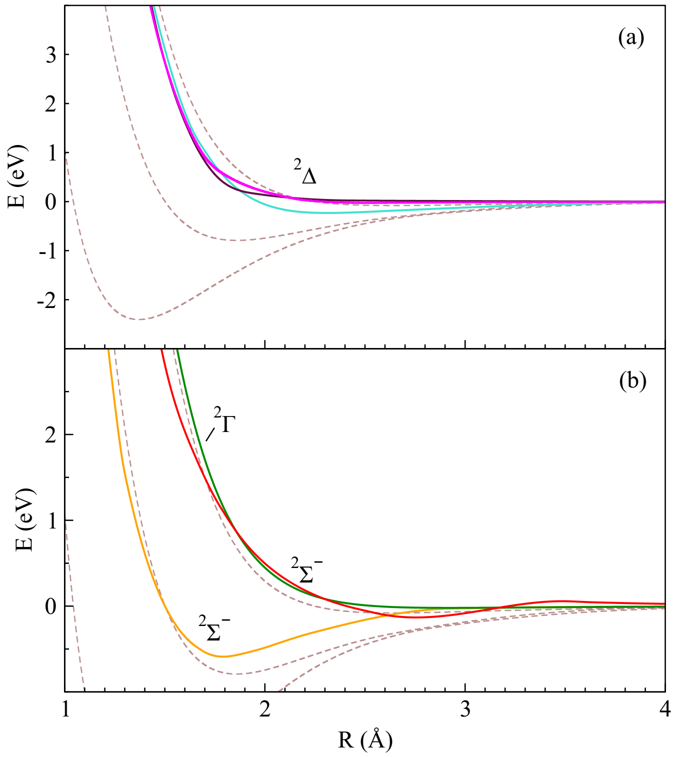

Figure 3.4: Comparison of the PECs of $\mathrm{Ar}^+(3p^{-2}[^1D])3d)\mathrm{He}$ spin doublet ionisation satellites with the PECs of the corresponding dicationic parent states (broken lines) (see Fig. 3.1(b)). (a) Satellite states of $^2\Delta$ symmetry; (b) Satellite states of $^2\Gamma$ symmetry and $^2\Sigma^-$ symmetry.

$\mathrm{Ar}^+(3p^{-2}[^1D]3d)\mathrm{He}$ electronic configuration are not mixed and their curves behave similarly to the PECs of the parent $[^1D]\Pi$ and $[^1D]\Delta$ dicationic states (Fig. 3.4 (b)). Interestingly, the presence, or absence of mixing of the two-hole configurations in these satellites is manifest already at asymptotic interatomic distances and persists for all considered distances. There is also a single term of $^2\Gamma$ symmetry obtained by adding the $3d\delta$ Rydberg electron to the $[^1D]\Delta$ dicationic state (Fig. 3.4(b)). Its diabatic PEC as expected closely resembles the PEC of the parent state.

3.3 Summary and conclusions

In this chapter, the structure of the PECs of the lower-lying ionisation satellites of ArHe was investigated with a view of modelling similar states in systems where they cannot be computed by direct application of *ab initio* methods. In contrast to previous studies of ionisation satellites in M–RG complexes, the simple model describing the Rydberg electron moving on top of the dicationic parent can break down in RG–RG systems.

When several terms of the same molecular symmetry can be formed by adding a Rydberg electron to different parent dications, they may mix by configuration interaction. This occurs, for example for the $\mathrm{Ar}^+(3p^{-2}[^1D]3d)\mathrm{He}\ ^2\Delta$ satellites. As a result, the Rydberg electron moves in a potential represented by some weighted average of the potentials of the dications, and any resemblance between the satellite and dicationic PECs is destroyed. The presence of strong configuration mixing is obvious already at the asymptotic interatomic distances.

The ionisation satellites in which the electron occupies an s-type Rydberg orbital result in unique molecular terms. This leads to the overall resemblance of the corresponding satellite and dicationic potential energy curves. However, the interaction of the Rydberg electron with the He perturber leads to the important differences between these PECs. Thus, the well depth of the most satellite curves decreases compared with the parent dicationic curves, or in the case of weaker-bound dications the well might disappear altogether. The satellite curves are moreover characterised by the appearance of a maximum at interatomic distances corresponding to the maximum of the electronic density of the Rydberg orbital, followed by a shallow minimum at larger interatomic separations. Exciting the Rydberg electron to a higher, more diffuse Rydberg orbital was shown to lead to a considerable improvement in the correspondence of the satellite and dicationic PECs.

The study of the ionisation satellites of ArHe shows that by considering the different possible satellites already for the separated atoms, one could predict for which states an electron on top of a dicationic parent type of model could be applied. This could provide a limited solution for larger systems where such high-level *ab initio* calculations and the subsequent analysis of the states are very difficult.

Chapter 4

Resonant-Auger – ICD cascade in rare-gas dimers

The structure of the ICD-electron and kinetic-energy-release (KER) spectra depends on the specific manifold of ionisation satellites, which undergo ICD, and also on the nature of the neighbouring species. This was confirmed in a series of experimental studies in ArNe, Ar_2, ArKr, and ArXe [45–47]. In these experiments the cascade was initiated by resonant photoexcitation of a $2p$ core electron of Ar to the $4s$ or the $nd, n = 3, 4, 5$, virtual orbital. The resulting ICD-electron spectra indeed show marked dependence on the parent core excitation. Additionally, it was demonstrated that the partner atom's choice can influence the ICD emission [47] and that it can even serve as a switch for particular decay channels [45].

In this chapter we investigate the ICD process in Ar_2 and ArKr following the resonant Auger decay of $2p_{3/2} \rightarrow 4s$, $2p_{1/2} \rightarrow 4s$, and $2p_{3/2} \rightarrow 3d$ core excitiations on Ar. The major goals are

- to study what role the accurate interaction energies in the decaying and final states of ICD and the nuclear dynamics during the decay play in shaping the ICD electron and KER spectra;
- to clarify what effect the presence of a chemically "softer" neighbour has on the ICD spectra.

We assume that the cascade is initiated by a broad resonant excitation so that the ground-state wave packet is transferred vertically to the PEC of the specific $2p \rightarrow nl$ core-excited state of Ar. The lifetime of these states is ∼6 fs [116] and, therefore, the resonant Auger decay will be nearly unaffected by the nuclear dynamics on the core-excited PEC. Due to these assumptions of instantaneous core excitation and resonant Auger decay, the nuclear dynamics of the whole cascade is restricted to the dynamics during the ICD process. For the full quantum mechanical simulation of the dynamics one requires accurate *ab initio* potential energy curves and ICD widths as the input.

The chapter is structured as follows. In the next section we provide the details of the computations of the potential energy curves and the decay widths of both Ar_2 and ArKr, as well as the description of the nuclear dynamics calculations. In Sec. 4.2 we discuss the properties of the potential energy curves, the nuclear dynamics during the resonant-Auger – ICD cascade, and the final ICD-electron and KER spectra of Ar_2. In Sec. 4.3 we discuss the influence of the partner atom on the PECs and the decay widths, as well as on the computed ICD-electron and KER spectra. The conclusions are given in Sec. 4.4.

4.1 Computational details

4.1.1 Potential energy curves

The ground-state potential curves of Ar_2 and ArKr were obtained using the coupled cluster singles and doubles and perturbative triples method (CCSD(T)) as implemented in the GAMESS-US package [137, 138]. The basis set used on Ar in Ar_2 was aug-cc-pV6Z [139] and an additional set of diffuse basis functions was added at the midpoint position between the two atoms. In the case of ArKr, the aug-cc-pV5Z basis set [131, 140] was used on both atoms. The exponents of the additional diffuse functions in both cases were taken to be the most diffuse s, p, d, f and g exponents from the respective basis sets (aug-cc-pV6Z in the case of Ar_2 and aug-cc-pV5Z in the case of ArKr). The minimum and the binding energy of the computed ground state potential energy curve of Ar_2 are $R_e = 3.80\,\text{Å}$ and $D_e = 11.5\,\text{meV}$, respectively, which is in good agreement with the experimental values of 3.76 Å and 12.3 meV [141]. In the case of ArKr, the computed equilibrium distance and binding energy are $R_e = 3.94\,\text{Å}$ and $D_e = 13.3\,\text{meV}$, respectively, which is also in good agreement with the experimental values of 3.9 Å and 16.0 meV [142].

The PECs of the ionised-excited states were computed using the configuration interaction (CI) method as implemented in the GAMESS-US computational package [143, 144]. The CI-expansion comprises all single and double excitations (CISD) from the reference configurations. The latter were constructed from all possible 1h-configurations in which the 8 valence orbitals of Ar_2 (converging to the $3s$ and $3p$ atomic orbitals of Ar at asymptotic distances) were occupied with 15 electrons. In the case of ArKr, the reference configurations were constructed from 13 electrons occupying 7 valence orbitals, converging to $3s$ and $3p$ of Ar and $4p$ of Kr (the $4s$ orbital of Kr was frozen in the calculation). The cc-pVDZ basis set [131] augmented with two diffuse s functions, two diffuse d functions and two compact d functions was used on Ar. The additional diffuse and compact basis functions were generated as an even-tempered sequence ($\xi = \alpha\beta^l$) from the most diffuse s and d and the most compact d exponents, respectively, with $\beta = 10$ and $l = \pm 1/2$ ($l = 1/2$ in the case of the compact exponents, and $-1/2$ for the diffuse exponents). The aug-cc-pVTZ basis set [140] was used on Kr.

The PECs of the low-lying members of the Rydberg series (namely, the $Ar^+(3p^{-2}4s)RG$ and $Ar^+(3p^{-2}3d)RG$ states) and of the higher-lying $Ar^+(3p^{-2}\,5s)RG$ satellites were found among the first 100 (Ar_2) and 200 (ArKr) roots of the CI matrix in all irreducible representations of the D_{2h} (Ar_2) and C_{2v} (ArKr) point groups, respectively. However, obtaining the PECs of the $Ar^+(3p^{-2}4d)RG$ Rydberg states was beyond our reach. First, this task requires the computation of a very large number of roots. Second, due to the high density of states at higher energies the recovery of the corresponding PECs from the data becomes extremely difficult. An alternative approach to the straightforward computation of these states is to model them. We have shown [145] that the PECs of higher satellites at the interatomic distances where the nuclear dynamics predominantly takes place can be fairly accurately reproduced by the PECs of the corresponding parent dicationic states. Therefore, the PECs of the $Ar^+(3p^{-2}4d)RG$ states were approximated by averages of the PECs of the parent $Ar^{2+}(3p^{-2})RG$ states.

The computation of the PECs of the final two-site dicationic states, as well as the one-site states used to approximate the higher-lying ionisation satellites was carried out using the same implementation of the CISD method and the same basis set as for the singly-ionised states. The reference space in the case of Ar_2 comprises all possible 2h-configurations with 14 electrons occupying the 8 valence orbitals (the $3s$ and $3p$ orbitals of each Ar atom). In the case of ArKr, the 2h-configurations were obtained by distributing 12 electrons on 7 valence orbitals (the $3s$ and $3p$ orbitals of Ar, and $4p$ of Kr). Two sets of reference spaces were constructed corresponding to the two possible spin multiplicities (singlet and triplet). At asymptotic distances the PECs of the ionisation satellites and two-site dicationic final states were adjusted to the correct asymptotic energies taken from the NIST database [130]. The NIST energies were averaged over all possible fine structure components since the spin-orbit coupling was not accounted for in our calculations.

4.1.2 Decay widths

The ICD widths were computed using the Fano-Stieltjes method, with the bound and continuum part of the corresponding resonance state constructed using the extended ADC(2) scheme for the one-particle propagator [98]. For this purpose we used on each atom an effective core potential (ECP) with $4s$, $4p$, $4d$ and $1f$ basis functions with 8 active valence electrons. The ECP was adjusted in energy to non-relativistic and scalar relativistic energies [146]. The basis was further augmented by $8s$, $8p$, $8d$, $5f$, and $3g$ diffuse functions on the atomic centres and additional sets of $3s$, $3p$, and $4d$ functions on 5 ghost centres on the interatomic axis. The diffuse functions were specifically designed for the computation of Rydberg and continuum states [147]. The computed decay widths of the ionisation satellites of Ar_2 and ArKr at the equilibrium distances of the two dimers and at the left turning points of the corresponding PECs are listed in Tables 4.1 and 4.2. The decay widths of the two $Ar^+(3p^{-2}5s)Kr$ states could not be obtained within the present approach. Therefore, in order to compute the ICD-electron and KER spectra of these states, these widths were approximated by averages of the widths of the corresponding states of g- and u-symmetry in Ar_2 (see Table 4.1).

In contrast to the computation of PECs using the CISD method, in the Fano-Stieltjes method the higher-lying ionisation satellites are still accessible. The projection on the bound states subspace simplifies the ionisation spectrum significantly, which facilitates the identification of the states in question. For the lowest Rydberg terms these widths vary between 47 and 1 meV corresponding to the lifetimes between 28 fs and 1.35 ps. For the higher states the widths become considerably smaller and range between 2.2 and 0.2 meV corresponding to the lifetimes between 0.6 and 6.6 ps. Therefore, the ICD rate decreases with the increase of the principal quantum number n of the excited electron, which is expected as the Rydberg orbitals become more diffuse for larger n's, resulting in a smaller overlap with the dicationic core and smaller ICD rates [4]. The widths also de-

Table 4.1: Computed ICD widths of the ionisation satellites of Ar_2 used to obtain the ICD spectra. The values are given at the equilibrium interatomic distance R_e and at the left turning point $R_{t.p.}$ whose position is shown in parentheses. The states for which $\Gamma(R_{t.p.})$ is missing are dissociative.

Ar^+Ar State	Term Symbol	$\Gamma(R_e)$, meV	$\Gamma(R_{t.p.})$, meV
$3p^{-2}\ [^1S]4s\ ^2S$	Σ_g^+	12.32	–
	Σ_u^+	12.83	–
$[^1D]3d\ ^2D$	Σ_g^+	47.27	80.43 (3.39 Å)
	Σ_u^+	37.37	74.66 (3.25 Å)
	Π_g	28.91	39.57 (3.63 Å)
	Π_u	35.20	–
	Δ_g	15.00	19.24 (3.20 Å)
	Δ_u	13.88	9.036 (3.09 Å)
$[^1D]3d\ ^2P$	Σ_g^-	11.63	–
	Σ_u^-	10.12	–
	Π_g	24.57	41.85 (3.12 Å)
	Π_u	28.13	–
$[^1S]3d\ ^2D$	Σ_g^+	1.04	–
	Σ_u^+	0.97	–
	Π_g	1.19	14.51 (3.17 Å)
	Π_u	1.79	11.51 (3.23 Å)
	Δ_g	4.36	23.60 (3.34 Å)
	Δ_u	4.36	14.22 (3.48 Å)
$[^1D]5s\ ^2D$	Σ_g^+	1.04	21.68 (2.85 Å)
	Σ_u^+	0.90	14.49 (2.82 Å)
	Π_g	0.33	5.89 (2.83 Å)
	Π_u	0.31	4.23 (2.92 Å)
	Δ_g	0.68	5.49 (2.79 Å)
	Δ_u	0.58	4.21 (2.78 Å)
$[^3P]5s\ ^2P$	Σ_g^-	2.24	15.13 (2.91 Å)
	Σ_u^-	1.95	11.55 (2.90 Å)
	Π_g	0.76	20.02 (2.93 Å)
	Π_u	0.82	11.94 (2.98 Å)
$[^1D]4d\ ^2P$	Σ_g^-	0.83	20.70 (2.75 Å)
	Σ_u^-	0.73	13.26 (2.75 Å)
	Π_g	0.59	10.82 (2.77 Å)
	Π_u	0.63	15.83 (2.77 Å)
$[^1D]4d\ ^2D$	Σ_g^+	1.22	14.23 (2.77 Å)
	Σ_u^+	0.85	7.840 (2.77 Å)
	Π_g	0.39	20.47 (2.77 Å)
	Π_u	0.43	20.50 (2.77 Å)
	Δ_g	0.72	14.52 (2.77 Å)
	Δ_u	0.70	13.54 (2.77 Å)
$[^1D]4d\ ^2F$	Σ_g^-	0.37	10.34 (2.75 Å)
	Σ_u^-	0.36	11.84 (2.75 Å)
	Π_g	0.31	8.15 (2.77 Å)
	Π_u	0.30	7.76 (2.77 Å)
	Δ_g	0.20	13.04 (2.77 Å)
	Δ_u	0.22	12.92 (2.77 Å)
	Φ_g	0.55	3.93 (2.75 Å)
	Φ_u	0.61	3.13 (2.75 Å)

Table 4.2: Computed ICD widths of the ionisation satellites of ArKr used to obtain the ICD spectra. The values are given at the equilibrium interatomic distance R_e and at the left turning point $R_{t.p.}$ whose position is shown in parentheses. The states for which $\Gamma(R_{t.p.})$ is missing are dissociative.

$\mathrm{Ar^+Kr}$ state	Term symbol	$\Gamma(R_e)$, meV	$\Gamma(R_{t.p.})$, meV
$3p^{-2}[^1D]4s\,^2D$	Σ^+	10.34	–
	Π	9.15	–
	Δ	4.91	9.71 (3.51 Å)
$[^3P]3d\,^2D$	Σ^+	5.46	20.34 (3.48 Å)
	Π	4.33	4.85 (3.88 Å)
	Δ	2.97	–
$[^1S]4s\,^2S$	Σ^+	14.81	–
$[^1D]3d\,^2D$	Σ^+	44.72	84.97 (3.44 Å)
	Π	34.95	–
	Δ	16.05	21.15 (3.44 Å)
$[^1D]3d\,^2P$	Σ^-	11.26	–
	Π	29.22	33.71 (2.87 Å)
$[^1S]3d\,^2D$	Σ^+	0.95	–
	Π	1.25	–
	Δ	3.06	18.89 (3.38 Å)
$[^3P]5s\,^2P$	Σ^-	1.48	12.71 (2.84 Å)
	Π	0.57	11.28 (3.00 Å)
$[^1D]5s\,^2D$	Σ^+	0.62	12.10 (2.90 Å)
	Π	0.21	4.43 (2.90 Å)
	Δ	0.44	3.83 (2.84 Å)
$[^1D]4d\,^2P$	Σ^-	0.67	12.26 (2.89 Å)
	Π	0.53	6.61 (2.91 Å)
$[^1D]4d\,^2D$	Σ^+	0.87	6.63 (2.91 Å)
	Π	0.36	16.67 (2.91 Å)
	Δ	0.60	5.28 (2.91 Å)
$[^1D]4d\,^2F$	Σ^-	0.33	5.88 (2.89 Å)
	Π	0.23	5.63 (2.91 Å)
	Δ	0.18	12.67 (2.91 Å)
	Φ	0.47	2.60 (2.89 Å)

pend strongly on the interatomic distance R becoming larger as R decreases. At large R they behave as $1/R^6$ and grow even faster about R_e due to the effect of orbital overlap [148].

The decay widths were computed only down to 3 Å for all ionisation satellites of interest. For the nuclear dynamics simulations, however, it was necessary to extrapolate the decay widths to shorter internuclear distances. In the case of the fast satellites (correlating with the $\mathrm{Ar}^+(3p^{-2}3d,\,4s)$ states), the decay width was set to a constant value below 3 Å. This is justified by the fact that the decay is much faster than the nuclear dynamics. It occurs predominantly around the respective equilibrium distance R_e and therefore, the wave packet does not reach this range of internuclear distances. In the case of the slow satellites (correlating with the $\mathrm{Ar}^+(3p^{-2}5s,\, 4d)$ states), the decay width was quadratically extrapolated in order to account for its enhancement at shorter internuclear distances [148]. In this case the decay occurs mostly in the vicinity of the left turning points $R_{t.p.}$ of the respective PECs, which lie below 3 Å for all states of interest (see Tables 4.1 and 4.2). Hence, the value of the decay width below R_e is crucial for obtaining accurate ICD-electron and KER spectra.

Within the present method partial decay widths, needed for the nuclear dynamics calculations, cannot be reliably computed. Instead, they were assumed to be equal and were obtained by dividing the total decay width of the i-th ICD state by the number of channels, i.e. $\Gamma^i_{f_k}(R) = \Gamma_i(R)/N_c$. In the case of both Ar_2 and ArKr there are 18 decay channels.

4.1.3 Nuclear dynamics calculations

The potential curves and decay widths serve as input for the nuclear dynamics calculation. The PECs are the R-dependent potential energy operators $\hat{V}_{i/d_m/f_k}$, whereas the R-dependent decay widths enter both differential equations in Eq. (2.3.8) as the operators $\hat{\Gamma}_m(R)$ and $\hat{W}_{d_m \to f_k}(R)$. The time-evolution of the nuclear wave packets (i.e. the system Eq. (2.3.8)) was computed using the Lanczos-Arnoldi algorithm [149] as implemented in the multi-configuration time-dependent Hartree (MCTDH) package [150, 151]. The computations were done for the internuclear distances between 1.5 Å and 11.73 Å using fast Fourier transform (FFT) with 1024 points. The nuclear wave packets of the decaying and final states were propagated until the norm of the wave function of the decaying state becomes of the order of 10^{-8}. The propagation times for different decaying states vary between 700 fs and 200 ps in the case of Ar_2, and between 500 fs and 150 ps in the case of ArKr.

The ICD-electron spectra were computed from the final nuclear wave packets as explained in Sec. 2.3. The KER spectra were computed using the mirror image principle Eq. (2.3.13). Note that the asymptotic energy of the final two-site dicationic states $E_f(\infty)$ is the same for all 18 channel $\mathrm{Ar}^+\mathrm{RG}^+$ belonging to a given rare gas dimer.

The total ICD-electron and KER spectra of a cascade initiated by a particular core excitation were calculated as weighted sums of the spectra belonging to the ionisation satellites populated in the resonant Auger step. The respective weights for Ar_2 and ArKr were obtained from the known branching ratios of this process in isolated Ar [38]. This assumption is confirmed by the experimental results for Ar_2 reported in Ref. [46], which show that even in the argon dimer the resonant Auger decay is mostly of local nature. Finally, the total ICD-electron and KER spectra were convolved with Gaussians of FWHM 1.24 eV and 0.64 eV, respectively, to account for the experimental resolution [46, 47].

4.2 ICD following resonant core excitation of Ar in Ar_2

4.2.1 Potential energy curves of Ar_2

In the following the properties of the PECs of all states of Ar_2 relevant for the nuclear dynamics, namely the ground state of the neutral dimer Ar_2, the ionisation satellites $Ar^+(3p^{-2}\, nl)Ar$ populated after the resonant Auger decay, and the final dicationic states of the ICD process $Ar^+(3p^{-1})Ar^+(3p^{-1})$, will be discussed. The PECs of interest are presented in Fig. 4.1.

The ground-state PEC of Ar_2 (see Fig. 4.1(a)) is characterised by a shallow minimum of $D_e = 11.5\,\text{meV}$ located at $R_e = 3.8\,\text{Å}$. This potential supports seven vibrational levels. It is assumed that the argon dimer is in its lowest vibrational state which corresponds to the experimental conditions. Therefore, the initial wave packet is taken to be the respective nodeless eigenfunction of the nuclear Hamiltonian and has an approximately Gaussian shape.

The initial ICD states of interest are ionisation satellites populated in the RA step. Due to a large number of such states (see Table 4.3), it is computationally very demanding to take them all into account in calculating the ICD spectra. Therefore, we restrict the initial ICD states to include only the spin doublet satellites originating from the states populated by more than 3 % in the RA decay of isolated Ar (see Table 4.1). These states form more than 60 % of all states populated in the RA decay of the $2p_{3/2} \rightarrow 3d$ core excitation that can further

Table 4.3: Ionisation satellites of Ar atom populated in the resonant Auger decay following the $2p_{3/2} \rightarrow 4s$, $2p_{1/2} \rightarrow 4s$ and $2p_{3/2} \rightarrow 3d$ core excitations [38]. Only the states which are allowed to undergo ICD in Ar_2 and ArKr are presented. A horizontal line separates the two additional ICD-active states in ArKr. The excitation energies are taken from the NIST database [130].

		Intensity, %		
Ionisation satellite of Ar	Excitation energy, eV	$2p_{3/2}^{-1}4s$	$2p_{1/2}^{-1}4s$	$2p_{3/2}^{-1}3d$
$3p^{-2}$ $[^1D]4s\,^2D$	34.20	25	28	2
$[^3P]3d\,^2D$	34.46	21	16	-
$[^1S]4s\,^2S$	36.50	10	9	-
$[^1D]3d\,^2D$	37.15	-	5.62	12
$[^1D]3d\,^2P$	37.40	-	3.38	13
$[^1S]3d\,^2D$	38.04	-	2	7
$[^3P]5s\,^{2,4}P$	38.33 (^4P), 38.49 (^2P)	5	5	-
$[^3P]4d\,^4D$	38.55	-	-	7
$[^1D]3d\,^2S$	38.58	-	-	
$[^3P]4d\,^4P$, $^{2,4}F$	38.90 (^4P), 38.96 (^2F), 38.78 (^4F)	-	-	8
$[^1D]5s\,^2D$	40.04	5	5	3
$[^1D]4d\,^2P$, ^2D, ^2F	40.49 (^2P), 40.53 (^2D), 40.58 (^2F)	-	-	27
$[^3P]5d\,^4D$, ^4F	40.56 (^4D), 40.67 (^4F)	-	-	
$[^3P]5d\,^2P$, ^2D	41.17 (^2P), 41.12 (^2D)	-	-	7
$[^1D]4d\,^2S$	41.21	-	-	
$[^1D]5d\,^2G$, ^2D, ^2F	42.32 (^2P), 42.37 (^2D), 42.40 (^2F)	-	-	4
$[^1S]5s\,^2S$	42.42	1	-	-
$[^1S]4d\,^2D$	42.97	-	-	5
$[^1S]5d\,^2D$	44.78	-	-	1

decay via ICD. This proportion rises to about 75 % for the $2p_{3/2,1/2} \rightarrow 4s$ core excitations (see Table 4.3). As Figs. 4.4 and 4.5 show, this selection is sufficient for accurately reproducing the experimental spectra. The PECs of these states are shown in Fig. 4.1.

One can better understand the structure of the ICD-electron and KER spectra if the interatomic decay of the low- and high-lying Rydberg states populated in the RA step is considered separately. The former comprise the satellites correlating with the $Ar^+(3p^{-2}[^1S]4s\,^2S)Ar$, $Ar^+(3p^{-2}[^1D]3d\,^2D)Ar$, $Ar^+(3p^{-2}[^1D]3d\,^2P)Ar$, and $Ar^+(3p^{-2}[^1S]\ 3d\ ^2D)Ar$ states at asymptotic distances. Their PECs possess shallow minima located between 3.37 and 4.90 Å with interaction energies ranging between 36 and 129 meV. At the equilibrium distance, the ICD lifetimes

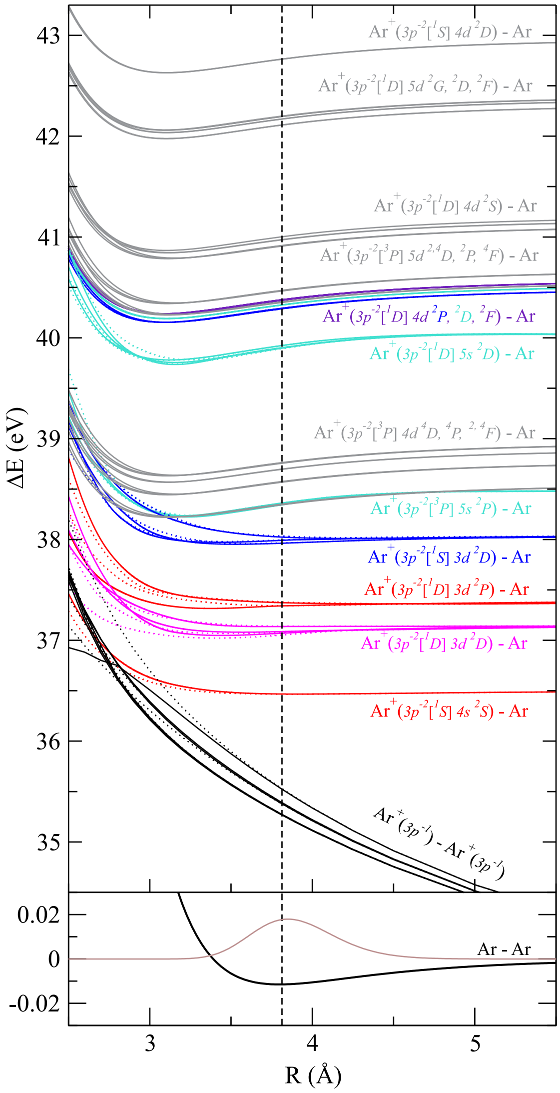

Figure 4.1: Potential energy curves of Ar_2; (lower panel) the ground-state PEC and ground-state wave packet density of Ar_2; (upper panel) the black curves represent the final repulsive two-site dicationic states $Ar^+(3p^{-1})Ar^+(3p^{-1})$; the red and pink curves represent the lowest fast-decaying ionisation satellites, the blue and violet curves represent the higher slow-decaying satellites (see Table 4.1 for the corresponding decay widths). The ICD-active states which were not included in the dynamics calculation, but are populated after the resonant Auger decay are shown in grey.

of these states range between 28 and 130 fs being an order of magnitude smaller than the characteristic vibrational periods (0.6 ÷ 1.3 ps). Therefore, these intermediate states are expected to decay fast with little dynamics taking place during the decay. The PECs of the higher Rydberg states correlating with the $Ar^+(3p^{-2}[^3P]5s\,^2P)Ar$, $Ar^+(3p^{-2}[^1D]5s\,^2D)Ar$, $Ar^+(3p^{-2}[^1D]4d,\ ^2P,\ ^2D,\ ^2F)Ar$

satellites at asymptotic distances have somewhat different binding properties compared to the lower Rydberg states. These PECs are generally characterised with a deeper potential well, with binding energies between 250 meV and 340 meV, and minima shifted to shorter internuclear distances (3.08 – 3.24 Å). This can be explained by smaller repulsion between the excited electron occupying a diffuse high Rydberg orbital and the neutral Ar neighbour [145]. As a result, these states have smaller characteristic vibrational periods (180 – 250 fs). These, in turn, are by an order of magnitude shorter than the relevant ICD lifetimes at R_e. Therefore, the decay of these states is expected to be substantially influenced by the vibrational motion of the nuclei. The decay takes place mostly at shorter internuclear distances, where the respective width is an order of magnitude larger compared to its value at R_e (see Table 4.1).

The final ICD states are presented in the upper panel of Fig. 4.1 (black curves). There are 12 two-site final dicationic states of the $\mathrm{Ar}^+(3p^{-1})\mathrm{Ar}^+(3p^{-1})$ with symmetries $^1\Sigma_g^+(2)$, $^3\Sigma_u^+(2)$, $^1\Sigma_u^-$, $^3\Sigma_g^-$, $^1\Pi_g$, $^3\Pi_g$, $^1\Pi_u$, $^3\Pi_u$, $^1\Delta_g$, $^3\Delta_u$, resulting in 18 decay channels in total. Their PECs are all repulsive in the range of internuclear distances relevant for the decay, and behave as R^{-1} at large distances due to the dominant Coulomb repulsion between the two positively charged ions Ar^+. Therefore, ICD will be followed by a fast dissociation of the dimer.

4.2.2 Nuclear dynamics during the ICD step

In order to obtain a clearer picture of the role nuclear dynamics play during the final ICD step, we will consider the fast- and slow-decaying ionisation satellites separately. In Sec. 4.2.1 two groups of states, namely the low and high Rydberg states, have already been defined. The low Rydberg states $\mathrm{Ar}^+(3p^{-2}3d)\mathrm{Ar}$ and $\mathrm{Ar}^+(3p^{-2}4s)\mathrm{Ar}$, fall into the group of the fast-decaying states, while the higher Rydberg states, $\mathrm{Ar}^+(3p^{-2}4d)\mathrm{Ar}$ and $\mathrm{Ar}^+(3p^{-2}5s)\mathrm{Ar}$, are the slow-decaying states. The ICD-electron and KER spectra are profoundly different for these two groups. This difference can be demonstrated by examining the ICD-electron spectra of two specific satellites.

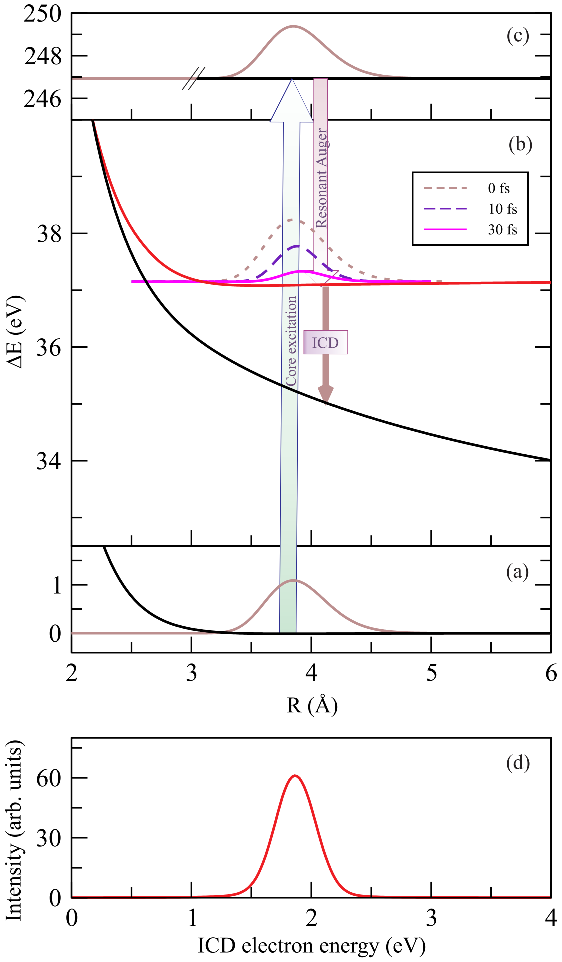

Figure 4.2: Resonant-Auger – ICD cascade of the $2p_{3/2} \rightarrow 3d$ excitation proceeding with a fast ICD step through the $\mathrm{Ar}^+(3p^{-2}[^1D]3d\,^2D\ ^2\Sigma_g^+)\mathrm{Ar}$ satellite. (a) Ground-state PEC and the corresponding ground-state nuclear wave packet density. (c) A resonant core excitation of the initial wave packet to the $\mathrm{Ar}(2p_{3/2} \rightarrow 3d)\mathrm{Ar}$ state and subsequent instantaneous resonant Auger decay. (b) ICD of the $\mathrm{Ar}^+(3p^{-2}[^1D]3d\ ^2D\ ^2\Sigma_g^+)\mathrm{Ar}$ satellite; the $\mathrm{Ar}^+(3p^{-1})\mathrm{Ar}^+(3p^{-1})\ ^1\Delta_g$ final state is populated. (d) ICD-electron spectrum of the $\mathrm{Ar}^+(3p^{-2}[^1D]3d\,^2D\ ^2\Sigma_g^+)\mathrm{Ar}$ state.

RA-ICD cascade via a fast-decaying state

First, consider the decay cascade proceeding via the $\mathrm{Ar}^+(3p^{-2}[^1D]3d\,^2D\,^2\Sigma_g^+)\mathrm{Ar}$ ionisation satellite which is shown in Fig. 4.2. The PEC of this state is bound by 70 meV at 3.57 Å and supports 25 vibrational levels. At the equilibrium distance, the characteristic vibrational period is about 600 fs, which is an order of magnitude larger than the ICD lifetime of 28 fs. Therefore, the decay outpaces the vibrational motion and, thus, ICD occurs essentially at the internuclear separation at which the state was initially populated, i.e. at the equilibrium distance of the ground state. As one can see from the time evolution of the nuclear wave packet, presented in Fig. 4.2(b), its initial shape is not distorted by the vibrational motion, and the position of its maximum is also unaltered during the decay. The electron spectrum of this satellite is depicted in Fig. 4.2(d). It has a nearly Gaussian shape with a maximum at the electronic energy of 1.86 eV. It corresponds to the difference between the energy of the decaying state and that of the final electronic state at the equilibrium distance.

RA-ICD cascade via a slow-decaying state

Let us focus next on the cascade proceeding via the $\mathrm{Ar}^+(3p^{-2}[^1D]5s\,^2D\,^2\Sigma_g^+)\mathrm{Ar}$ satellite shown in Fig. 4.3. The PEC of this state possesses a deeper minimum of 307 meV located at 3.15 Å. It supports 39 vibrational levels and the characteristic time of vibrational motion was estimated to be about 200 fs. At R_e the ICD lifetime is 1270 fs, i.e. an order of magnitude larger than the vibrational period. As a result, after the state is populated, the wave packet at first becomes broader and shifts towards shorter internuclear distances. At later times the wave packet acquires a characteristic multinodal structure with a dominant maximum located close to the left turning point (see Fig. 4.3(b)). Since the decay rate increases fast with the decreasing interatomic distance, ICD occurs mostly in the vicinity of the left turning point of the PEC, where the corresponding rate is approximately 20 times larger than at R_e. The resulting electron spectrum is shown in Fig. 4.3(d). The effect of nuclear dynamics on the spectrum is clearly visible in the dominant peak at 3.44 eV which corresponds to ICD taking place when the two argon atoms are approximately 2.9 Å apart, i.e. at the left turning point. The shoulder at 4.5 eV is a vestige of the decay which happened in the vicinity of R_e. Similar evolution of the vibrational wave packet during ICD was experimentally observed and confirmed numerically for the slow-decaying satellite states of the He dimer [152, 153].

The states converging to $\mathrm{Ar}^+(3p^{-2}[^1S]3d\,^2D)\mathrm{Ar}$ are an exceptional case which does not fit in the picture presented above. Their ICD lifetimes are rather long (300 – 1400 fs) and thus comparable to the characteristic time of vibrational motion (500 – 1400 fs). However, since the minima of the corresponding PECs lie close to R_e, the effect of nuclear dynamics on the ICD spectra is rather small.

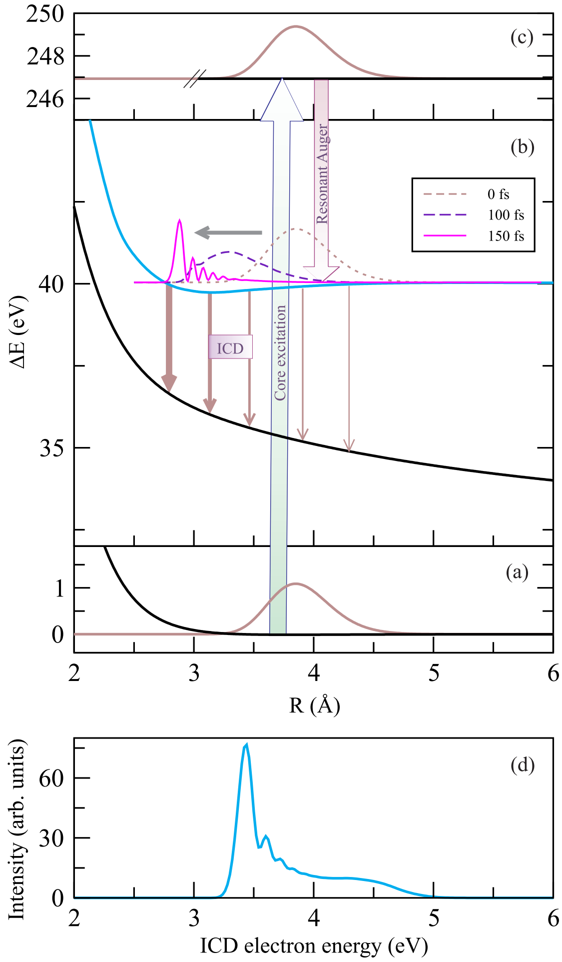

Figure 4.3: Resonant-Auger – ICD cascade of the $2p_{3/2} \rightarrow 3d$ excitation proceeding with a slow ICD step through the $\mathrm{Ar}^+(3p^{-2}[^1D]5s\,^2D\ ^2\Sigma_g^+)\mathrm{Ar}$ satellite. (a) Ground-state PEC and the corresponding ground-state nuclear wave packet density (c) A resonant core excitation of the initial wave packet to the $\mathrm{Ar}(2p_{3/2} \rightarrow 3d)\mathrm{Ar}$ state and subsequent instantaneous resonant Auger decay. (b) ICD of the $\mathrm{Ar}^+(3p^{-2}[^1D]5s\,^2D\ ^2\Sigma_g^+)\mathrm{Ar}$ satellite; the $\mathrm{Ar}^+(3p^{-1})\mathrm{Ar}^+(3p^{-1})\ ^1\Delta_g$ final state is populated. (d) ICD-electron spectrum of the $\mathrm{Ar}^+(3p^{-2}[^1D]5s\,^2D\ ^2\Sigma_g^+)\mathrm{Ar}$ state.

4.2.3 ICD-electron and KER spectra

In this section we present and discuss the total ICD-electron and KER spectra of Ar dimer produced following the decay of the $2p_{3/2} \rightarrow 4s$, $2p_{1/2} \rightarrow 4s$, and $2p_{3/2} \rightarrow 3d$ parent core excitations of Ar. The resulting spectra are shown in Figs. 4.4, 4.5. It can be seen from Fig. 4.4 that the electron spectra for all three parent excitations possess a double peak structure. The peak at lower energies (0 - 3 eV) originates mainly from the ICD of the four lowest ionisation satellites: $\mathrm{Ar}^+(3p^{-2}[^1S]4s\,^2S)\mathrm{Ar}$,

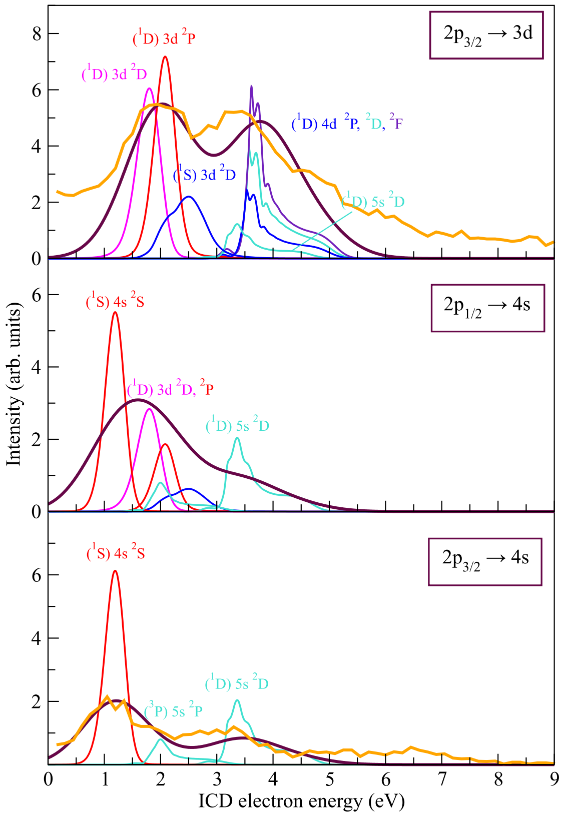

Figure 4.4: ICD-electron spectra obtained in the RA-ICD cascade following the Ar $(2p_{3/2} \rightarrow 4s)$Ar (lowermost panel), Ar$(2p_{1/2} \rightarrow 4s)$Ar (middle panel), and Ar$(2p_{3/2} \rightarrow 3d)$Ar (uppermost panel) core excitation. The dark red curves in all panels represent the total ICD spectra corresponding to the particular core excitation. Experimental data is available for the Ar$(2p_{3/2} \rightarrow 4s)$Ar and Ar$(2p_{3/2} \rightarrow 3d)$Ar excitation (orange curves) [47]. The experimental spectra were scaled so that the intensities of the lower-energy peaks coincide. The electron spectra resulting from the decay of the individual satellites contributing to the total spectrum of each core excitation are also presented (the color scheme follows that of the PECs in Fig. 4.1).

$\mathrm{Ar}^+(3p^{-2}[^1D]3d\,^2P,\,^2D)$Ar, and $\mathrm{Ar}^+(3p^{-2}[^1S]3d\,^2D)$Ar, populated in the strict spectator Auger transition. The second peak is located at energies between 3 and 6 eV. It is predominantly due to the ICD of the higher Rydberg states: $\mathrm{Ar}^+(3p^{-2}[^3P]5s\,^2P)$Ar, $\mathrm{Ar}^+(3p^{-2}[^1D]5s\,^2D)$Ar, $\mathrm{Ar}^+(3p^{-2}[^1D]4d\ ^2P,\ ^2D,\ ^2F)$Ar, which are populated in a shake-up process during the resonant Auger step [38]. The relative intensities of the peaks reflect, therefore, the relative probability of shake-up processes in the RA decay of a particular parent state.

If one considers only the populations of the satellites decaying by ICD, the

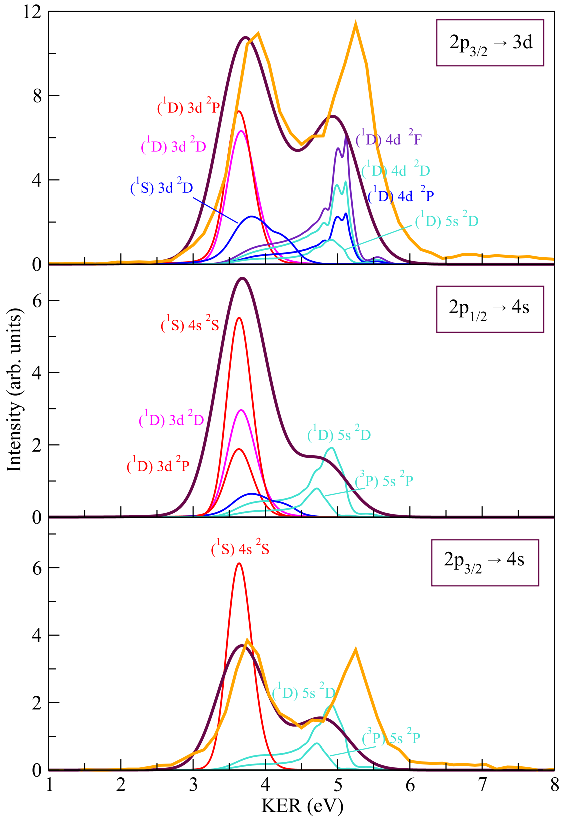

Figure 4.5: KER spectra obtained in the RA-ICD cascade following the Ar($2p_{3/2} \rightarrow 4s$)Ar (lowermost panel), Ar($2p_{1/2} \rightarrow 4s$)Ar (middle panel), and Ar($2p_{3/2} \rightarrow 3d$)Ar (uppermost panel) core excitation. The spectra were obtained using the mirror image principle (see Eq. (2.3.13)). The dark red curves in all panels represent the KER spectra corresponding to the particular core excitation. The orange lines are the experimental KER spectra for the Ar($2p_{3/2} \rightarrow 4s$)Ar and Ar($2p_{3/2} \rightarrow 3d$)Ar core excitation [46, 49]. The experimental spectra were scaled so that the intensities of the lower-energy peaks coincide. The KER spectra of the satellites contributing to the total spectrum of each core excitation are also presented (the color scheme follows that of the PECs in Fig. 4.1)

ratios of the strict spectator to shake-up probabilities for the $2p_{3/2} \rightarrow 4s$, $2p_{1/2} \rightarrow 4s$, and $2p_{3/2} \rightarrow 3d$ parent states are approximately 2:1, 3:1, 1:1. This is clearly reflected in the resulting ICD-electron spectra. The low-energy peak dominates the high energy one for the $2p_{3/2} \rightarrow 4s$ and $2p_{1/2} \rightarrow 4s$ parent states and is more pronounced in the former case. Unlike these spectra, the two peaks in the electron spectrum of the $2p_{3/2} \rightarrow 3d$ core excitation have almost equal intensities, a result of a very large shake-up probability for this state [36, 48].

The KER spectrum carries information about the internuclear distances at which ICD takes place and is, therefore, sensitive to the ratio of the electronic decay lifetime to the vibrational period. The Ar_2 spectra corresponding to the parent states in question are shown in Fig. 4.5. They possess a double-peak structure as the respective ICD-electron spectra, although for a different physical reason. In the electron spectra this structure reflects the differences in the populations and excitation energies of the satellite states following the resonant Auger decay, while in the KER spectra it is a sign that the ICD of different satellite states proceeds with notably different rates. In our previous analysis we showed that lower Rydberg states decay fast with interatomic distances being close to R_e. This results in the peak located at energies between 2.5 and 4.5 eV. The longer ICD lifetimes of the higher Rydberg states lead to the decay close to the left turning point of the corresponding PECs, i.e. at shorter interatomic distances, resulting in the peak between 4.5 and 6 eV.

Comparison of the computed ICD-electron and KER spectra with experimental results

The computed ICD-electron and KER spectra of the $2p_{3/2} \to 4s$ and $2p_{3/2} \to 3d$ parent states are in good agreement with the experimental results [46, 47, 49] as is evident from Figs. 4.4 and 4.5. Both electron and KER experimental spectra show the double-peak structure discussed above. There are, however, certain discrepancies in the positions of the computed and measured peaks. In particular, in the computed ICD-electron spectrum corresponding to the $\mathrm{Ar}(2p_{3/2} \to 3d)\mathrm{Ar}$ parent core excited state the two peaks are shifted by 85 meV and 315 meV, respectively, to higher energies relative to the experimental spectrum. A shift of ~180 meV to higher energies is clearly visible for the two peaks in the ICD-electron spectrum corresponding to the $\mathrm{Ar}(2p_{3/2} \to 4s)\mathrm{Ar}$ parent excitation. Comparing the experimental and theoretical KER spectra, one sees that the theoretical spectrum is shifted to smaller energies of the emitted ionic fragments. In the case of the $\mathrm{Ar}(2p_{3/2} \to 3d)\mathrm{Ar}$ excitation, the shifts of the low and high Rydberg peaks are 170 meV and 320 meV, while for the $\mathrm{Ar}(2p_{3/2} \to 4s)\mathrm{Ar}$ excitation the respective shifts are 240 meV and 480 meV.

As one can see, from the total ICD-electron spectra corresponding to all considered core-excited states (see Fig. 4.4) the peaks corresponding to the lower-energy satellites are shifted less than the peaks corresponding to the higher-energy ones. This is indicative of the different sources of error in the computation of the decay of the respective satellites. The KER spectra (see Fig. 4.5) show a similar behaviour. However, due to energy conservation (see Eq. (2.3.13)) the shifts of the peaks have signs opposite to the shifts in the electron spectra.

Sources of error in the computed ICD-electron and KER spectra

In the following, we will discuss the sources of error in the computed ICD-electron and KER spectra of Ar_2 considering the fast- and the slow-decaying states separately.

For the fast-decaying satellites the resulting peaks in the ICD-electron spectrum are sensitive to

- the quality of the ground-state vibrational wave packet,
- the relative populations of the satellite states in the RA decay,
- the energy difference between the decaying and final states close to the equilibrium distance R_e.

It is clear from Fig. 4.2 (see also Ref. [123]) that an error in the initial wave packet immediately translates into an error in the spectral peak. As we mentioned earlier, our ground state PEC compared to a benchmark computation has a minimum shifted by 0.04 Å towards larger interatomic distances and also underestimates the binding by 0.8 meV. The combined effect would be to shift the maximum of the respective wave packet to larger interatomic distances shifting the electron peaks to larger energies by a few tens of meV compared to the benchmark wave packet. The effect of the relative populations is relevant in the case of the $\mathrm{Ar}(2p_{3/2} \rightarrow 3d)\mathrm{Ar}$ parent excitation. The low-energy peak is composed of two peaks of nearly equal intensity arising due to ICD of the $\mathrm{Ar}^{+}(3p^{-2}[{}^{1}D]3d\,{}^{2}P,\,{}^{2}D)\mathrm{Ar}$ states (see Fig. 4.4). One can see that by changing the relative intensity of these constituent peaks one would shift the combined peak by at most 200 meV. However, as discussed at the end of Sec. 4.1.3, the atomic intensities we used in this work were experimentally shown to be accurate in the dimer. The errors in the energies of the decaying and the final states around R_e are less than 100 meV. A comparable value will be an upper boundary on their energy difference. One can see that the difference between the corresponding peaks in the theoretical and experimental spectra in

Fig. 4.4 is a few tens of meV agreeing well with the estimates made above.

The position of the low-energy peak in the KER spectrum originating from the lower Rydberg states depends on

- the quality of the ground-state vibrational wave packet,
- the accuracy of the PECs of the final states around R_e.

In the previous paragraph we concluded that both errors will be below a hundred meV. The total observed shift is 170 meV which again agrees with our estimate (see Fig. 4.5).

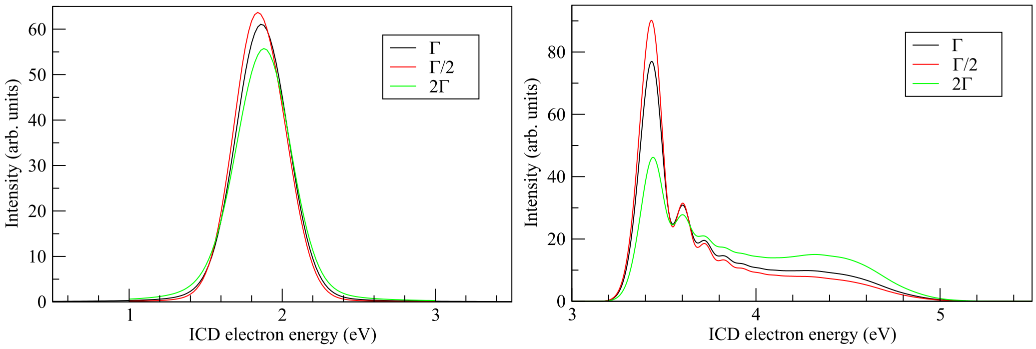

Figure 4.6: Partial ICD-electron spectra following the decay of the $\mathrm{Ar}^+(3p^{-2}[^1D]3d\,^2D\ ^2\Sigma_g^+)$ (left) and $^+(3p^{-2}[^1D]5s\,^2D\ ^2\Sigma_g^+)$ (right) state to the $\mathrm{Ar}^+(3p^{-1})\mathrm{Ar}^+(3p^{-1})\ ^1\Delta_g$ final state. The original ICD-electron spectrum (in black) is compared to the ICD-electron spectra obtained by scaling the decay width with a constant factor k.

The analysis of the computational errors in the case of the slow-decaying satellites is much more complicated than in the case of the fast-decaying ones. The accuracy in the positions of the corresponding peaks in both ICD-electron and KER spectra is primarily determined by

- the accuracy of the positions of the left turning points on the PECs in question,
- the respective ICD rates.

In Fig. 4.3 we show the electron spectrum corresponding to a slow decay from a single satellite state. It has a pronounced maximum at low energies corresponding to the decay around the left turning point and another maximum at higher energies due to the decay around the ground state equilibrium distance. Since the *ab initio* calculation of decay widths, especially for interatomic processes is difficult, one

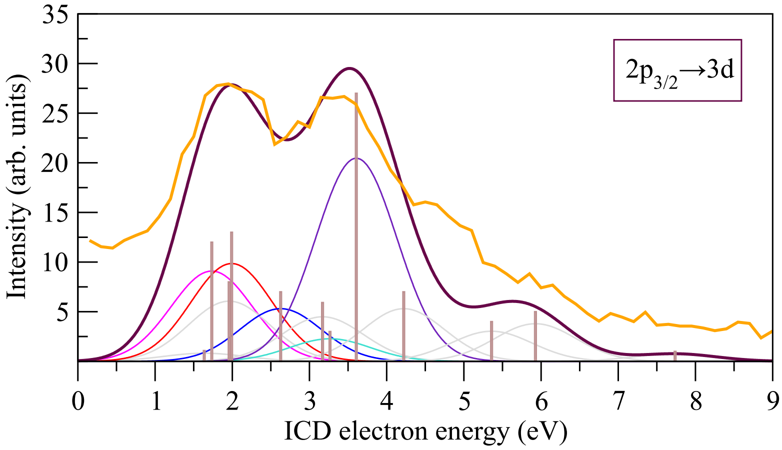

Figure 4.7: ICD-electron spectrum following the resonant Auger decay of the Ar($2p_{3/2} \rightarrow 3d$) core excitation in Ar_2. The dark red line represents the theoretical spectrum (see text for details). The total spectrum was convolved with a Gaussian of FWHM 1.24 eV to account for the experimental resolution. The experimental ICD-electron spectrum [47] is given in orange.

cannot expect the computed widths to be highly accurate (see Refs. [106, 118, 154]). As shown in Fig. 4.6, a larger ICD rate leads to the reduction in the effect of nuclear dynamics, enhancing the spectrum in the higher-energy region. On the contrary, smaller ICD rate accentuates the effect of nuclear dynamics, enhancing the spectrum in the lower-energy part of the peak [154]. These errors may, therefore, produce a shift in the positions of the slow satellite peaks in the total electron and KER spectra, but they will have almost no effect on the intensity and the position of the peaks in the case of the fast satellites (see Fig. 4.6). We also introduce an error in the turning point positions by modelling the higher satellite PECs with the PECs of the respective dicationic states. Although due to the diffuse nature of the Rydberg electron there is a good correspondence between the two types of PECs, the residual screening of the dicationic core by the Rydberg electron leads to differences in the slope of the repulsive part of the potentials [145].

Finally, the effect of omitting some ICD states from the calculations will be briefly discussed (see Fig. 4.1 for the satellites in question, their PECs are shown in grey). The largest deviation from the experiment is observed for the ICD spectra of the $2p_{3/2} \rightarrow 3d$ parent state where the neglected satellites carry up to 30% of the intensity. Therefore, in order to estimate the latter effect, the ICD-electron spectrum following the decay of the Ar($2p_{3/2} \rightarrow 3d$) core excitation in

Table 4.4: Ionisation satellites of Ar_2 used in constructing the ICD-electron spectrum originating from the $Ar(2p_{3/2} \rightarrow 3d)Ar$ core excitation. The estimated energies of the ICD electron E_e and the respective intensities taken from Ref. [38] are also given.

Ar^+Ar state		E_e, eV	Intensity
$3p^{-2}$	$[^1D]3d\,^2D$	1.734	12
	$[^1D]3d\,^2P$	1.992	13
	$[^1S]3d\,^2D$	2.627	7
	$[^3P]4d\,^4D$	1.636	1.08
	$[^1D]3d\,^2S$	3.170	5.92
	$[^3P]4d\,^4P,\ ^{2,4}F$	1.960	8
	$[^1D]5s\,^2D$	3.266	3
	$[^1D]4d\,^2P,\ ^2D,\ ^2F;\ [^3P]5d\,^4D,\ ^4F$	3.606	27
	$[^3P]5d\,^2D,\ ^2P;\ [^1D]4d\,^2S$	4.221	7
	$[^1D]5d\,^2G,\ ^2D,\ ^2F$	5.358	4
	$[^1S]4d\,^2D$	5.927	5
	$[^1S]5d\,^2D$	7.737	1

Ar_2 has been simulated in a simple way including all possible states populated in the resonant Auger step. For this purpose, only knowledge of the decay widths at the equilibrium distance, and the PECs of the decaying and final states was used. In the case of the omitted satellites, neither their PECs, nor the respective decay widths were available. As a result, the PECs were approximated by averages of the PECs of the parent dicationic states. Subsequently, the states were divided into fast- and slow-decaying based on the consideration that the ICD rate decreases with the increase of the principal quantum number n of the excited electron (see Sec. 4.1.2). Thus, all $Ar^+(3p^{-2}3d, 4s)Ar$ ionisation satellites fell into the group of the fast-decaying states, whereas the $Ar^+(3p^{-2}4d, 5s, 5d)Ar$ states were assumed to be slow-decaying. The total ICD-spectrum shown in Fig. 4.7 was obtained by evaluating the energies of the emitted ICD electrons as differences between the energies of the decaying and the final states as follows. For the fast-decaying states this difference was estimated at the equilibrium distance R_e, whereas for the slow-decaying states it was taken as the difference at the left turning points $R_{t.p.}$ of the respective PECs. The satellites used to obtain the spectrum comprise all ICD-active states populated after the resonant Auger decay of the Ar($2p_{3/2} \rightarrow 3d$) core excitation. These states as well as the respective estimated ICD-electron energies are given in Table 4.4. In comparison with the spectrum shown in Fig. 4.4, the one in Fig. 4.7 has a triple-peak structure. It can be better understood if the omitted satellites are divided according to their energy. As can be seen from Fig. 4.1 these states form three groups lying in the energy ranges 38 ÷ 39 eV, 40 ÷ 42 eV and above 42 eV, respectively. The states in the first group, namely, Ar($3p^{-2}[^3P]4d\,^4D$)Ar and Ar($3p^{-2}[^3P]4d\,^4P$, $^{2,4}F$)Ar contribute to the lowest-energy peak in the ICD-electron spectrum. The decay of the states in the second group, Ar($3p^{-2}[^1D]3d\,^2S$)Ar, Ar($3p^{-2}[^3P]5d\,^2D$, ^2P)Ar, and Ar($3p^{-2}[^1D]4d\,^2S$)Ar, enhances the second peak in the spectrum. The highest Rydberg states, namely, Ar($3p^{-2}[^1D]5d\,^2G$, ^2D, ^2F)Ar, Ar($3p^{-2}[^1S]4d\,^2D$)Ar and Ar($3p^{-2}[^1S]5d\,^2D$)Ar would decay emitting electrons of energies above 5 eV, which would account for the difference between the theoretical and experimental spectra in this region. All of the above mentioned states, except for the Ar($3p^{-2}[^1D]3d\,^2S$)Ar satellite, are slow-decaying and would contribute to the high-energy peak in the KER spectrum.

4.3 ICD following resonant core excitation of Ar in ArKr: the role of the partner atom

To understand how the energy distributions of the emitted particles in the ICD process depend on the nature of the neighbouring atom, the atomic properties of Kr compared to Ar will be considered first. Krypton is a “softer” atom (see e.g. Ref. [155] for a definition of “soft” and “hard” atoms). As such, it has larger atomic and van der Waals radii (1.89 Å compared to 1.79 Å for Ar [156]), larger polarisability (17.07 a.u. compared to 11.22 a.u. for Ar [157]) and lower ionisation potential (14.00 eV compared to 15.76 eV for Ar [130]), the latter two quantities being inversely proportional [158].

4.3.1 Potential energy curves

Let us now consider how the PECs of the states of interest are influenced by the presence of a “softer” neighbour. The positions of the peaks in the ICD-electron and KER spectra are determined by

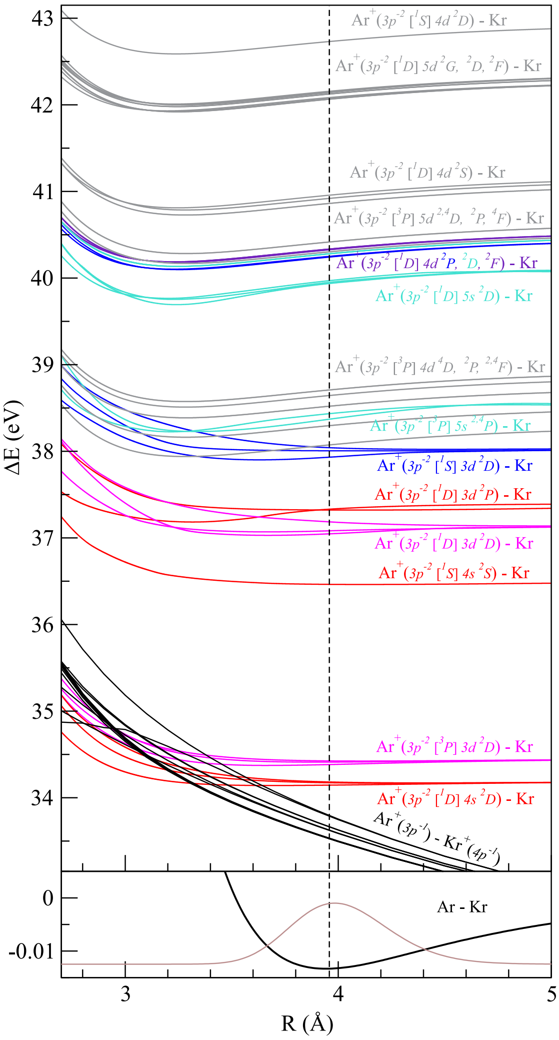

Figure 4.8: Potential energy curves of ArKr; (lower panel) the ground-state PEC and ground-state wave packet density of ArKr; (upper panel) the black curves represent the final repulsive two-site dicationic states $\mathrm{Ar}^+(3p^{-1})\mathrm{Kr}^+(4p^{-1})$; the red and pink curves represent the lowest fast-decaying ionisation satellites, the blue and violet curves represent the higher slow-decaying satellites (see Table 4.2 for the corresponding decay widths). The ICD-active states which were not included in the dynamics calculation, but are populated after the resonant Auger decay are shown in grey.

- the ground-state equilibrium distance R_e,
- the positions of the left turning points of the decaying states PECs,
- the ratios between the characteristic vibrational periods and the ICD lifetimes of the decaying states,
- the shape of the final states PECs. [159]

As a result of the higher polarisability and larger van der Waals radius of Kr, the ground state PEC of ArKr (Fig. 4.8, lower panel) is deeper, $D_e = 13.3\,\mathrm{meV}$, and its minimum is shifted to larger interatomic distances ($R_e = 3.94\,\text{Å}$) compared to the ground state PEC of Ar_2 ($R_e = 3.80\,\text{Å}$).

The PECs of the initial ICD states are presented in the upper panel of Fig. 4.8. Due to the lower ionisation potential of Kr, two more ionisation satellites in ArKr become available for ICD compared to Ar_2, namely, $Ar^+(3p^{-2}[^1D]4s\ ^2D)Kr$ and $Ar^+(3p^{-2}[^3P]3d\ ^2D)Kr$. Thus, the initial ICD states form three groups lying in the energy ranges 34 to 35 eV, 36 to 39 eV, and above 39 eV. The ionisation satellites belonging to a given group are expected to decay by emitting electrons of similar energies and, hence, contribute to the same peak in the total ICD-electron spectrum. Therefore, in the ICD-electron spectrum of ArKr one would expect three peaks, in contrast to the double-peak structure observed in the spectrum of Ar_2. The PECs of the low-lying ionisation satellites ($Ar^+(3p^{-2}[^1D]4s\ ^2D)Kr$, $Ar^+(3p^{-2}[^3P]3d\ ^2D)Kr$, $Ar^+(3p^{-2}[^1S]4s\ ^2S)Kr$, $Ar^+(3p^{-2}[^1D]3d\ ^2D)Kr$, $Ar\ ^+(3p^{-2}[^1D]3d\ ^2P)Kr$, $Ar^+(3p^{-2}[^1S]\ 3d\ ^2D)Kr$) are shallow, with minima located between 3.32 and 5.09 Å and depths in the range between 31 and 217 meV. Their characteristic vibrational periods vary between 290 fs and 2.20 ps. The PECs of the remaining high-lying ICD states have different binding properties. They are deeper, with binding energies between 265 and 334 meV, and their minima are located at shorter internuclear distances 3.20 to 3.34 Å. Their characteristic vibrational periods are between 280 and 290 fs, and generally tend to be shorter than those of the low-lying states. Due to the similar binding properties of the PECs of ArKr and Ar_2, the vibrational periods in ArKr do not significantly differ from the corresponding vibrational periods in Ar_2.

There are 12 two-site dicationic final states of the kind $Ar^+(3p^{-1})Kr^+(4p^{-1})$ (Fig. 4.8, upper panel). Their PECs are repulsive, behaving as R^{-1} at large interatomic distances. Compared to the corresponding PECs of Ar_2, the final states of ArKr are more repulsive at shorter internuclear distances due to the larger van der Waals radius of Kr. However, the difference is negligible and does not affect the positions of the peaks in the spectra.

4.3.2 Decay widths

Let us now focus on the decay widths of the ionisation satellites included in the nuclear dynamics calculation (see Table 4.2). The differences between the decay widths of the states converging to the same ionisation satellites of Ar in ArKr and Ar_2 are of the order of 10%, which is within the error of the computational approach. Therefore, replacing Ar with Kr does not qualitatively change the ICD widths. We can conclude from this and from the above discussion of the vibrational periods that the division into fast- and slow-decaying states made in the case of Ar_2 remains valid also in the case of ArKr. The lowest-lying satellites correlating with $Ar^+(3p^{-2}3d,\ 4s)$Kr (except for the $Ar^+(3p^{-2}[^1S]3d\ ^2D)$Kr state) are fast-decaying. Their decay lifetimes range between 29 and 443 fs, and are by an order of magnitude shorter than the typical vibrational periods (290 fs to 2.20 ps). Consequently, the decay of these states takes place around R_e. The higher-lying ionised-excited states converging to $Ar^+(3p^{-2}\,5s,\ 4d)$Kr fall into the group of the slow-decaying states. Their ICD lifetimes at R_e range between 2.30 and 5.60 ps, and are by an order of magnitude longer than the typical vibrational periods (280 to 290 fs). Thus, the decay of these states is substantially affected by nuclear dynamics and predominantly happens close to the left turning points $R_{t.p.}$ of the corresponding PECs (see Table 4.2 for their positions). A detailed description of the decay as well as the spectra of these two groups of states can be found in Ref. [159].

4.3.3 ICD-electron and KER spectra

Comparison of the ICD-electron spectra of Ar_2 and ArKr originating from the $Ar(2p_{3/2} \rightarrow 4s)$ core excitation

In order to illustrate the influence of the chemically "softer" neighbour on the ICD-electron spectrum, we compare the electron spectra of Ar_2 and ArKr, originating from the same core excitation, $Ar(2p_{3/2} \rightarrow 4s)$ (see Fig. 4.9). The resonant Auger decay of this state proceeds predominantly according to the strict spectator model, leading to the population of the fast-decaying $Ar^+(3p^{-2}4s)$ and $Ar^+(3p^{-2}3d)$ lowest satellites with 89% probability [38]. The remaining 11% of the populated states are the slow-decaying shake-up satellites $Ar^+(3p^{-2}5s)$ (see Table I in Ref. [38]).

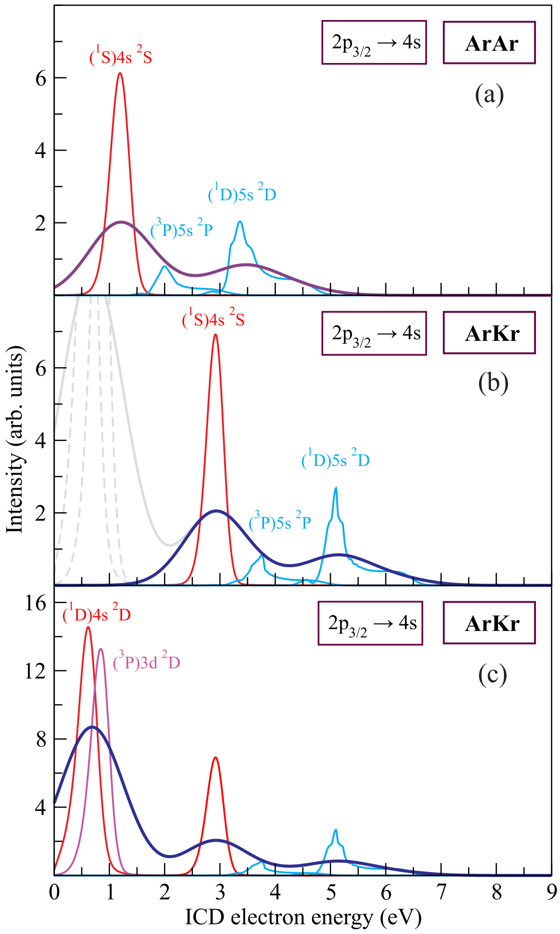

Figure 4.9: Comparison between the ICD-electron spectra following the resonant Auger decay of the Ar($2p_{3/2} \to 4s$) core excitation in Ar_2 and ArKr. (a) Total electron spectrum of Ar_2 evaluated as a sum of the $Ar^+(3p^{-2}[^1S]4s\,^2S)$, $Ar^+(3p^{-2}[^3P]5s\,^2P)$, and $Ar^+(3p^{-2}[^1D]5s\,^2D)$ final resonant Auger states. (b) The portion of the electron spectrum of ArKr (blue curve) originating from the decay of the same Ar^{+*} satellites as in (a). (c) The total ICD-electron spectrum of ArKr including all ICD-available states. All spectra shown in the figure are convolved with a Gaussian of FWHM 1.24 eV to account for the experimental resolution. The colour scheme for the electron spectra originating from the different classes of satellites follows that of Fig. 4.8.

We assume that the states populated in the dimer are the same as in the atom and their branching ratios are preserved as well (see Refs. [46, 159]).

Let us first compare the ICD-electron spectrum of Ar_2 which derives from the decay of the $Ar^+(3p^{-2}[^1S]4s\ ^2S)Ar$, $Ar^+(3p^{-2}[^3P]5s\ ^2P)Ar$, and $Ar^+(3p^{-2}[^1D]5s\ ^2D)Ar$ satellites with the portion of the ICD-electron spectrum of ArKr corresponding to the decay of the same Ar^{+*} states (see Figs. 4.9(a) and (b)). The Ar_2

spectrum possesses two peaks: one between 0.0 and 2.0 eV, attributed to the decay of the $\mathrm{Ar}^+(3p^{-2}[^1S]4s\ ^2S)\mathrm{Ar}$ state, and a second peak between 2.5 and 5.0 eV, originating from the decay of the shake-up $\mathrm{Ar}^+(3p^{-2}5s)\mathrm{Ar}$ states. The corresponding part of the ArKr spectrum (see Fig. 4.9(b)) possesses the same double-peak structure. However, due to the lower ionisation potential of Kr compared to Ar, the energies of the final two-site dicationic states $\mathrm{Ar}^+(3p^{-1})\mathrm{Kr}^+(4p^{-1})$ decrease by the difference between the two ionisation potentials, i.e. by 1.76 eV. Therefore, the respective part of the electron spectrum of ArKr is shifted to larger electron kinetic energies by approximately the same amount (see Fig. 4.9(a) and (b)). As we have discussed above, replacing Ar with Kr in the dimer causes small changes in the PECs and ICD widths of the states relevant for the peaks in question. These changes have in turn a minor effect on the structure of the corresponding portion of the ArKr spectrum, which can be seen by comparing the latter (Fig. 4.9(b)) with the Ar_2 spectrum (Fig. 4.9(a)).

Now let us consider the complete electron spectrum of ArKr (Fig. 4.9(c)). Due to the lower energies of the final two-site dicationic states, two more resonant Auger final states become ICD-active in ArKr: $\mathrm{Ar}^+(3p^{-2}[^1D]4s\ ^2D)\mathrm{Kr}$ and $\mathrm{Ar}^+(3p^{-2}[^3P]3d\ ^2D)\mathrm{Kr}$. These two states are fast-decaying states (see Table 4.2). Consequently, their decay occurs mostly at the equilibrium interatomic distance, producing a third peak at energies between 0.0 and 2.0 eV (see Fig. 4.9(c)). Its intensity is approximately four times higher than that of the second peak, due to the high Auger branching ratios of these two satellites. As a result, the percentage of the final resonant Auger states undergoing ICD which is unusually low in Ar_2 (21%) grows to 67% in the case of ArKr for the $2p_{3/2} \rightarrow 4s$ parent core excitation. The total efficiency of the RA-ICD cascade thus increases by more than three times upon replacing of Ar with Kr as a neighbour.

Theoretical ICD-electron spectra of ArKr

The ICD-electron spectra corresponding to the other two parent core excitations considered in this work, namely $\mathrm{Ar}(2p_{1/2} \rightarrow 4s)$ and $\mathrm{Ar}(2p_{3/2} \rightarrow 3d)$, are presented in Fig. 4.10. All three computed spectra possess three peaks originating from the decay of the three energetically separated groups of satellite states (Fig. 4.8). The lowest-energy peak (0.0 to 2.0 eV) originates from the decay of the $\mathrm{Ar}^+(3p^{-2}[^1D]4s\ ^2D)\mathrm{Kr}$ and $\mathrm{Ar}^+(3p^{-2}[^3P]3d\ ^2D)\mathrm{Kr}$ states, which are not available

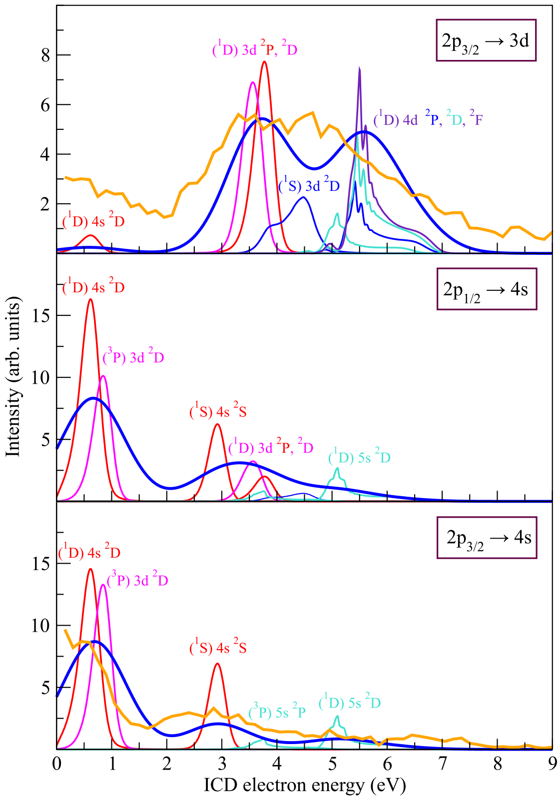

Figure 4.10: ICD-electron spectra obtained in the RA-ICD cascade following Ar($2p_{3/2} \rightarrow 4s$)Kr (lower panel), Ar($2p_{1/2} \rightarrow 4s$)Kr (middle panel), and Ar($2p_{3/2} \rightarrow 3d$)Kr (upper panel) core excitations. The dark blue curves in all panels represent the total ICD spectra corresponding to the particular core excitation. Experimental data is available for the Ar($2p_{3/2} \rightarrow 4s$)Kr and Ar($2p_{3/2} \rightarrow 3d$)Kr excitation (orange curves) [47]. The experimental spectra were scaled such that the intensities of the most intense peaks coincide. The electron spectra resulting from the decay of the individual satellites contributing to the total spectrum of each core excitation are also presented (the color scheme follows that of the PECs in Fig. 4.8).

for ICD in Ar_2 due to the higher ionisation potential of Ar. This peak has a high relative intensity in the spectra corresponding to the Ar($2p_{3/2,1/2} \rightarrow 4s$) parent core excitations, due to the high probability of populating these satellites in the RA decay (46% in the case of the $2p_{3/2} \rightarrow 4s$ excitation and 44% in the case of the $2p_{1/2} \rightarrow 4s$ excitation). In the spectrum corresponding to the $2p_{3/2} \rightarrow 3d$ core excitation this peak is weak, since the population of the respective satellite states is only about 2%. The second peak in all three spectra is located between 2.0 and 4.5 eV. It is produced by ICD of the satellite states in the energy range 36.5 to 39.0 eV (see Fig. 4.8). The third peak is located at energies above 4.5 eV. It is attributed to the ICD of the higher Rydberg states of energies above 39.5 eV (see Fig. 4.8). Its high intensity in the spectrum originating from the Ar($2p_{3/2} \rightarrow 3d$) parent core excitation is a result of strong shake-up processes in the resonant Auger step. The two peaks at higher energy are virtually identical with the respective Ar_2 electron spectra since they originate from ICD of the states correlating with the same Ar satellites in both dimers (see Fig. 4.8, states of energies above 36.0 eV). The peaks in the spectra of ArKr are shifted to higher energies by approximately 1.76 eV relative to the spectra of Ar_2 due to the lower ionisation potential of Kr. The availability of additional ICD-active states in ArKr increases the ICD yield by approximately a factor of 3 in the case of the $2p_{3/2,1/2} \rightarrow 4s$ parent states, whereas the yield in the case of the $2p_{3/2} \rightarrow 3d$ core-excited state remains almost unaltered.

Theoretical KER spectra of ArKr

The computed KER spectra of the three core-excited states are presented in Fig. 4.11. The KER spectra of ArKr are rather similar to those of Ar_2 (see Fig. 5 in Ref. [159]). The two peaks manifest that the decay occurs at two different internuclear separations: the ground state equilibrium distance $R_e = 3.94$ Å and the left turning points of the considered PECs (located between 2.84 and 3.00 Å for the satellites of interest). Thus, all fast-decaying states contribute to the peak at lower energies (2.5 to 4.2 eV), whereas the high-energy peak (4.2 to 6.0 eV) is produced by the slow-decaying states. The corresponding low-energy peaks in the KER spectra of ArKr are shifted to lower kinetic energies by about 200 meV compared to their positions in the Ar_2 spectra. This is due to the larger ground state equilibrium distance of ArKr. The higher peaks in the KER spectra of ArKr are also shifted to lower kinetic energies compared to Ar_2 because the left turning points of the respective PECs are located at larger internuclear distances in the case of ArKr.

Comparison of the theoretical ICD-electron and KER spectra of ArKr with experimental results

The available experimental ICD-electron and KER spectra [47, 49] are shown in Figs. 4.10 and 4.11 as thick orange lines. As one can see from the figures, there is a very good correspondence between the computed and the experimental spectra.

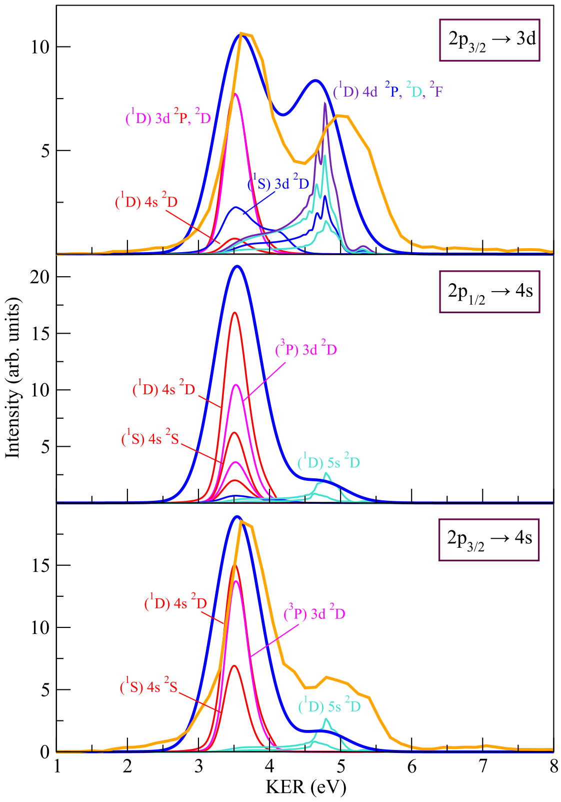

Figure 4.11: KER spectra obtained in the RA-ICD cascade following Ar($2p_{3/2} \to 4s$)Kr (lower panel), Ar($2p_{1/2} \to 4s$)Kr (middle panel), and Ar($2p_{3/2} \to 3d$)Kr (upper panel) core excitations. The spectra are obtained using the mirror image principle. The dark blue curves in all panels represent the KER spectra corresponding to the particular core excitation. The orange lines are the available experimental KER spectra for the Ar($2p_{3/2} \to 4s$)Kr and Ar($2p_{3/2} \to 3d$)Kr core excitation [47, 49]. The experimental spectra were scaled such that the intensities of the lower-energy peaks coincide. The KER spectra of the satellites contributing to the total spectrum of each core excitation are also presented (the color scheme follows that of the PECs in Fig. 4.8).

The calculations reproduce the number of peaks and their relative intensities. The discrepancies concern mainly the positions of the peaks, being larger for the higher-energy peaks which originate from the slow-decaying states. The deviations of the computed ICD-electron and KER spectra from the experimental ones are between 60 and 280 meV, and between 70 and 370 meV, respectively. The errors are comparable with those in the case of Ar_2 and have opposite signs in the ICD-electron and KER spectra due to energy conservation used in the mirror image principle (see Figs. 4.10 and 4.11). The sources of the discrepancies between the theoretical and the experimental spectra are the accuracy of the potential curves (i.e. the values of the equilibrium distance, left turning points, as well as the characteristic vibrational periods) and the decay widths. They are discussed in detail in Ref. [159] for Ar_2, but remain valid also in the case of ArKr.

An additional source of error for this system is the neglect of relativistic effects. The spin-orbit coupling in the final ICD states leads to the splitting of the $Kr^+(4p^{-1}\,{}^2P)$ multiplet into the $Kr^+(4p^{-1}\,{}^2P_{3/2})$ and $Kr^+(4p^{-1}\,{}^2P_{1/2})$ terms which differ by 0.67 eV at asymptotic distances. Moreover, it has been shown [160] that the relativistically corrected ICD rates may differ from the non-relativistic ones. Including the relativistic corrections might shift the position of the theoretical peak by up to a few hundred meV.

Finally, we would like to discuss briefly the effect of omitting some ICD states from the calculations (see Fig. 4.8 for the satellites in question, their PECs are shown in grey). The largest deviation from the experiment should be observed for the ICD spectra of the $2p_{3/2} \to 3d$ parent state where the neglected satellites carry up to 30% of the intensity. The decay of the states below 40 eV would produce electrons with energies between 2.7 and 4.0 eV. The decay of the states in the energy range between 40 and 42 eV is expected to produce electrons of energies between 5.0 and 6.3 eV and thus, enhance the high-energy peak. The highest Rydberg states would decay emitting electrons of energies above 6.5 eV, which would account for the difference between the theoretical and experimental spectra in this region. All of the above mentioned states are slow-decaying and would contribute to the high-energy peak in the KER spectrum.

We would also like to mention that the electronic spectra corresponding to the $2p_{1/2} \to 4s$ and $2p_{3/2} \to 3d$ parent core excitations in ArKr have been previously estimated [32] using a simple model. In this model the PECs of the most populated ICD states were approximated as horizontal lines positioned at the correct asymptotic energies. The final states were represented by repulsive R^{-1} curves. The electron spectra were obtained assuming vertical ICD transitions taking place at the equilibrium distance of the ground state R_e. In this simple model, the low-energy peak originating from the decay of the fast states is accurately described. However, the high-energy peak produced from the decay of the slow ICD states is shifted by about 1 eV to higher kinetic energies. This is due to the fact that the decay of these states is accompanied by nuclear dynamics and it actually occurs in the vicinity of the left turning points of the corresponding PECs. The nuclear motion during the decay also influences the form of the peak. It is now skewed to the large kinetic energies compared to the Gaussian-like peak resulting from the simple model used in Ref. [32]. In addition, due to the assumption that ICD is very fast, according to this model the KER spectrum would consist of a single peak. However, as both the present calculations and the experimental results show, the KER spectrum actually consists of two peaks indicating that the fast and slow decay occur at different internuclear separations.

4.4 Summary and conclusions

This chapter presents the results of *ab initio* computations of ICD-electron and KER spectra produced in the resonant-Auger – ICD cascades following $2p_{3/2} \rightarrow 4s$, $2p_{1/2} \rightarrow 4s$, and $2p_{3/2} \rightarrow 3d$ core excitiations of Ar in Ar_2 and ArKr. We computed the potential energy curves of the ionisation satellites of Ar_2 populated in the resonant Auger steps, the repulsive two-site dicationic final states, as well as the ICD rates. These quantities were used to simulate quantum mechanically the nuclear dynamics during the decay and to derive the ICD spectra.

The computation of the decay rates revealed that the ionisation satellites corresponding to the lowest terms of the respective Rydberg series in both Ar_2 and ArKr have lifetimes considerably shorter than the characteristic vibrational periods of the satellites PECs. In contrast, the lifetimes of the higher Rydberg states are longer than the vibrational periods. Therefore, ICD of the former states is unaffected by nuclear dynamics; it proceeds around the respective equilibrium interatomic distance R_e and the resulting peaks in the spectra retain the shape of the initial vibrational wave packet. However, the dynamics play an important role in the decay of the higher satellites. Due to the larger ICD lifetimes, the decay takes place mostly at interatomic distances close to the left turning points of the corresponding PECs. This shifts the positions of the peaks in the ICD-electron spectra by about 1 eV to smaller energies than would be the case had the decay happened at R_e. The corresponding peaks in the KER spectra are shifted by about 1 eV towards higher energies due to energy conservation. The shapes of the resulting peaks strongly deviate from the shape of the initial vibrational wave packet.

The total ICD spectra of Ar_2 and ArKr exhibit a double-peak and a triple-peak structure, respectively, due to the population of higher Rydberg terms in the shake-up process during the resonant Auger step. The computed spectra deriving from the Ar($2p_{3/2} \rightarrow 4s$) and Ar($2p_{3/2} \rightarrow 3d$) excitations agree well with the available experimental results. The differences in the positions of the calculated and experimentally observed peaks are about a few hundred meV.

The accuracy in the position of the peak originating from the decay of the lower Rydberg states depends on

- the quality of the ground-state vibrational wave packet,
- relative populations of the satellite states in the RA decay,
- the energy difference between the decaying and final states close to the equilibrium distance R_e.

We estimated that the deviation of the theoretical peak from the experimental one due to these factors should amount to 100 – 200 meV. The accuracy in the position of the peak produced in the decay of the higher Rydberg satellites is influenced primarily by

- the accuracy of the positions of the left turning points on the PECs in question,
- the quality of the respective ICD rates.

The left turning points of the majority of states were obtained from model potentials. Moreover, due to the complexity of the task, it is difficult to achieve high accuracy in the computation of *ab initio* interatomic decay widths. Therefore, it is difficult to come up with an error estimate for the case of the higher-lying Rydberg satellites. However, the reasonably small deviation of a few hundred meV from the measured peak shows that our computations were accurate enough.

The total KER spectra of both Ar_2 and ArKr exhibit a double-peak structure. In this case the presence of two peaks indicates that there are two types of decaying states, which decay at two different internuclear separations – the ground-state equilibrium distance R_e and the left turning points of the corresponding PECs. The electron and KER spectra were shown to be the mirror image of each other. Therefore, the shifts of the theoretical peaks compared to the experimental ones are of the same order as those in the ICD-electron spectrum, but have the opposite sign.

Substituting the neighbouring rare-gas atom with a chemically “softer” one has several consequences. Due to the larger van der Waals radius of Kr, the ground state equilibrium distance R_e increases and the positions of the left turning points $R_{t.p.}$ in the PECs of the decaying states shift to larger internuclear separations. The decay of the fast and slow ICD states happens mostly at R_e and $R_{t.p.}$, respectively. Replacing Ar with Kr does not lead to a significant change in either the characteristic vibrational periods of nuclear motion or the ICD lifetimes of the satellite states. Therefore, the same division into fast- and slow-decaying states as in the case of Ar_2 remains valid in ArKr. The larger van der Waals radius of Kr also results in more repulsive character of the final $\mathrm{Ar}^+(3p^{-1})\mathrm{Kr}^+(4p^{-1})$ states at shorter internuclear distances. Moreover, reducing the ionisation potential of the neighbour by replacing Ar with Kr lowers the energies of the final states by approximately 1.76 eV.

We have seen that the ionisation potential of the neighbour has the most pronounced effect on the ICD-electron and KER spectra. On one hand, lowering the final states energies leads to an increase in the energies of the emitted electrons. Comparing the ICD-electron spectra of ArKr and Ar_2, one notices that the peaks originating from the decay of the satellites correlating with the same ionised-excited states of Ar are shifted to higher energies in the case of ArKr. The shift corresponds to the difference between the ionisation potentials of Ar and Kr, namely, 1.76 eV. On the other hand, additional final resonant Auger states may become ICD-active. In the present example these are $\mathrm{Ar}^+(3p^{-2}[^1D]4s\ ^2D)\mathrm{Kr}$ and $\mathrm{Ar}^+(3p^{-2}[^3P]3d\ ^2D)\mathrm{Kr}$. The fast decay of these states produces electrons of kinetic energies between 0 and 2 eV. The increase in the number of available ICD states leads to an overall rise in the ICD yield. The increase is insignificant in the case of the $2p_{3/2} \rightarrow 3d$ core excitation due to the low probability of populating these states (only 2%). However, in the case of the $2p_{3/2,1/2} \rightarrow 4s$ core excitations the efficiency increases more than three times compared to Ar_2.

In the case of the KER spectra, the effect of the neighbour is not as pronounced. Substituting the Ar atom with a softer one has two consequences. First, due to the larger R_e and $R_{t.p.}$ of ArKr compared to Ar_2, the KER spectra of ArKr are shifted to lower kinetic energies. Second, the relative intensity of the lower-energy peak compared to the high-energy one is much larger than in the spectra of Ar_2. This is attributed to the decay of the additional ICD states, which in the case of the $2p_{1/2,3/2} \rightarrow 4s$ core excitations form up to 70% of the available ICD states.

The study of the impact of nuclear dynamics on ICD following resonant Auger gives insight into the mechanism of controlling the energies of the emitted electrons suggested in Ref. [32]. Understanding the origin of the peaks in the spectra and how they are influenced by the presence of different neighbours, can be used to predict the spectra of similar weakly-bound diatomic systems (consisting of identical or different atoms) without explicitly calculating the nuclear dynamics during the decay. This allows for simulation of the spectra in a simple way where only knowledge of the decay rates at the ground state equilibrium distance, and the PECs of the decaying and final states is required. This may also be of importance in larger clusters, since for such systems it becomes computationally impossible to calculate the electron and KER spectra using nuclear dynamics. The ICD-electron spectra are also very sensitive to the nature of the species being ionised in the ICD step. Therefore, we think that this property of the RA-ICD cascade can make it a spectroscopic tool which can be used alongside such well established methods as resonant Auger and near edge X-Ray absorption fine structure (NEXAFS) spectroscopies.

Chapter 5

X-Ray absorption spectra of microsolvated metal cations

In Chapter 4 we studied the RA-ICD cascade in rare-gas dimers. It was assumed that both the resonant core excitation and the subsequent resonant Auger process in dimers proceed analogously to the case of atoms due to the weak interaction between the atoms in the dimer. Recent studies on soft X-Ray absorption (XAS) spectra in ArNe and Ar_2 in the near L-edge region of Ar atom [50] demonstrate that the chemical shifts in the XAS spectra are less than 100 meV in both investigated systems, which evidences the weak influence of a single neighbouring atom. Moreover, the experimental results reported in Ref. [46], confirm that the resonant Auger process in dimers is mostly of local nature.

This approximation is less justified if one considers resonant core excitation and subsequent Auger decay in larger rare-gas clusters and in solids. The XAS spectra of Ar and Ne clusters [41, 42] and Ar solids [40] at the Ne 1s and Ar 2p thresholds as well as the Auger spectra of Ar solids were studied previously. It was found, that for each atomic transition, the XAS spectra of the large clusters exhibit two peaks – from atoms on the surface and in the bulk of the cluster [40–42]. Moreover, the chemical shifts of the peaks in the XAS spectra depend on the size of the clusters and can reach $\sim$1 eV in the case of large clusters and solids [40]. The Auger spectra of Ar solids show that in the case of higher-excited states, the excited electron delocalises over the cluster before the resonant Auger decay takes place, i.e. faster than 6 fs, which is the lifetime of the Ar $2p$ hole [116]. Thus, the delocalisation of the excited electron outpaces the resonant Auger decay and normal Auger takes place instead [40]. Consequently, the environment influences not only the energies of the core-excited states, but also the course of the subsequent de-excitation processes.

The effect of the surrounding becomes even more pronounced in solutions, where the interactions between the initially excited species and the surrounding medium are stronger. For example, studies of the Auger electron spectra of solvated ions demonstrate that the chemical shifts in this case are much larger, of the order of several tens of eV, and that they also depend on the charge of the central ion [16, 17]. Moreover, additional features appear in the spectra, due to the possibility of delocalisation of the final Auger states [16, 17]. Their positions and intensities, as well as the lifetime of the electronic decay process also show a marked dependence on the ionic charge [17].

In this chapter, our intention is to study the X-Ray absorption spectra of metal ions in microsolvated clusters. Understanding whether in a solution, the delocalisation of the core-excited electron is faster than the resonant Auger decay, and whether the competition between the two processes depends on the charge of the metal ion, is an important first step to determining the course of the decay cascade. To this end, we computed and analysed the X-Ray absorption (XAS) spectra of microsolvated clusters of the isoelectronic Na^+ and Mg^{2+} ions with coordination numbers $m = 1 - 6$. In order to better understand the character of the core-excited states and to quantify the degree of delocalisation of the excited electron, we also computed and analysed the singly-occupied natural orbitals (SONO) occupied by the excited electron in the core-excited states of interest.

The chapter will be organised as follows. In the next section, we present the computational details of the geometry optimisation of Na^+ and Mg^{2+} water clusters with coordination numbers from 1 to 6, as well as the computations of the respective XAS spectra. In Sec. 5.2 we present and discuss our results. A summary of our findings and our conclusions are given in Sec. 5.3.

5.1 Computational details

5.1.1 Geometry optimisation

The symmetry point groups of the ground-state structures of the microsolvated clusters of Na^+ and Mg^{2+} were taken from Refs. [161, 162]. In order to obtain the structural parameters, we performed geometry optimisation of the clusters at the DFT level of theory, using the B3LYP functional [163–165] and the 6-

Table 5.1: M-O distances (Å) for the B3LYP/6-311++G(3df,3pd) optimised microsolvated clusters of Na^+ and Mg^{2+}.

$M^{q+}(H_2O)_m$						
$m =$	1	2	3	4	5	6
Na^+	2.212	2.241	2.273	2.308	2.294/2.417/2.420	2.425
Mg^{2+}	1.914	1.936	1.964	2.000	2.041/2.093/2.032	2.100

311++G(3df,3pd) basis set [166]. The calculations were carried out with the Gaussian 09 package [167]. The optimised structures of $M^{q+}(H_2O)_m$ for coordination numbers $m = 1 - 6$ are presented in Fig. 5.1. The symmetries of the equilibrium structures of the metal-water complexes of Na^+ and Mg^{2+} with $m = 1 - 4$ are identical. The 5- and 6-coordinated clusters of both ions have different symmetries (see Fig. 5.1). In the case of Na^+, the 5- and 6-coordinated clusters belong to the C_2 and D_3 point groups, respectively. The corresponding Mg^{2+} structures belong to the C_{2v} and T_h points groups. The 6-coordinated structures used in this work are considered to represent the first solvation shell of both Na^+ and Mg^{2+}. It is known from the literature [168] that Na^+ has between 4 and 8 water molecules in its first coordination shell, whereas the coordination numbers of Mg^{2+} were found to be between 6 and 8. The M-O bond lengths of the optimised microsolvated clusters of the two metal ions are presented in Table 5.1. The computed M-O distances for the 6-coordinated clusters are in very good agreement with the experimental distances reported in Ref. [168], which range between 2.40 and 2.50 Å in the case of Na^+ and between 2.00 and 2.12 Å in the case of Mg^{2+}. The optimised ground-state geometries were used as input for the calculation of the X-Ray absorption spectra (see Sec. 5.1.2).

5.1.2 Core-excitation spectra

Under the assumption of an instantaneous core excitation, during which no significant nuclear dynamics take place, we performed all computations using the ground-state equilibrium structures as input. The X-Ray absorption spectra as well as the excited-state properties were calculated using the CVS-ADC(2)-x method (see Sec. 2.1) as implemented in the Q-Chem package [169–172]. The 6-311++G(3df,3pd) basis set (excluding the f functions) was used on all atoms [166]. The CVS-

ADC(2)-x excitation energies were computed using the cartesian 6D/10F version of the respective basis sets. The symmetry of some of the microsolvated clusters had to be reduced to one of the Abelian subgroups. In the case of the $M^{q+}(H_2O)_{3,4}$ structures, the C_2 point group was used. In the case of the $M^{q+}(H_2O)_6$ structures, the calculations were performed in the C_i (Na^+) and C_{2v} (Mg^{2+}) point groups, respectively. The computed XAS spectra of the microsolvated Na^+ and Mg^{2+} ions for different coordination numbers ($m = 1 - 6$) are shown in Fig. 5.1.

In order to account for the lifetime broadening of the core-excited states, we used the Auger decay widths of Na^+ and Mg^{2+} calculated using the Fano-Stieltjes-ADC method (see Chapter 2) [27, 173]. The basis set used on both ions was the uncontracted cc-pCV5Z basis set [174]. The calculated decay widths are 303 meV in the case of Na^+ and 344 meV in the case of Mg^{2+} [27, 173]. Finally, we convolved each computed transition with a Lorentzian profile of FWHM 303 meV (Na^+) and 344 meV (Mg^{2+}), respectively (see Fig. 5.1).

5.2 Results and discussion

In this section we present the X-Ray absorption spectra of microsolvated clusters of Na^+ and Mg^{2+} with coordination numbers $m = 1-6$ close to the metal K-edge, and discuss the lowest bright states in the spectra correlating with the $1s \to 3p$ and $1s \to 4p$ core excitations in the bare ions. The core-excited states will be characterised by means of their energy, oscillator strength, singly-occupied natural orbitals (SONO) occupied by the excited electron and the projections of the latter on the basis of SONOs of the respective bare ion. Throughout the chapter, we are interested only in the singly-occupied natural orbitals occupied by the excited electron and will refer to them simply as SONO.

Let us denote the SONO of the i-th core-excited state of a given microsolvated cluster as $|\Psi_i\rangle$ and that of the $1s \to nl$ state of the bare ion as $|\chi_{nl}\rangle$. We then define a projection operator $\hat{P}$ on the basis of SONOs of the bare ion as

$$\hat{P} = \sum_{nl} |\chi_{nl}\rangle\langle\chi_{nl}| \tag{5.2.1}$$

In order to find the contribution of core-excited states of the bare ion to the i-th core-excited state of a given cluster, we project the SONO $|\Psi_i\rangle$ onto the

Table 5.2: Excitation energies (eV) and oscillator strengths of the $1s \rightarrow 3p$ core excitations in the bare ions ($m = 0$) and in the metal-water clusters of Na^+ and Mg^{2+} with coordination number $m = 1 - 6$. The overlap between the SONO of each core-excited state of the cluster and the SONO corresponding to the $1s \rightarrow 3p$ excitation of the bare ion, $|a_{i,31}|^2$, is also given.

	Na^+				Mg^{2+}			
m	State	ω_{ex}	f_{osc}	$\lvert a_{i,31}\rvert^2$	State	ω_{ex}	f_{osc}	$\lvert a_{i,31}\rvert^2$
0		1076.18	0.0088	1.00		1310.70	0.0129	1.00
1	$1\,^1B_1$	1075.23	0.0079	0.98	$1\,^1B_1$	1308.94	0.0117	0.97
	$1\,^1B_2$	1075.41	0.0078	0.96	$1\,^1B_2$	1309.25	0.0116	0.94
	$2\,^1A_1$	1076.36	0.0045	0.66	$2\,^1A_1$	1311.49	0.0070	0.53
2	$1\,^1E$	1074.60	0.0069	0.94	$1\,^1E$	1307.78	0.0107	0.92
		1074.60	0.0069			1307.80	0.0107	
	$1\,^1B_2$	1076.15	0.0018	0.42	$1\,^1B_2$	1312.05	0.0032	0.29
3	$1\,^1A_2$	1074.07	0.0061	0.91	$1\,^1A_2$	1306.98	0.0099	0.88
	$1\,^1E$	1075.03	0.0025	0.53	$1\,^1E$	1309.45	0.0056	0.48
		1075.03	0.0025			1309.45	0.0056	
4	$1\,^1E$	1074.21	0.0024	0.52	$1\,^1E$	1308.33	0.0057	0.50
		1074.21	0.0023			1308.35	0.0057	
	$1\,^1B$	1074.27	0.0020	0.47	$1\,^1B$	1308.45	0.0054	0.48
5	$1\,^1B$	1074.34	0.0025	0.53	$2\,^1A_1$	1307.95	0.0053	0.47
	$2\,^1B$	1074.52	0.0022	0.49	$1\,^1B_2$	1308.76	0.0031	0.30
	$2\,^1A$	1074.63	0.0011	0.28	$1\,^1B_1$	1308.81	0.0024	0.23
6	$1\,^1A_u$	1074.19	0.0027	0.57	$1\,^1T_u$	1308.37	0.0016	0.17
	$1\,^1E_u$	1074.56	0.0008	0.23		1308.37	0.0016	
		1074.56	0.0008			1308.37	0.0016	

orthonormal basis of SONOs of the bare ion $\{|\chi_{nl}\rangle\}$

$$\hat{P}|\Psi_i\rangle = \sum_{nl} a_{i,nl}|\chi_{nl}\rangle \tag{5.2.2}$$

where $a_{i,nl}$ denote the overlaps of the SONO of the i-th core-excited state of the microsolvated cluster, and the SONO of the $1s \rightarrow nl$ state of the bare ion. Then, we define the projection P_i as a sum of the squared overlaps between the SONOs of the i-th core-excited state of the cluster, and the SONOs of the $1s \rightarrow nl$ states of the bare ion

$$P_i = \langle \Psi_i | \hat{P} | \Psi_i \rangle = \sum_{nl} |a_{i,nl}|^2 \tag{5.2.3}$$

In Figs. 5.5 and 5.6, we present both the individual contributions $|a_{i,nl}|^2$ and the projection P_i.

5.2.1 Bare ions ($\mathbf{M}^{q+}$)

In order to understand the spectra of the microsolvated clusters, first the XAS spectra of the bare ions have to be discussed.

The XAS spectra of the bare ions are presented in the lowest panels of Fig. 5.1. The only dipole allowed transitions from the K shell in both Na^+ and Mg^{2+} are the $1s \rightarrow np$ transitions, where m is the principal quantum number. Due to the spherical symmetry of the ions, each of these states is triply degenerate. The intensity of the peaks in the series is expected to decrease with increasing principal quantum number [175]. The first bright state in the XAS spectra of both Na^+ and Mg^{2+} is the $1s \rightarrow 3p$ core excitation. The second peak in the XAS spectra, shown in the insets of Fig. 5.1, corresponds to the $1s \rightarrow 4p$ transition. Its intensity is approximately 4 times lower than that of the $1s \rightarrow 3p$ excitation. The oscillator strength of the $1s \rightarrow 3p$ transition in Na^+ is lower compared to Mg^{2+} (see Table 5.2).

The optically forbidden core-excited states are also shown in Fig. 5.1 as points of zero intensity. The first such state in both ions is the lowest excitation $1s \rightarrow 3s$. As can be seen from Fig. 5.1, it acquires small intensity for some of the clusters, due to mixing with optically allowed $1s \rightarrow np$ states. The higher-lying forbidden $1s \rightarrow 4s$ and $1s \rightarrow 3d$ states also lie in the energy range between the first two bright states.

To better understand the effect of the solvent on the electron density distribution in the core-excited states of the metal-water clusters, in Fig. 5.2 we also present the radial density distributions of the excited electron in the bare ions. As can be seen, as a result of the larger charge of Mg^{2+} its orbitals are more compact and consequently, a larger part of the electron density is located within a sphere with radius equal to the metal-oxygen distance, $R_{\mathrm{M-O}}$ (see Table 5.1 and Ref. [168] for the metal-oxygen distances in question). A substantial difference

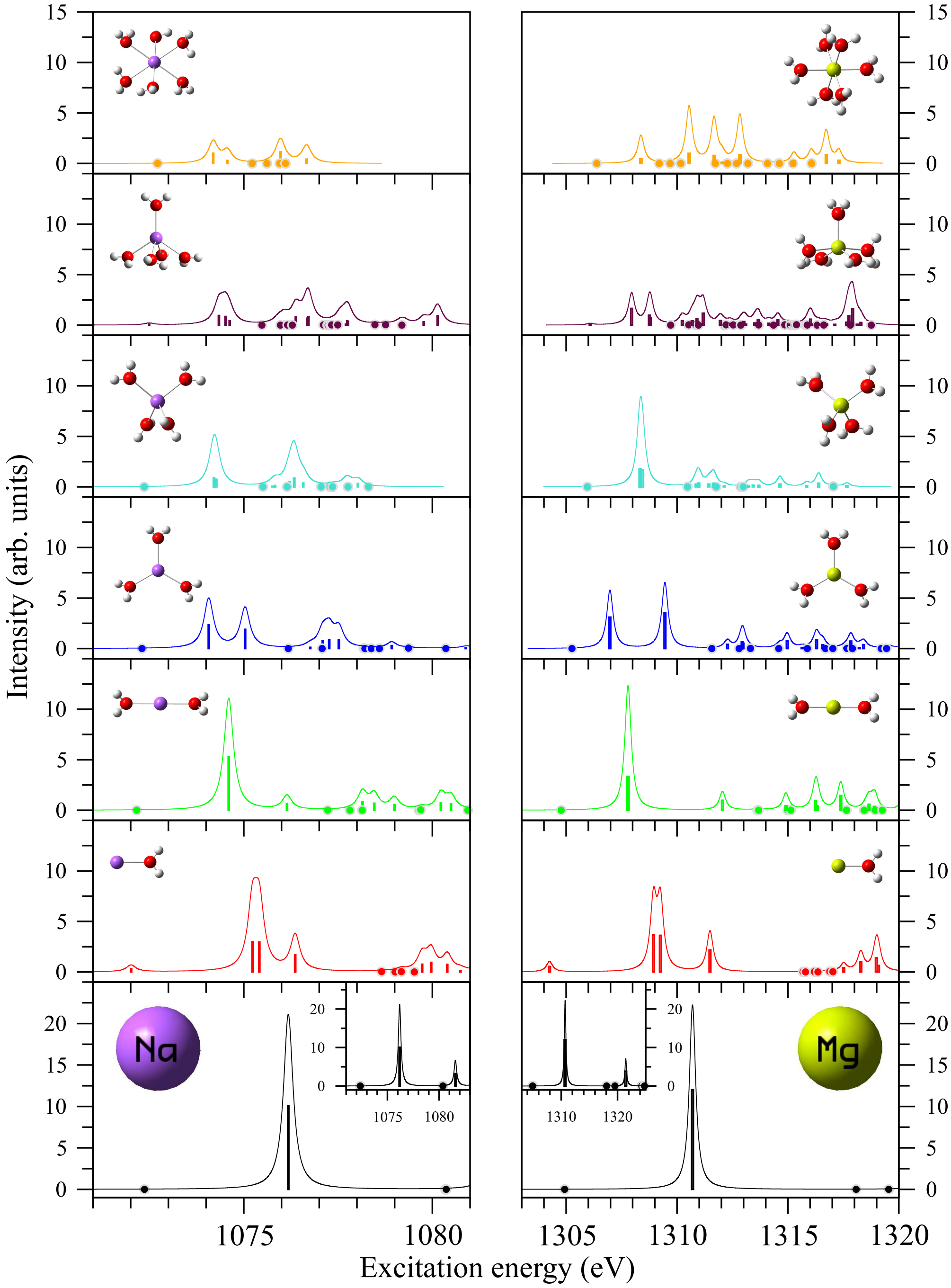

Figure 5.1: X-Ray absorption spectra of Na^+ (left, lowermost panel) and Mg^{2+} (right, lowermost panel), and their microsolvated clusters with coordination numbers $m = 1 - 6$. The $1s \to 4p$ core excitation in the bare ions is shown in the insets of the lowermost panels. The optimised ground-state structures are also presented. The theoretical spectra were convolved with Lorentzians of FWHM 303 meV (Na^+) and 344 meV (Mg^{2+}), respectively, in order to account for the line broadening due to the Auger decay.

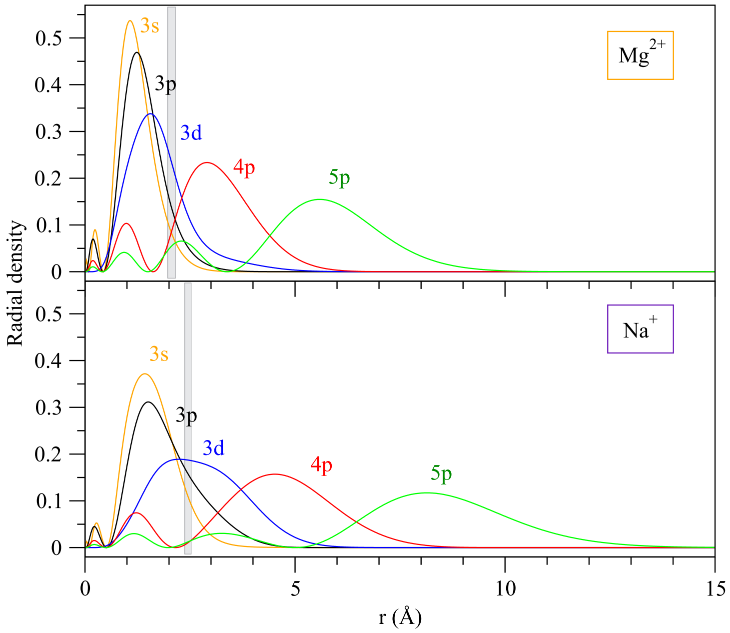

Figure 5.2: Radial density distributions of the SONOs occupied by the excited electron corresponding to the $1s \to 3s$, $1s \to 3p$, $1s \to 3d$, $1s \to 4p$, $1s \to 5p$ core excitations in the bare Na^+ (lower panel) and Mg^{2+} (upper panel) ions. The grey areas represent the range of metal-water distances reported in Ref. [168].

between Na^+ and Mg^{2+} is observed for the electron density distributions of the $3p$ and $3d$ orbitals within the sphere. In the case of the $3p$ orbital, the electron density located within the sphere is 76% for Na^+, in contrast to Mg^{2+}, where it is 91%. The $3d$ orbital of Na^+ is even more spatially extended with only 48% of the electron density within the sphere, in contrast to Mg^{2+}, where most of the electron density, 84%, is still within the sphere.

5.2.2 $M^{q+}(H_2O)$ clusters

We begin the discussion of the core-excited spectra of microsolvated clusters with the singly-coordinated complexes of Na^+ and Mg^{2+}. Their XAS spectra are shown in Fig. 5.1. As one can see, the spectra exhibit a lower-lying peak of large intensity at 1075.33 eV (Na^+) and 1309.09 eV (Mg^{2+}), a second less intense peak at 1076.36 eV (Na^+) and 1311.49 eV (Mg^{2+}), respectively, followed by a series of higher-lying peaks, separated from the first two. The first two peaks can be unambiguously attributed to the $1s \to 3p$ core-excited state, while the higher-energy peaks originate from the $1s \to 4p$ excitation. Let us now discuss the properties of

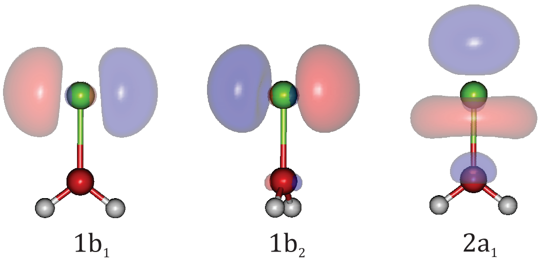

Figure 5.3: SONOs occupied by the excited electron corresponding to the $1s \rightarrow 3p$ core-excited states in $Mg^{2+}(H_2O)$ (C_{2v} symmetry). The orbitals are arranged in increasing energy of the core-excited state (from left to right). They show 50% of the electron density. The respective SONOs of $Na^{+}(H_2O)$ are identical with those of $Mg^{2+}(H_2O)$ and therefore, not shown.

these states.

$1s \rightarrow 3p$ core excitation

The ground-state equilibrium geometries of the singly-coordinated metal-water clusters belong to the C_{2v} symmetry. In this symmetry the degeneracy of the $1s \rightarrow 3p$ core-excited state is completely lifted. The energies of the first two states ($1\,^1B_1$ and $1\,^1B_2$) are lower compared to the energy of the excitation in the respective bare ion, whereas the third state ($2\,^1A_1$) has higher energy compared to the bare ion. The shifts of the $1\,^1B_1$ and $1\,^1B_2$ states are 0.95 and 0.77 eV in Na^+, and 1.76 and 1.45 eV in Mg^{2+}. The $2\,^1A_1$ state is shifted to the blue by 0.18 eV in Na^+ and 0.79 eV in Mg^{2+} (Table 5.2). Note that the oscillator strengths of the $1\,^1B_1$ and $1\,^1B_2$ states are very close to the ones in the bare ions, whereas the oscillator strength of the $2\,^1A_1$ state decreases by about 50% on adding a water molecule.

The energy splitting of the $1s \rightarrow 3p$ multiplet and the observed intensities of the three states can be understood by analysing the SONOs occupied by the excited electron and their overlaps with the SONOs of the bare ions. The SONOs of the $1\,^1B_1$ and $1\,^1B_2$ states (see Fig. 5.3) correspond to the case when the excited electron occupies a $3p$ orbital of the metal ion, which is perpendicular to the M-O bond. Thus, the repulsion between the excited electron and the O-atom is minimal and the electron density distribution closely resembles that of the $1s \rightarrow 3p$ state of the bare ion. This is supported by the fact that the overlap of the SONO corresponding to this state with the SONO of the ionic $1s \rightarrow 3p$ state is close to

1.0 (see Figs. 5.5 and 5.6). As discussed in the previous paragraph, the energies of these states are lower compared to the 1*s* → 3*p* state in the bare ions. Due to the orientation of the *p* orbital which the excited electron occupies, the charge of the metal ion is unscreened. Therefore, the water molecule feels a positive charge, larger than +1 in the case of Na^+ and +2 in the case of Mg^{2+}, which leads to additional stabilisation of the core-excited state relative to the ground state, and consequently to the red shift of the respective excitation energy.

The $2\,^1A_1$ state corresponds to the case when the excited electron occupies a 3*p* orbital of the metal ion oriented towards the O-atom (see Fig. 5.3). Due to the repulsion between the excited electron and the lone pairs of the O-atom, on the one hand, and the shielding of the ionic charge, on the other, the state is destabilised and its energy increases compared to the bare ion. The perturbation introduced by the water molecule leads to a different distribution of the excited electron density from that in the bare ion. The resulting density distribution can no longer be adequately described by the 3*p* orbital, but rather by a combination of SONOs of different states of the bare ion. This is shown in Figs. 5.5 and 5.6, where one can see that the overlap between the SONO corresponding to the $2\,^1A_1$ state in the cluster and the SONO of the 1*s* → 3*p* state of the bare ion is lower than 1.0, and there is a non-negligible overlap with the SONO of the 1*s* → 3*d* state. Since the 1*s* → 3*d* transition is dipole forbidden, the oscillator strength of the $2\,^1A_1$ state decreases. It is ~2.0 smaller than that of the 1*s* → 3*p* state of the bare ion. Note that the $2\,^1A_1$ core-excited state has 66% 1*s* → 3*p* character in the case of Na^+, and 53% in the case of Mg^{2+}. This suggests that the more compact 3*p* orbital of Mg^{2+} is more perturbed than the corresponding more diffuse orbital in Na^+ (see Fig. 5.2).

1*s* → 4*p* core excitation

Let us now consider how the 1*s* → 4*p* excitation is influenced by the presence of a single water molecule. The energies and oscillator strengths of the core-excited states in question are given in Table 5.3. Similarly to the 1*s* → 3*p* excitation, the degeneracy present in the bare ions is lifted and instead of a single peak, several closely lying peaks are observed in the XAS spectra (see Fig. 5.1). However, unlike the 1*s* → 3*p* excitation, the 1*s* → 4*p* state splits into 4 states – $3\,^1B_1$, $3\,^1B_2$, $6\,^1A_1$ and $4\,^1B_1$. In the case of Na^+ these states lie in the range 1079 – 1081 eV, in the

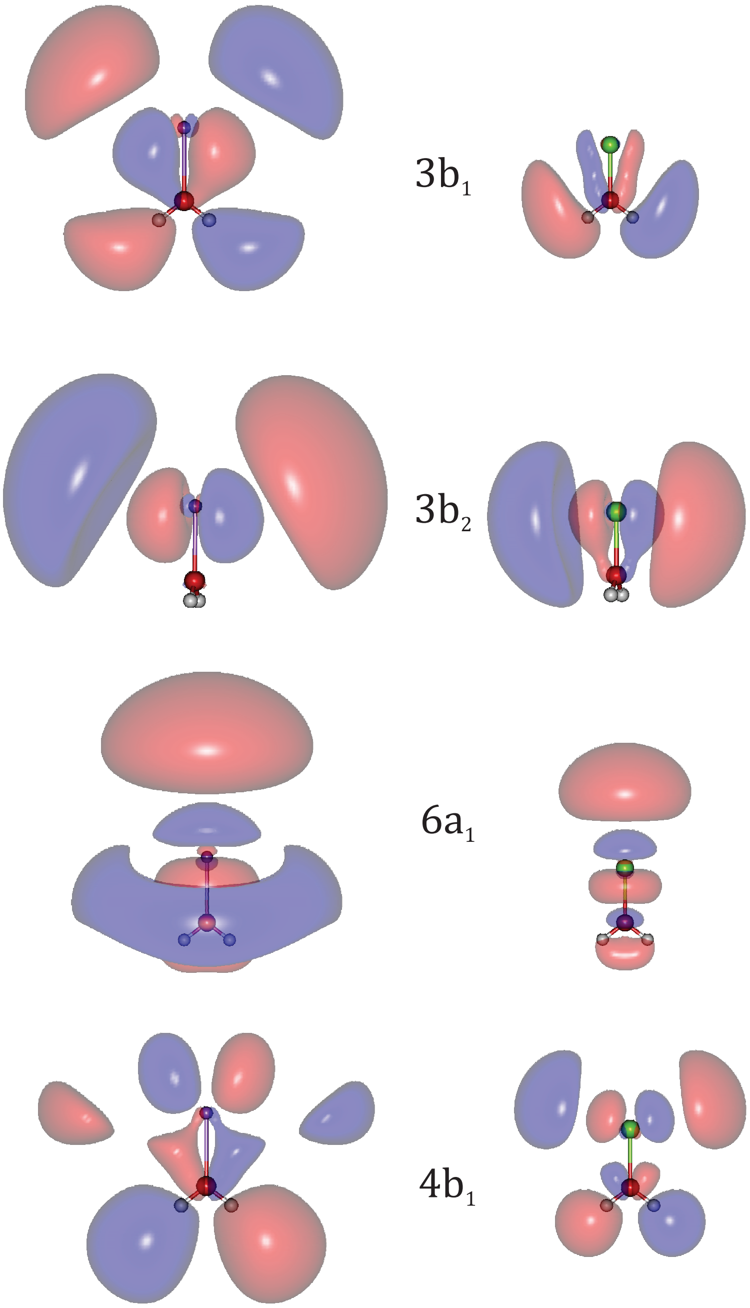

Figure 5.4: SONOs occupied by the excited electron corresponding to the $1s \rightarrow 4p$ core-excited states in $Na^+(H_2O)$ (left) and $Mg^{2+}(H_2O)$ (right) (C_{2v} symmetry) (see Table 5.3 for the energies of the states). The natural orbitals show 50% of the electron density.

Table 5.3: Excitation energies (eV) and oscillator strengths of the $1s \rightarrow 4p$ core excitation in the singly-coordinated clusters of Na^+ and Mg^{2+}. The overlap between the SONO of each core-excited state of the cluster and the SONO corresponding to the $1s \rightarrow 4p$ excitation of the bare ion, $|a_{i,41}|^2$, is also given.

	Na^+			Mg^{2+}		
State	ω_{ex}	f_{osc}	$\|a_{i,41}\|^2$	ω_{ex}	f_{osc}	$\|a_{i,41}\|^2$
$3\,^1B_1$	1079.73	0.0020	0.76	1317.51	0.0014	0.57
$3\,^1B_2$	1079.97	0.0025	0.94	1318.28	0.0033	0.97
$6\,^1A_1$	1080.39	0.0020	0.58	1318.98	0.0045	0.54
$4\,^1B_1$	1080.75	0.0003	0.15	1319.08	0.0031	0.39

case of Mg^{2+} they lie between 1317 and 1320 eV. All of the $1s \rightarrow 4p$ states are shifted to lower excitation energies compared to the bare ions. The shifts amount to 0.83 – 1.85 eV for Na^+ and to 2.39 – 3.96 eV for Mg^{2+}.

The SONOs representing the density distribution of the excited electron in the states deriving from the $1s \rightarrow 4p$ excited state of the bare ion are presented in Fig. 5.4. In analogy with the $1\,^1B_2$ state, the $3\,^1B_2$ state is characterised with the excited electron occupying a p orbital of the metal ion, which is perpendicular to the M-O axis. Thus, the repulsion between the excited electron and the O-atom is minimal. The SONO of the $3\,^1B_2$ state in both systems shows that the electron density is very little affected by the presence of the water molecule. This correlates with the fact that the overlap of the SONO with the $1s \rightarrow 4p$ states in the bare ion is close to 1.0 (see Table 5.3). The $6\,^1A_1$ state is characterised by the excited electron occupying the metal $4p$ orbital oriented towards the O-atom. Due to the repulsion between the excited electron and the lone pairs of O, the electron density is distorted and, therefore, the overlap with the $1s \rightarrow 4p$ states of the bare ion is smaller.

The density distribution of the excited electron in the $3\,^1B_2$ and $6\,^1A_1$ states can be rationalised considering the electrostatic interaction between the excited electron and the ligand. In the case of the state of B_1 symmetry, however, these considerations alone cannot be used to explain the splitting of the state into two states – a lower-lying $3\,^1B_1$ and a higher-lying $4\,^1B_1$ state. The splitting is a result of hybridisation of the p orbital of the metal ion with the $2b_1$ virtual orbital of the water molecule (Fig. 5.4). The sum of the oscillator strengths of the $3\,^1B_1$

and $4\,^1\mathrm{B}_1$ states is close to the oscillator strength of each of the $3\,^1\mathrm{B}_2$ and $6\,^1\mathrm{A}_1$ states. Moreover, the sum of their overlaps with the SONO of the $1s \rightarrow 4p$ state of the bare ion is close to 1.0 (see Table 5.3 and Figs. 5.5 and 5.6). The electron density distribution of the excited electron in the $3\,^1\mathrm{B}_1$ and $4\,^1\mathrm{B}_1$ states in Na^+ and Mg^{2+} is different due to the more diffuse character of the $4p$ orbital of Na^+ (see Fig. 5.2). This results in different degree of hybridisation, which is manifested in the different ratios between the oscillator strengths of $3\,^1\mathrm{B}_1$ and $4\,^1\mathrm{B}_1$ states and between their overlaps with the SONO of the $1s \rightarrow 4p$ ionic state. These ratios imply that the hybridisation is more pronounced in the case of Mg^{2+}.

The addition of a single water molecule has a profoundly different effect on the $1s \rightarrow 3p$ and $1s \rightarrow 4p$ states of the ion. The splitting of the $1s \rightarrow 3p$ multiplet, and the energies and intensities of the resulting states can be rationalised on a purely electrostatic level by considering the ion-dipole interactions between the excited metal ion and the ligands. On the contrary, the splitting of the $1s \rightarrow 4p$ multiplet cannot be explained solely within the framework of ligand-field theory. In the singly-coordinated clusters, this multiplet forms a series of states, in which the metal p-orbital hybridises with virtual orbitals of water. Moreover, the energy of these state decreases compared to the $1s \rightarrow 4p$ core excitation in the bare ion.

5.2.3 $\mathrm{M}^{q+}(\mathrm{H}_2\mathrm{O})_2$ clusters

In this section we will discuss the XAS spectra of the doubly-coordinated metal-water clusters, shown in Fig. 5.1.

$1s \rightarrow 3p$ core excitation

The equilibrium ground-state geometries of the doubly-coordinated metal-water clusters have D_{2d} symmetry (see Fig. 5.1). In this symmetry, the $1s \rightarrow 3p$ core-excited state splits into doubly-degenerate lower-lying states ($1\,^1\mathrm{E}$) and a higher-lying state ($1\,^1\mathrm{B}_2$) (Table 5.2). In the case of Na^+, both the $1\,^1\mathrm{E}$ and the $1\,^1\mathrm{B}_2$ states have lower excitation energies than the ion – the shifts are 1.58 eV and 0.04 eV. In Mg^{2+}, the $1\,^1\mathrm{E}$ states are shifted by 2.92 eV to smaller energies compared to the ion, whereas the excitation energy of the higher-lying $1\,^1\mathrm{B}_2$ state is 1.35 eV larger compared to the ion. The oscillator strengths of the $1\,^1\mathrm{E}$ state in both Na^+ and Mg^{2+} are more than 3 times higher than those of the $1\,^1\mathrm{B}_2$ state.

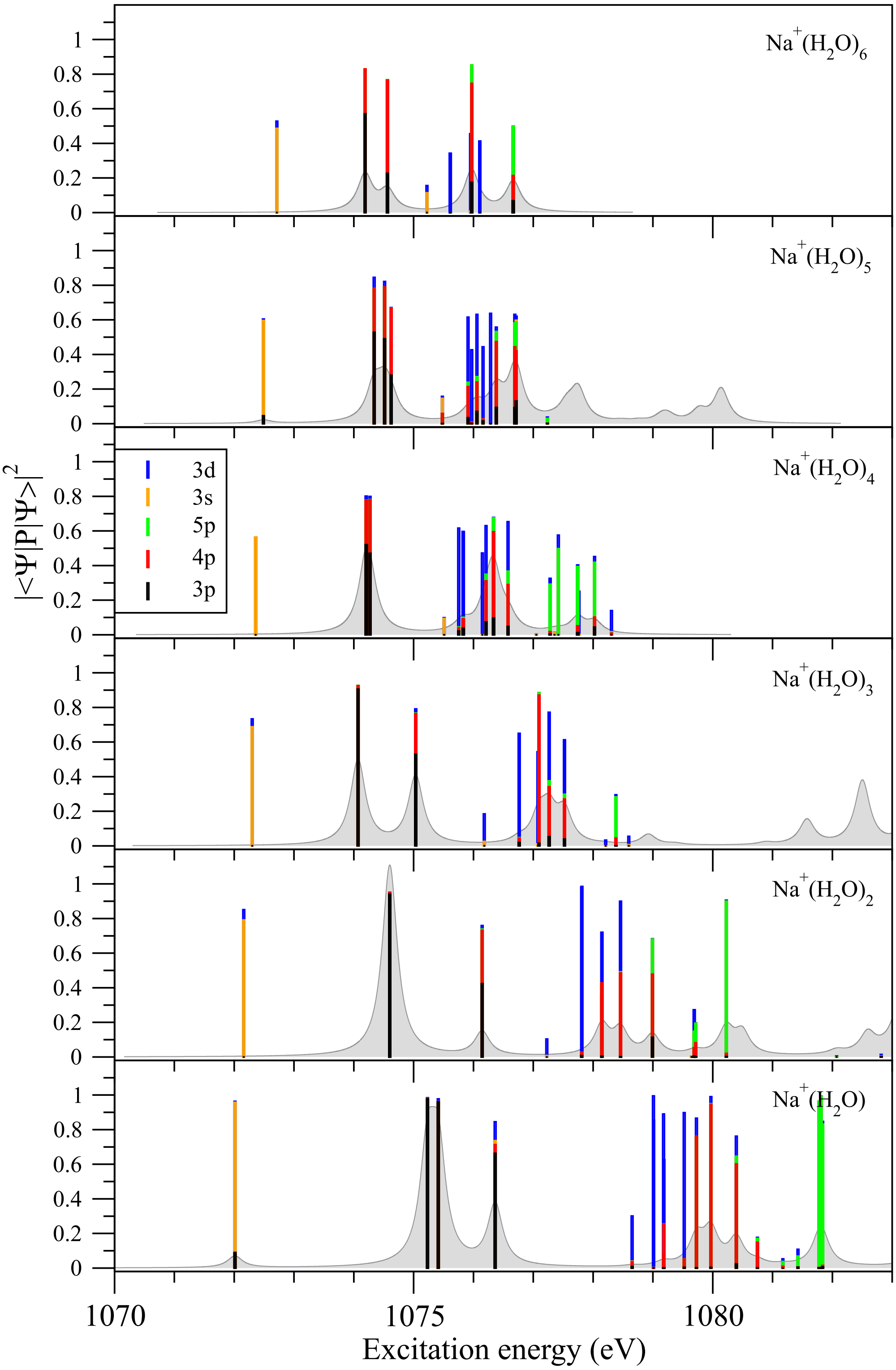

Figure 5.5: Projections of the SONOs corresponding to the core-excited states of the $Na^+(H_2O)_m$ clusters with $m = 1-6$ on the basis of SONOs corresponding to the $1s \rightarrow 3s$, $1s \rightarrow 3p$, $1s \rightarrow 3d$, $1s \rightarrow 4p$ and $1s \rightarrow 5p$ states in Na^+. The color scheme follows that of Fig. 5.2.

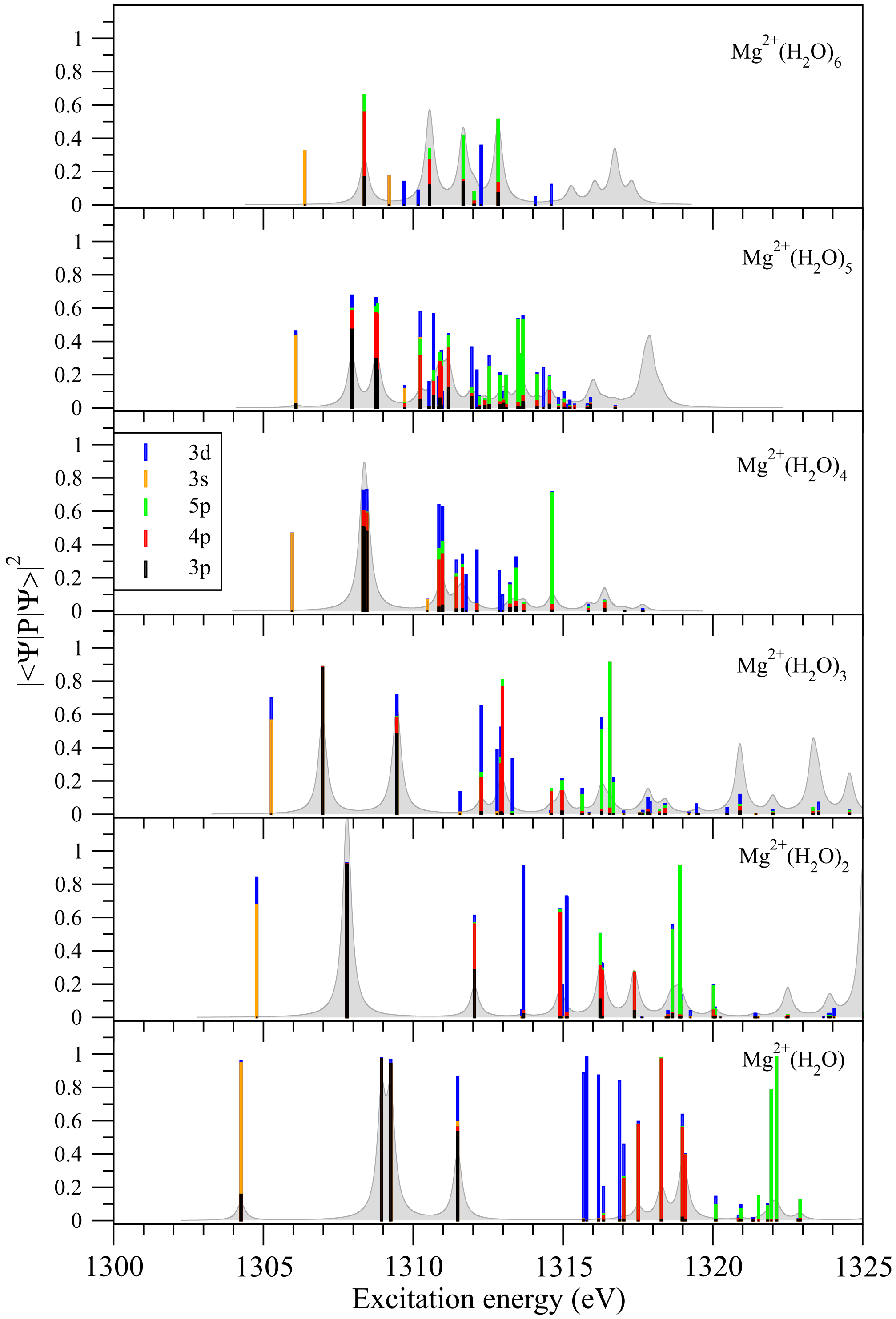

Figure 5.6: Projections of the SONOs corresponding to the core-excited states of the Mg^{2+}(H$_2$O)$_m$ clusters with $m = 1$–6 on the basis of SONOs corresponding to the $1s \rightarrow 3s$, $1s \rightarrow 3p$, $1s \rightarrow 3d$, $1s \rightarrow 4p$ and $1s \rightarrow 5p$ states in Mg^{2+}. The color scheme follows that of Fig. 5.2.

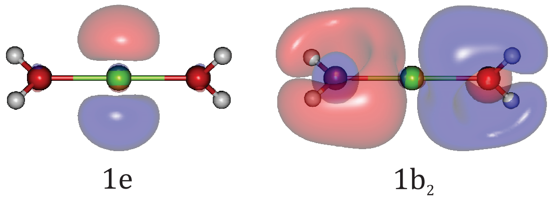

Figure 5.7: SONOs occupied by the excited electron corresponding to the $1s \to 3p$ core excitation in $Mg^{2+}(H_2O)_2$ (D_{2d} symmetry). The orbitals are arranged in increasing energy of the core-excited state (from left to right). They show 50% of the electron density. The respective SONOs of $Na^{+}(H_2O)_2$ are identical with those of $Mg^{2+}(H_2O)_2$ and therefore, not shown.

The energy shifts of the $1\,^1E$ states are about two times higher than the energy shifts of the $1\,^1B_1$ and $1\,^1B_2$ states of the singly-coordinated clusters (see Sec. 5.2.2). This suggests that these energy shifts can be considered as resulting from a pure electrostatic interaction between the unscreened metal ion and the water molecules.

In analogy with the singly-coordinated metal-water clusters, the $1\,^1E$ states correspond to the case when the excited electron occupies a p orbital of the metal ion perpendicular to the O-M-O axis. It can be seen from the SONOs depicted in Fig. 5.7 that the electron density distribution is not perturbed by the presence of the water molecules. This is also confirmed by the values of the overlaps of these states with the $1s \to 3p$ state in the bare ion, which are close to 1.0 for both Na^+ and Mg^{2+} (see Figs. 5.5 and 5.6). The state is stabilised by the additional attractive interaction between the metal ion and the water molecule. Due to the orientation of the metal $3p$ orbital, the water molecules feel an “effective” ionic charge larger than +1 in the case of Na^+, and +2 in the case of Mg^{2+}.

In the $1\,^1B_2$ state, the excited electron occupies a $3p$ orbital of the metal ion, which is oriented towards the water molecules. As a result, the excited electron is wedged up between the two water molecules and experiences strong repulsion, which can be seen from the electron density distribution in Fig. 5.7. Due to the repulsion, the density distribution of the excited electron in the $1\,^1B_2$ state cannot be adequately described only by the SONO of the ionic $1s \to 3p$ state. Consequently, the overlap of the SONO of the $1\,^1B_2$ with the SONO of the $1s \to 3p$ state in the bare ion decreases to 0.42 in the case of Na^+, and only 0.29 in the case of Mg^{2+}. It should be noted that the $1\,^1B_2$ state acquires a non-negligible

$1s \rightarrow 4p$ character. This indicates that as a consequence of the repulsion from the two water molecules, the excited electron density becomes spatially extended. The reduced $1s \rightarrow 3p$ character of the $1\,^1\mathrm{B}_2$ state and the admixture of the $1s \rightarrow 4p$ state leads to a substantial reduction in the intensity (see Fig. 5.1). Similarly to the $2\,^1\mathrm{A}_1$ state in the singly-coordinated clusters, the effect is more pronounced in Mg^{2+} due to its more compact $3p$ orbital.

The $1\,^1\mathrm{B}_2$ state in the doubly-coordinated clusters can serve as an example of the spatial extension of the excited electron, which results from strong repulsion when the p orbital of the metal ion points towards the two water molecules. A similar excited state appears in the 5- and 6-coordinated clusters.

$1s \rightarrow 4p$ core excitation

In the doubly-coordinated metal-water clusters the $1s \rightarrow 4p$ multiplet splits into a series of states as in the singly-coordinated clusters, and the energy of these states decreases further. In the case of Na^+, there are 5 states in the energy range 1078.15 – 1078.99 eV, with 40% to 50% $1s \rightarrow 4p$ character. These states also have a substantial $1s \rightarrow 3d$ contribution, between 30% and 40% (see Fig. 5.5). In the case of Mg^{2+}, the $1s \rightarrow 4p$ excitation splits into 6 states lying between 1314.90 and 1317.38 eV. The first two states have more than 60% $1s \rightarrow 4p$ character, whereas the $1s \rightarrow 4p$ contribution decreases to between 20% and 30% for the remaining states. The splitting of the $1s \rightarrow 4p$ multiplet into a series of states is a result of the hybridisation of the p orbital of the metal ions with virtual orbitals of the ligands. However, this also makes the identification and further analysis of the states very difficult. Already in the doubly-coordinated clusters it becomes clear that these states cannot be considered as being pure $1s \rightarrow 4p$ excitations (see Figs. 5.5 and 5.6). Therefore, we will not discuss the $1s \rightarrow 4p$ core excitation in detail for the larger clusters.

5.2.4 $\mathrm{M}^{q+}(\mathrm{H}_2\mathrm{O})_{3-5}$ clusters

In this section, we will focus on the microsolvated clusters with coordination numbers $m = 3, 4, 5$. The optimised equilibrium structures of the three clusters and the respective XAS spectra are presented in Fig. 5.1.

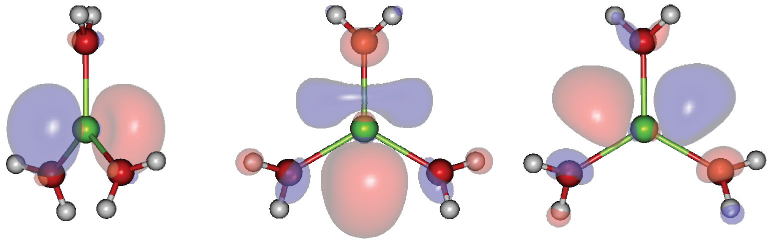

$1a_2$ 1e 1e

Figure 5.8: SONOs occupied by the excited electron corresponding to the $1s \rightarrow 3p$ core excitation in $Mg^{2+}(H_2O)_3$ (D_3 symmetry). The orbitals are arranged in increasing energy of the core-excited state (from left to right). They show 50% of the electron density. The respective SONOs of $Na^+(H_2O)_3$ are identical with those of $Mg^{2+}(H_2O)_3$ and therefore, not shown.

$\mathbf{M^{q+}(H_2O)_3}$

The equilibrium geometries of the triply-coordinated clusters belong to the D_3 symmetry point group. Since the M-O bonds lie in a plane, one can expect that there will be a lower-lying excited state, corresponding to the case when the excited electron occupies a p orbital of the metal ion, perpendicular to the plane, and that this state will have the highest oscillator strength. As can be seen from Figs. 5.1 and 5.8, indeed, this is the case of the lowest excited state, $1\,^1A_2$. It is the first bright state in the XAS spectra, located at 1074.07 eV in Na^+, and 1306.89 eV in Mg^{2+}. In both cases, it is red shifted compared to the $1s \rightarrow 3p$ excitation of the bare ion, and also compared to the lowest excited states of the doubly-coordinated clusters. This stabilisation is again the result of the attractive ion-dipole interaction between the unscreened charge of the metal ion and the three water molecules. The excited electron density is negligibly distorted and consequently, the overlap of this state with the $1s \rightarrow 3p$ state of the bare ion is almost 1.0 (see Figs. 5.5 and 5.6).

The higher-lying states, $1\,^1E$, are doubly-degenerate and correspond to the case when the excited electron occupies a p orbital in the plane of the M-O bonds. They are located at 1075.03 eV in Na^+ and 1309.45 eV in Mg^{2+}, and in both cases are red shifted compared to the bare ion. On the one hand, the states are destabilised by the repulsion between the excited electron and the water molecules, which is confirmed by the electron density distribution (Fig. 5.8) and by their overlap with the $1s \rightarrow 3p$ state of the bare ion (~50% Figs. 5.5 and 5.6). On the

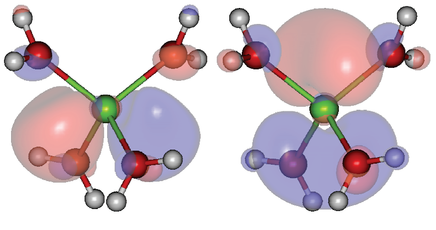

Figure 5.9: SONOs occupied by the excited electron corresponding to the $1s \rightarrow 3p$ core excitation in $Mg^{2+}(H_2O)_4$ (C_2 symmetry). The two SONOs corresponding to the doubly-degenerate $1\,^1E$ states are identical, therefore, only one of them is shown. The orbitals are arranged in increasing energy of the core-excited state (from left to right). They show 50% of the electron density. The respective SONOs of $Na^+(H_2O)_4$ are identical with those of $Mg^{2+}(H_2O)_4$ and therefore, not shown.

other hand, due to the stabilising ion-dipole interaction, the energy of these states is lower than the $2\,^1A_1$ and $1\,^1B_2$ states in the singly- and doubly-coordinated clusters, respectively.

$M^{q+}(H_2O)_4$

The equilibrium structures of the 4-coordinated metal-water clusters belong to the S_4 point group. The geometry of these clusters already implies that the excited electron is strongly repelled by the ligands in all three possible orientations of the p orbital of the metal ion. Therefore, the energy splitting between the first three bright states ($1\,^1E$ and $1\,^1B$) is very small and they form a single peak at 1074.23 eV and 1308.37 eV in the XAS spectra of Na^+ and Mg^{2+}, respectively (see Fig. 5.1 and Table 5.2). Due to the repulsion between the excited electron and the water molecules, the electron density is distorted compared to the regular $3p$ shape in the bare ions (see Fig. 5.9) and the three states have only ~50% $1s \rightarrow 3p$ character (see Figs. 5.5 and 5.6). Moreover, there are large contributions from the $1s \rightarrow 4p$ and $1s \rightarrow 3d$ states of the bare ion, which determine the low oscillator strength of the $1\,^1E$ and $1\,^1B$ states.

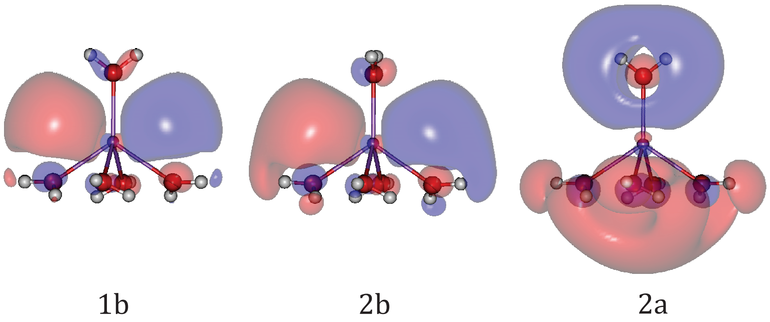

Figure 5.10: SONOs occupied by the excited electron corresponding to the $1s \rightarrow 3p$ core excitation in $Na^+(H_2O)_5$ (C_2 symmetry). The orbitals are arranged in increasing energy of the core-excited state (from left to right). They show 50% of the electron density.

$\mathbf{M^{q+}(H_2O)_5}$

The 5-coordinated metal-water clusters of Na^+ and Mg^{2+} will be discussed separately because they have different equilibrium geometries which result in different XAS spectra.

The equilibrium structure of the 5-coordinated Na^+ cluster has C_2 symmetry and represents a square pyramid. The 4 water molecules in the base of the pyramid form a hydrogen-bonded network [161]. Each of them simultaneously participates in two hydrogen bonds – with O as a donor and with one of the H-atoms as an acceptor. Therefore, it is expected that the excited electron occupying the p orbital of the metal ion on the C_2 axis will be strongly repelled by the water molecules. The corresponding $2\,^1A$ state has the highest energy, the lowest oscillator strength and the smallest overlap with the $1s \rightarrow 3p$ state of the bare ion ($\sim$0.3) (see Table 5.2 and Fig. 5.5). The two lower-lying states, $1\,^1B$ and $2\,^1B$, represent the case, when the excited electron occupies a p orbital perpendicular to the C_2 axis. They have approximately 50% $1s \rightarrow 3p$ character (see Fig. 5.5).

The equilibrium structure of the 5-coordinated Mg^{2+} cluster has C_{2v} symmetry. The water molecules off the C_2 axis do not form hydrogen bonds as in the case of Na^+ and two of them form an almost straight angle (see Fig. 5.1).

The excited state, corresponding to the case when the p orbital of the metal ion is oriented towards these two molecules (Fig. 5.11), $1\,^1B_1$, is highest in energy. Analogously to the $1\,^1B_1$ state in the doubly-coordinated clusters, it has the lowest oscillator strength of the first three bright states and only 23% $1s \rightarrow 3p$ character

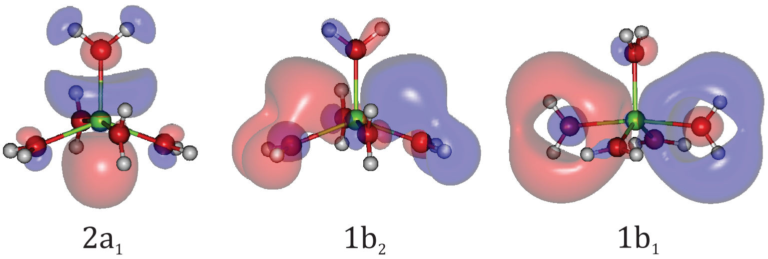

Figure 5.11: SONOs occupied by the excited electron corresponding to the $1s \rightarrow 3p$ core excitation in $Mg^{2+}(H_2O)_5$ (C_{2v} symmetry). The orbitals are arranged in increasing energy of the core-excited state (from left to right). They show 50% of the electron density.

(see Table 5.2 and Fig. 5.6). The two lower-lying states, $2\,^1A_1$ and $1\,^1B_2$, have higher oscillator strengths and a higher contribution of the $1s \rightarrow 3p$ state of the bare ion (50% and 30%, respectively). Due to the energy splitting of ∼0.8 eV between the $2\,^1A_1$ and $1\,^1B_2$ states, two peaks are observed in the XAS spectrum (see Fig. 5.1).

5.2.5 $M^{q+}(H_2O)_6$ clusters

The XAS spectra of the 6-coordinated clusters of Na^+ and Mg^{2+} are presented in the uppermost panel of Fig. 5.1. The two clusters will be discussed separately because of their different equilibrium geometries, which result in different XAS spectra.

$Na^+(H_2O)_6$

The first peak in the XAS spectrum of $Na^+(H_2O)_6$ lying between 1073.50 and 1075.20 eV is comprised of the lower-lying $1\ ^1A_2$ state and a doubly-degenerate higher-lying state ($1\ ^1E$) separated by 0.37 eV (see Table 5.2 and Fig. 5.1). The oscillator strength of the $1\,^1A_2$ is approximately 3 times lower than that of the $1s \rightarrow 3p$ excitation in the bare ion. This state corresponds to the case when the excited electron occupies a p orbital of Na^+ on the C_3 axis (Fig. 5.12). Consequently, the excited electron experiences weak repulsion from the water ligands and the electron density distribution retains the $3p$ orbital shape. This also correlates with the large overlap of the SONO of the $1\,^1A_2$ state with the $1s \rightarrow 3p$ state of the bare ion, 0.57.

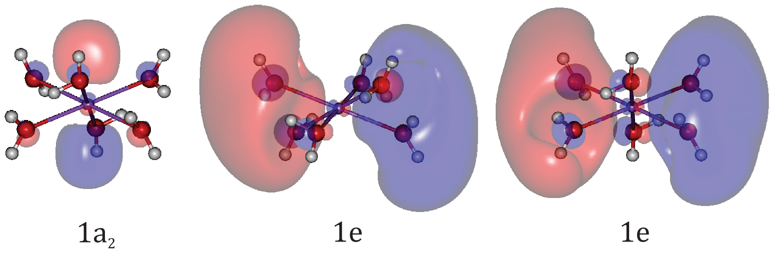

Figure 5.12: SONOs occupied by the excited electron corresponding to the $1s \rightarrow 3p$ core excitation in $Na^+(H_2O)_6$ (D_3 symmetry). The orbitals are arranged in increasing energy of the core-excited state (from left to right). They show 50% of the electron density.

The doubly-degenerate $1\,^1E$ states have only ~10% of the intensity of the bare ion. They correspond to the case when the excited electron occupies the p orbitals, which are perpendicular to the C_3 axis of the cluster. Due to the much stronger repulsion from the water molecules, the electron density is highly distorted and spatially extended. Consequently, the states have only about 20% $1s \rightarrow 3p$ character and more than 50% $1s \rightarrow 4p$ character (see Figs. 5.12 and 5.5).

In the XAS spectrum shown in Fig. 5.1, there are two higher-lying peaks between 1075.50 and 1077.00 eV with intensities comparable to the first peak. They originate from states, which have 10 – 20% contribution from the $1s \rightarrow 3p$ state of the bare ion and also from the higher dipole allowed core excitations. Thus, in the fully coordinated Na^+, the distinction between the $1s \rightarrow 3p$ and the higher-lying $1s \rightarrow np$ core excitations is not straightforward. The states become much closer in energy compared to the bare ion, and as a result, they start interacting. Moreover, due to the delocalised nature of these states, one can discuss their properties after fully taking into account the solvent and the presence of counterions.

$Mg^{2+}(H_2O)_6$

The equilibrium structure of the fully coordinated Mg^{2+} belongs to the T_h symmetry. In this symmetry, the p orbitals of the metal ion are degenerate.

The first four peaks in the XAS spectrum (Fig. 5.1), located between 1308.00 and 1313.50 eV, have less than 70% contribution from states of the bare ion and less than 20% contribution from the $1s \rightarrow 3p$ state (see Fig. 5.6). In this case, the higher $1s \rightarrow 4p$ and $1s \rightarrow 5p$ excitations become lower in energy and start mixing

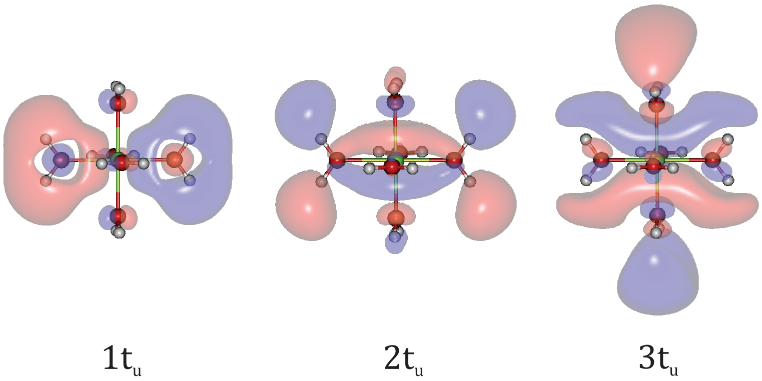

Figure 5.13: SONOs occupied by the excited electron corresponding to the first three bright states in the XAS spectrum of $Mg^{2+}(H_2O)_6$ (T_h symmetry) at energies 1308.37 eV, 1310.55 eV and 1311.67 eV (see Fig. 5.1). The orbitals are arranged in increasing energy of the core-excited state (from left to right). They show 50% of the electron density.

with the $1s \rightarrow 3p$ state. Consequently, all of these excited states lose their atomic character and can no longer be considered as pure $1s \rightarrow 3p$, $1s \rightarrow 4p$ or $1s \rightarrow 5p$ states.

The SONOs of the states forming the first three peaks in the spectrum (lying between 1308.00 and 1312.50 eV), i.e. the $1\,^1\mathrm{T}_u$, $2\,^1\mathrm{T}_u$ and $3\,^1\mathrm{T}_u$ states, are shown in Fig. 5.13. The electron density distribution in the $1\,^1\mathrm{T}_u$ state resembles that of the $1\,^1\mathrm{B}_2$ state of the doubly-coordinated cluster (Fig. 5.7). Since the p orbital of the metal ion occupied by the excited electron points towards the water molecules, the excited electron is strongly repelled. Therefore, its natural orbital is distorted and becomes spatially extended, which can be seen from the non-negligible contributions from higher-lying $1s \rightarrow np$ states to the SONO of this state (Fig. 5.6). In the $2\,^1\mathrm{T}_u$ and $3\,^1\mathrm{T}_u$ states, the p orbital of the metal ion hybridises with virtual orbitals of the surrounding water molecules as in the $3\,^1\mathrm{B}_1$ and $4\,^1\mathrm{B}_1$ states of the singly-coordinated cluster (see Fig. 5.4). As a result, the total projection of the SONO of these two states on SONOs of the bare ion is $<$50%.

Similarly to the fully coordinated Na^+ clusters, the higher $1s \rightarrow np$ excitations become lower in energy and mix with the $1s \rightarrow 3p$ state. Moreover, the total projections of the SONOs occupied by the excited electron on the basis of ionic states are small, which is a result of the spatial extension of the electron density, on the one hand, and the hybridisation with virtual orbitals of the water molecules, on the other. Consequently, in the 6-coordinated ion, it is no longer possible to

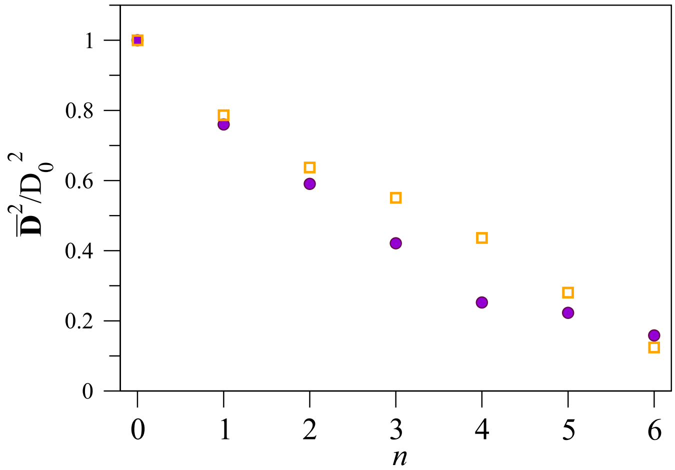

Figure 5.14: Dependence on the coordination number of the relative transition dipole moment of the first three bright states in the XAS spectra of Na^+ (circles) and Mg^{2+} (squares). The relative transition dipole moment was obtained as the ratio between the square of the average transition dipole moment, $\bar{\mathbf{D}}^2$, of the first three bright states correlating with the $1s \rightarrow 3p$ ionic state and the transition dipole moment of the $1s \rightarrow 3p$ core excitation in the bare ion, $\mathbf{D}_0$. As can be seen, the probability of excitation decreases monotonously in both Na^+ and Mg^{2+}.

distinguish between the different $1s \rightarrow np$ excitations.

5.3 Summary and conclusions

In this chapter, we presented and analysed the theoretical X-Ray absorption spectra of microsolvated clusters of the isoelectronic Na^+ and Mg^{2+} at the metal 1s threshold, in order to investigate the degree of delocalisation of the excited electron and how the former depends on the charge of the metal ion. In particular, we focused on the first bright states in the spectra deriving from the $1s \rightarrow 3p$ and $1s \rightarrow 4p$ core excitations in the bare ion.

In the Na^+ and Mg^{2+} clusters with coordination numbers $m = 1-3$, the first three bright states in the XAS spectra can unambiguously be identified as deriving from the $1s \rightarrow 3p$ multiplet of the ion. The energy, intensity and $1s \rightarrow 3p$ character of these states strongly depend on the orientation of the $3p$ orbital of the metal ion. If the excited electron occupies a $3p$ orbital which is perpendicular to the plane of the M-O bonds, the state retains its $1s \rightarrow 3p$ character and it is stabilised by the attraction between the unscreened metal charge and the water molecule(s). This state has the lowest energy and the highest oscillator strength in the multiplet. However, if the $3p$ orbital occupied by the excited electron is oriented towards one or more water molecules, the state loses its $1s \rightarrow 3p$ atomic character and its SONO contains contributions from SONOs of higher-excited states of the bare ion and also shows that the p orbital of the metal ion hybridises with virtual orbitals of the water molecules. The state is destabilised due to the repulsion from the water molecules. The attractive ion-dipole interaction decreases due to screening of the ionic charge.

In the 4- and 5-coordinated clusters, which have a pyramidal arrangement of the solvent molecules, in all three orientations of the metal p orbital the excited electron is surrounded by water molecules. For this reason, all three states correlating with the $1s \rightarrow 3p$ excitation are close in energy and they form a single peak in the XAS spectrum. Due to the repulsion, the three states have no longer purely $1s \rightarrow 3p$ atomic character but rather become a mixture of different states of the bare ion.

In the 6-coordinated clusters, the first three bright states carry only 20% of the intensity of the $1s \rightarrow 3p$ state of the bare ion. In this case, the higher-lying $1s \rightarrow np$ states become lower in energy, which results in mixing of the $1s \rightarrow np$ excitations. Consequently, one can no longer distinguish between the different $1s \rightarrow np$ states.

The effect of the charge of the metal ion comes forward in the bare ions. First of all, due to the smaller ionic radius of Mg^{2+} compared to Na^{+} [176], the M-O distance in the first solvation shell is smaller in the case of Mg^{2+}. Moreover, the SONO occupied by the excited electron in the $1s \rightarrow 3p$ state is more compact in the case of Mg^{2+}, compared to Na^{+}. This implies that the repulsion between the excited electron and the O lone pairs is larger in Mg^{2+}, and for the small clusters ($m = 1 - 3$), the core-excitations of Mg^{2+} are more strongly perturbed by the presence of the ligands. However, in the larger clusters, we could not distinguish the effect of the ionic charge neither on the XAS spectra nor on the delocalisation phenomenon.

In conclusion, we observe that both the electrostatic field created by the ligands, and the hybridisation of the p orbital of the metal ion with virtual orbitals of the water molecules result in spatially more extended distribution of the excited electron in the cluster compared to the bare ion. Based on this observation alone, one cannot draw a conclusion whether the delocalisation and subsequent solvation of the excited electron occur within the lifetime of the core hole. However, one can expect that the resonant Auger process will proceed differently in the solvated ion due to the difference between the core-excited states of the solvated and the bare ions.

An additional interesting question is whether in a larger cluster the electron distribution will become even more spatially extended. In order to clarify this, additional computations including a second and higher solvation shells as well as counterions are needed.

Appendices

Appendix A

Rydberg states of cations

A.1 General formalism

A Rydberg state of an atom or a molecule is an excited state, in which the mean distance of the excited electron from the positively charged ionic core is so large that the structure of the ionic core can be neglected and the electron can be considered as moving in a potential created by a point charge. Therefore, the motion of the electron is the same as it would be in a hydrogen atom (as implied by Eq. (A.1.1)). [177] The energy of the Rydberg state, E_m^{ne}, is equal to

$$E_m^{ne} = \mathrm{IP}_m - \frac{R}{(n-\delta)^2} \tag{A.1.1}$$

Here, IP_m is the ionization potential towards which the Rydberg series converges as n goes to infinity; R is the Rydberg constant ($R = 13.61\,\mathrm{eV}$); δ is called the quantum defect [178], which is defined as the deviation of the core charge from an impenetrable point charge (a detailed explanation of the dependence of δ on the type of Rydberg orbital for both atoms and molecules is given in Ref. [178]). The Rydberg series as defined in Eq. (A.1.1) is valid for sufficiently high excitations (with a large value of the principal quantum number n).

Due to the spatially extended nature of Rydberg orbitals compared to valence orbitals, the theoretical description of Rydberg states requires basis sets including diffuse functions (such basis sets provide a correct description only of the lowest members of a Rydberg series) or specifically designed basis sets (such as those of the Kaufmann-Baumeister-Jungen-type [147]). Consequently, if one is interested in higher-lying Rydberg states, one needs to use large augmented basis sets, on the one hand, and compute multiple roots of the electronic Hamiltonian, on the other hand. In addition to the need of using iterative diagonalisation techniques for huge matrices (e.g. in the case of ArHe dimer, the size of the CISD(T) matrix is $\sim 5 \cdot 10^6$ for a basis set containing 100 basis functions [179]), the convergence to the desired roots of the electronic Hamiltonian is also problematic. And yet if the diagonalisation step is feasible, the high density of states in the energy range of interest can turn out to be a stumbling block in the identification of the desired Rydberg states. Therefore, within the standard quantum-chemical methods, the computation of high-lying Rydberg states even in small systems, such as diatomics, becomes a very difficult task. This calls for the development of alternative methods, specifically designed for this purpose.

In the following we present a method, which utilises the above mentioned properties of the Rydberg states to construct an approximate wave function describing the Rydberg satellites of cations [77]. The wave function of a Rydberg satellite, e.g. $|\Psi_{em}^{N-1}\rangle$, is written as an anti-symmetrised product of two wave functions describing the ionic fragment (dication in this case) $|\Psi_m^{N-2}\rangle$ and the excited electron $|\phi_e\rangle$ represented by the creation operator $c_e^\dagger$

$$|\Psi_{em}^{N-1}\rangle = c_e^\dagger|\Psi_m^{N-2}\rangle \tag{A.1.2}$$

Each of the two wave functions $|\phi_e\rangle$ and $|\Psi_m^{N-2}\rangle$ can be constructed as a normalised linear combination of properly chosen states. The wave function of the Rydberg electron is represented as a linear combination of virtual Hartree-Fock orbitals of the N-particle system

$$|\phi_e\rangle = \sum_a f_a|\phi_a\rangle \tag{A.1.3}$$

where the coefficients f_a (strictly speaking, they should be denoted as f_{ea}) in the linear expansion are variational parameters. Similarly, the wave function of the dicationic core is represented as a linear combination of dicationic states generated, for example, using the ADC method

$$|\Psi_m^{N-2}\rangle = \sum_I a_{mI}|\tilde{\Psi}_I^{N-2}\rangle \tag{A.1.4}$$

where $\{|\tilde{\Psi}_I^{N-2}\rangle\}$ are a set of ADC states corresponding to the particular dicationic configuration, and a_{mI} are variational parameters, determining the weight of a particular ADC state $|\tilde{\Psi}_I^{N-2}\rangle$ in $|\Psi_m^{N-2}\rangle$. The two wave functions corresponding to the molecular ion $|\Psi_m^{N-2}\rangle$ and the excited electron $|\phi_e\rangle$ are constrained to be orthogonal

$$c_e|\Psi_m^{N-2}\rangle = 0 \tag{A.1.5}$$

Using the trial wave function Eq. (A.1.2) and the corresponding expansions Eqs. (A.1.3) and (A.1.4), the expectation value of the Hamiltonian with respect to the trial function $|\Psi_{em}^{N-1}\rangle$ can be constructed. The usual partitioning of the Hamiltonian into a one-electron $\hat{H}_0 + \hat{W}$ and a two-electron $\hat{V}$ part is used

$$\hat{H} = \hat{H}_0 + \hat{W} + \hat{V} \tag{A.1.6}$$

$$= \sum_p \epsilon_p c_p^\dagger c_p + \sum_{pq} w_{pq} c_p^\dagger c_q + \frac{1}{2} \sum_{pqrs} V_{pqrs} c_p^\dagger c_q^\dagger c_s c_r \tag{A.1.7}$$

where ϵ_p denote the Hartree-Fock one-electron energies, V_{pqrs} denote the two-electron integrals in the basis of Hartree-Fock orbitals. The quantities w_{pq}, constituting the non-diagonal one-electron part, are expressed in terms of two-electron integrals

$$w_{pq} = -\sum_r V_{pr[qr]} n_r$$

where n_r is the occupation number of the r-th orbital. Using the above notations, the matrix elements of the one-electron part $\hat{H}_0 + \hat{W}$ with respect to the Hartree-Fock one-particle states can be re-written as

$$h_{pq} = \epsilon_p \delta_{pq} - \sum_r V_{pr[qr]} n_r \tag{A.1.8}$$

The wave function Eq. (A.1.2) in a second-quantised form reads

$$|\Psi_{em}^{N-1}\rangle = c_e^\dagger |\Psi_m^{N-2}\rangle = c_e^\dagger \sum_I a_{mI} |\tilde{\Psi}_I^{N-2}\rangle \tag{A.1.9}$$

For further use let us evaluate the commutator of c_e and the Hamiltonian $\hat{H}$

$$[c_e, \hat{H}] = \sum_p h_{eq} c_q + \frac{1}{2} \sum_{qrs} V_{eq[rs]} c_q^\dagger c_s c_r \tag{A.1.10}$$

Finally, using the form of the wave function (A.1.9), the expectation value of the Hamiltonian can be written as

$$\begin{aligned} E[\Psi_{em}^{N-1}] &= \langle \Psi_{em}^{N-1} | \hat{H} | \Psi_{em}^{N-1} \rangle \\ &= \langle \Psi_m^{N-2} | c_e \hat{H} c_e^\dagger | \Psi_m^{N-2} \rangle \end{aligned} \tag{A.1.11}$$

Using the commutation relation Eq. (A.1.10) in Eq. (A.1.11), one obtains the following expression

$$\begin{aligned} E[\Psi_{em}^{N-1}] = \langle \Psi_m^{N-2} | \hat{H} | \Psi_m^{N-2} \rangle &+ \sum_j h_{eq} \langle \Psi_m^{N-2} | c_q c_e^\dagger | \Psi_m^{N-2} \rangle \\ &+ \tfrac{1}{2} \sum_{qrs} V_{eq[rs]} \langle \Psi_m^{N-2} | c_q^\dagger c_s c_r c_e^\dagger | \Psi_m^{N-2} \rangle \end{aligned} \tag{A.1.12}$$

Using the anticommutation relations for the creation and annihilation operators, the expansion (A.1.3) and the orthogonality condition Eq. (A.1.5), one arrives at the expression

$$E[\Psi_{em}^{N-1}] = \langle\Psi_m^{N-2}|\hat{H}|\Psi_m^{N-2}\rangle + h_{ee} + \sum_{qs} V_{eq[es]}\langle\Psi_m^{N-2}|c_q^{\dagger}c_s|\Psi_m^{N-2}\rangle \tag{A.1.13}$$

which can be considered as a sum of the energy of the dicationic core, the energy of the excited electron and the energy of their interaction. The next step is to minimise the energy of the Rydberg state Eq. (A.1.13) by varying the expansion coefficients $\{a_{mI}\}$ and $\{f_a\}$ simultaneously until self-consistency is reached. For this purpose, a Lagrangian is constructed employing the conditions of normalisation of $|\phi_e\rangle$ and $|\Psi_m^{N-2}\rangle$

$$\mathcal{L} = \langle\Psi_{me}^{N-1}|\hat{H}|\Psi_{me}^{N-1}\rangle + \lambda(1 - \langle\phi_e|\phi_e\rangle) + \mu(1 - \langle\Psi_m^{N-2}|\Psi_m^{N-2}\rangle) \tag{A.1.14}$$

The Lagrangian is minimised with respect to the two sets of coefficients

$$\frac{\partial\mathcal{L}}{\partial\mathbf{f}} = \mathbf{0} \tag{A.1.15}$$

$$\frac{\partial\mathcal{L}}{\partial\mathbf{a}} = \mathbf{0} \tag{A.1.16}$$

resulting in the following sets of equations

$$\begin{multline}\sum_b f_b\left(h_{ab} + \sum_{pq} V_{ap[bq]}\langle\Psi_m^{N-2}|c_p^{\dagger}c_q|\Psi_m^{N-2}\rangle + \delta_{ab}\langle\Psi_m^{N-2}|\hat{H}|\Psi_m^{N-2}\rangle\right) \\ - \lambda\sum_b f_b\delta_{ab} = 0 \tag{A.1.17}\end{multline}$$

$$\begin{multline}\sum_J a_{mJ}\left(h_{ee}\delta_{IJ} + \sum_{pq} V_{ep[eq]}\langle\tilde{\Psi}_I^{N-2}|c_p^{\dagger}c_q|\tilde{\Psi}_J^{N-2}\rangle + \langle\tilde{\Psi}_I^{N-2}|\hat{H}|\tilde{\Psi}_J^{N-2}\rangle\right) \\ - \mu\sum_J a_{mJ}\delta_{IJ} = 0 \tag{A.1.18}\end{multline}$$

which are interdependent and therefore, have to be solved iteratively. The procedure is similar to the SCF procedure. It requires an initial guess of the expansion coefficients. The selection of these coefficients is based on knowledge about the character of the Rydberg state. The optimal expansion coefficients are determined by solving Eqs. (A.1.17) and (A.1.18) iteratively. The physical picture behind Eqs. (A.1.17) and (A.1.18) is that the electron polarises the dicationic core. As a result of this interaction, configuration mixing can be observed in the dication. This means that the latter is no longer represented by a single configuration, but is rather a mixture of several dicationic configurations. The new cationic state then acts as a modified potential for the Rydberg electron which is accounted for by Eq. (A.1.17). The strength of the configuration mixing is sensitive to the nature of the excited electron [179].

The iterative procedure requires a reformulation of Eqs. (A.1.17) and (A.1.18) in terms of quantities, which can be obtained from a preceding ADC calculation. Let us consider the quantities

$$\sum_{pq} V_{ap[bq]} \langle \tilde{\Psi}_I^{N-2} | c_p^\dagger c_q | \tilde{\Psi}_J^{N-2} \rangle \tag{A.1.19}$$

They can be regarded as a representation of the one-particle operator

$$\hat{V}^{ab} = \sum_{pq} V_{ap[bq]} c_p^\dagger c_q \tag{A.1.20}$$

in the basis of ADC states. These matrix elements can easily be obtained within the ADC/ISR approach by considering

$$\hat{V}^{ab} = \sum_{pq} V_{pq}^{ab} c_p^\dagger c_q$$

as a one-particle operator with matrix elements $(V^{ab})_{pq} = V_{ap[bq]}$ in the basis of one-particle HF states. Inspecting the remaining terms in Eqs. (A.1.17) and (A.1.18), one notices that the elements $\langle \tilde{\Psi}_I^{N-2} | \hat{H} | \tilde{\Psi}_J^{N-2} \rangle$ are merely the ADC matrix elements $(\mathbf{H})_{IJ}$, and $\langle \Psi_m^{N-2} | \hat{H} | \Psi_m^{N-2} \rangle$ can easily be obtained from them.

Using the notations introduced in the previous paragraph, one can re-write Eq. (A.1.17) as

$$\sum_b \left[h_{ab} + \sum_{IJ} a_{mI}^* a_{mJ} \left(\langle \tilde{\Psi}_I^{N-2} | \hat{V}^{ab} | \tilde{\Psi}_J^{N-2} \rangle + \delta_{ab} \langle \tilde{\Psi}_I^{N-2} | \hat{H} | \tilde{\Psi}_J^{N-2} \rangle \right) - \lambda \delta_{ab} \right] f_b = 0 \tag{A.1.21}$$

or in matrix form

$$(\mathbf{h} + \tilde{\mathbf{V}}_m + E_m \mathbf{1} - \lambda \mathbf{1}) \mathbf{f} = \mathbf{0} \tag{A.1.22}$$

The matrix elements of $\mathbf{h}$ can be evaluated according to Eq. (A.1.8). This is the representation of the one-electron part of the Hamiltonian in the set of virtual Hartree-Fock orbitals chosen for the expansion of the wave function of the Rydberg electron. The matrix element $(\tilde{\mathbf{V}}_m)_{ab}$ is obtained as the expectation value of the operator $\hat{V}^{ab}$ with respect to the wave function of the dicationic core

$$(\tilde{\mathbf{V}}_m)_{ab} = \langle \Psi_m^{N-2} | \hat{V}^{ab} | \Psi_m^{N-2} \rangle \tag{A.1.23}$$

as explained above. The third term in Eq. (A.1.22), E_m, is the expectation value of the Hamiltonian with respect to the wave function of the dicationic core

$$E_m = \mathbf{a}_m^\dagger \mathbf{H} \mathbf{a}_m = \langle \Psi_m^{N-2} | \hat{H} | \Psi_m^{N-2} \rangle$$

The second set of equations (A.1.18) for the coefficients $\{a_{mJ}\}$ can be reformulated as follows:

$$\begin{aligned} \sum_J a_{mJ} \Bigg(h_{ee}\delta_{IJ} + \sum_{ab} f_a^* f_b \sum_{pq} V_{ap[bq]} \langle \tilde{\Psi}_I^{N-2} | c_p^\dagger c_q | \tilde{\Psi}_J^{N-2} \rangle \\ + \langle \tilde{\Psi}_I^{N-2} | \hat{H} | \tilde{\Psi}_J^{N-2} \rangle \Bigg) - \mu \sum_J a_{mJ} \delta_{IJ} = 0 \end{aligned} \tag{A.1.24}$$

or in matrix form

$$(\mathbf{H} + \tilde{\mathbf{V}}_e + h_{ee}\mathbf{1} - \mu\mathbf{1})\mathbf{a} = \mathbf{0} \tag{A.1.25}$$

Here $\tilde{\mathbf{V}}_e$ is a matrix, whose elements are obtained from the matrix representation of $\hat{V}^{ee}$ in the basis of dicationic ADC states

$$(\tilde{\mathbf{V}}_e)_{IJ} = \langle \tilde{\Psi}_I^{N-2} | \hat{V}^{ee} | \tilde{\Psi}_J^{N-2} \rangle \tag{A.1.26}$$

The operator $\hat{V}^{ee}$, on its turn, is obtained from the operator $\hat{V}^{ab}$ as follows

$$\hat{V}^{ee} = \sum_{ab} f_a^* f_b \hat{V}^{ab}$$

The quantity h_{ee} in Eq. (A.1.25) is the expectation value of the one-electron part of the Hamiltonian with respect to the wave function of the Rydberg electron

$$h_{ee} = \langle \phi_e | \hat{h} | \phi_e \rangle$$

It is the energy of the Rydberg electron.

Note: An important note should be made on the difference between the matrices $\tilde{\mathbf{V}}_m$ and $\tilde{\mathbf{V}}_e$. Both of them are obtained from the quantities in Eq. (A.1.19). In the first case, the size of the matrix $\tilde{\mathbf{V}}_m$ is equal to the number of one-particle states, constituting the vector $|\phi_e\rangle$. Each element of $\tilde{\mathbf{V}}_m$ represents the expectation value of the operator $\hat{V}^{ab}$ with respect to $|\Psi_m^{N-2}\rangle$ (see Eq. (A.1.23)). In the second case, the size of the matrix is equal to the number of ADC states used in the expansion of $|\Psi_m^{N-2}\rangle$. The matrix is the representation of the operator $\hat{V}^{ee}$ in the basis of ADC states $\{|\tilde{\Psi}_I^{N-2}\rangle\}$ used in the expansion of $|\Psi_m^{N-2}\rangle$.

Finally, Eqs. (A.1.22) and (A.1.25) are solved iteratively in order to determine the two sets of coefficients $\{f_a\}$ and $\{a_{mJ}\}$ which minimise the energy functional (A.1.11). The energy of the Rydberg state of interest is then obtained from Eq. (A.1.11) using the optimal expansion coefficients.

A.2 Spin-adapted configurations

In order to construct spin-adapted linear configurations for the wave function of the Rydberg state $|\Psi_{em}^{N-1}\rangle$, it is useful to adopt the spin-adapted dicationic configurations in the current ADC(2) implementation [68]. The explicit formulas for these functions can be found in Ref. [180]. The dicationic ADC states $|\tilde{\Psi}_I^{N-2}\rangle$ can be of spin $S = 0$ (singlet) or $S = 1$ (triplet), resulting in a total wave function of the Rydberg state of doublet (D) or quartet (Q) multiplicity (see Table A.1).

Table A.1: Possible multiplicities of the wave function of the Rydberg state.

$S\ (|\tilde{\Psi}_I^{N-2}\rangle)$	$S(|\Psi_{em}^{N-1}\rangle)$
0	$\frac{1}{2}$ (D)
1	$\frac{1}{2}$ (D), $\frac{3}{2}$ (Q)

The configuration space of the ADC/ISR(2) scheme comprises all possible 2h and 3h-1p configurations. Thus, formulas for the spin-adapted linear configurations for the Rydberg state distinguish the cases of 2h and 3h-1p states. In the following, the Greek letters $\sigma, \rho, \dots$ denote the magnetic spin quantum number, particularly, $\alpha(\beta)$ refer to $m_s = \frac{1}{2}(-\frac{1}{2})$. For notational brevity, a bar over an orbital index is used to distinguish spin β from spin α.

1. 2h dicationic configurations $|i\sigma\, j\rho\rangle$

   The resulting Rydberg states have a 2h-1p configuration $|e\kappa,\, i\sigma\, j\rho\rangle$. Here, one can distinguish two cases – when the 2h configuration consists of different or identical spatial orbitals.

   a) $i < j$

If the two holes are on different spatial Hartree-Fock orbitals, the resulting Rydberg state can be either a doublet or a quartet. There are eight possible spin configurations, out of which one can construct *two doublet* and *one quartet* spin eigenfunctions. The resulting linear combinations are presented in Table A.2 according to their magnetic spin quantum number.

Table A.2: Spin-adapted linear combinations for doublet (D) and quartet (Q) spin-configuration, originating from a 2h dicationic state. Only the configurations with magnetic spin quantum number $M_S = 1/2$ are shown. The remaining spin functions can be obtained simply by exchanging the α and β spins.

$i = j$	$i \neq j$	
D	D	Q
$\vert e, \bar{i}i\rangle$	$\frac{1}{\sqrt{2}}(\vert e, \bar{i}j\rangle - \vert e, i\bar{j}\rangle)$ $\frac{1}{\sqrt{6}}(\vert e, \bar{i}j\rangle + \vert e, i\bar{j}\rangle - 2\vert \bar{e}, \bar{i}\bar{j}\rangle)$	$\frac{1}{\sqrt{3}}(\vert e, \bar{i}j\rangle + \vert e, i\bar{j}\rangle + \vert \bar{e}, \bar{i}\bar{j}\rangle)$

Using the notations in Ref. [180], one can re-write the spin eigenfunctions as follows (only those with $M_S = \frac{1}{2}$ are presented for simplicity)

$$|D^{(1)}_{eij}\rangle = |e\rangle|S_{ij}\rangle \tag{A.2.1}$$

$$|D^{(2)}_{eij}\rangle = \frac{1}{\sqrt{3}}(|e\rangle|T_{ij}\rangle - \sqrt{2}|\bar{e}\rangle|\bar{i}\bar{j}\rangle) \tag{A.2.2}$$

$$|Q_{eij}\rangle = \frac{1}{\sqrt{3}}(\sqrt{2}|e\rangle|T_{ij}\rangle + |\bar{e}\rangle|\bar{i}\bar{j}\rangle) \tag{A.2.3}$$

b) $i = j$

If the two holes are on the same spatial Hartree-Fock orbital, the only possible value of the spin of the resulting Rydberg state is the *doublet* (see Table A.2). Using the notations in Ref. [180], the doublet spin eigenfunction can be re-written as follows

$$|D_{eii}\rangle = |e\rangle|S_{ii}\rangle \tag{A.2.4}$$

2. 3h-1p dicationic configurations $|a\gamma\, i\delta\, j\sigma\, k\rho\rangle$

The resulting Rydberg states are of 3h-2p character $|e\kappa, a\gamma\, i\delta\, j\sigma\, k\rho\rangle$. The spin-orbital indices of a 3h-1p configuration satisfy the condition given in Appendix B.2. Therefore, for the respective spatial orbital indices there are three possibilities: $i < j < k$, $i < j = k$, and $i = j < k$.

a) $i < j < k$

Out of all possible configurations of the kind $|e\kappa, a\gamma\, i\delta\, j\sigma\, k\rho\rangle$ one can construct *five doublet* ($S = 1/2$), *four quartet* ($S = 3/2$) and *one sextet* ($S = 5/2$) spin eigenfunctions. The sextet function is not considered since the multiplicity of the Rydberg states can be only doublet or quartet (see Table A.1). The remaining doublet and quartet spin eigenfunctions are presented in Table A.3.

Table A.3: The four quartet and five doublet spin-adapted linear combinations originating from a 3h-1p dicationic state. Only the configurations with magnetic spin quantum numbers $M_S = 1/2$ and $M_S = 3/2$ are presented. The remaining spin functions can be obtained simply by exchanging the α and β spins.

S	Norm	$\lvert\bar{e},\bar{a}\bar{i}\bar{j}\bar{k}\rangle$	$\lvert\bar{e},a\bar{i}\bar{j}\bar{k}\rangle$	$\lvert\bar{e},a\bar{i}j\bar{k}\rangle$	$\lvert\bar{e},a\bar{i}\bar{j}k\rangle$	$\lvert e,\bar{a}i\bar{j}\bar{k}\rangle$	$\lvert e,\bar{a}\bar{i}j\bar{k}\rangle$	$\lvert e,\bar{a}\bar{i}\bar{j}k\rangle$	$\lvert e,ai\bar{j}k\rangle$	$\lvert e,aij\bar{k}\rangle$	$\lvert e,a\bar{i}jk\rangle$
3/2	$\frac{1}{\sqrt{6}}$	1	0	0	−1	1	1	0	−1	0	−1
3/2	$\frac{1}{\sqrt{6}}$	0	1	−1	0	1	−1	0	1	0	−1
3/2	$\frac{1}{2\sqrt{3}}$	1	−1	−1	1	0	0	2	0	−2	0
3/2	$\frac{1}{2\sqrt{15}}$	3	3	3	3	−2	−2	−2	−2	−2	−2
1/2	$\frac{1}{2}$	0	0	0	0	0	1	−1	1	−1	0
1/2	$\frac{1}{2\sqrt{3}}$	2	−2	0	0	0	−1	−1	1	1	0
1/2	$\frac{1}{\sqrt{6}}$	1	1	−1	−1	−1	0	0	0	0	1
1/2	$\frac{1}{2\sqrt{3}}$	0	0	2	−2	0	−1	1	1	−1	0
1/2	$\frac{1}{2\sqrt{3}}$	0	0	0	0	2	−1	−1	−1	−1	2

Using the notations in Ref. [180], the spin eigenfunctions from Table A.3 can be re-written as

$$|Q^{(1)}_{eaijk}\rangle = \frac{1}{\sqrt{6}}\left(|\bar{e}\rangle|\bar{a}\bar{i}\bar{j}\bar{k}\rangle - |\bar{e}\rangle|a\bar{i}\bar{j}k\rangle - \sqrt{2}|e\rangle|I^{-}_{3,aijk}\rangle - \sqrt{2}|e\rangle|I^{-}_{2,aijk}\rangle\right) \tag{A.2.5}$$

$$|Q^{(2)}_{eaijk}\rangle = \frac{1}{\sqrt{6}}\left(|\bar{e}\rangle|a\bar{i}\bar{j}\bar{k}\rangle - |\bar{e}\rangle|a\bar{i}j\bar{k}\rangle - \sqrt{2}|e\rangle|I^{-}_{3,aijk}\rangle + \sqrt{2}|e\rangle|I^{-}_{2,aijk}\rangle\right) \tag{A.2.6}$$

$$\begin{aligned}|Q^{(3)}_{eaijk}\rangle = \frac{1}{2\sqrt{3}}\Big(&|\bar{e}\rangle|\bar{a}\bar{i}\bar{j}\bar{k}\rangle - |\bar{e}\rangle|a\bar{i}\bar{j}\bar{k}\rangle - |\bar{e}\rangle|a\bar{i}j\bar{k}\rangle + |\bar{e}\rangle|a\bar{i}\bar{j}k\rangle \\ &- 2\sqrt{2}|e\rangle|I^{-}_{1,aijk}\rangle\Big)\end{aligned} \tag{A.2.7}$$

$$\begin{aligned}|Q^{(4)}_{eaijk}\rangle = \frac{1}{2\sqrt{15}}\Big(&3|\bar{e}\rangle|\bar{a}\bar{i}\bar{j}\bar{k}\rangle + 3|\bar{e}\rangle|a\bar{i}\bar{j}\bar{k}\rangle + 3|\bar{e}\rangle|a\bar{i}j\bar{k}\rangle + 3|\bar{e}\rangle|a\bar{i}\bar{j}k\rangle \\ &- 2\sqrt{2}|e\rangle|T^{(1)}_{aijk}\rangle - 2\sqrt{2}|e\rangle|T^{(2)}_{aijk}\rangle - 2\sqrt{2}|e\rangle|T^{(3)}_{aijk}\rangle\Big)\end{aligned} \tag{A.2.8}$$

$$|D^{(1)}_{eaijk}\rangle = \frac{1}{\sqrt{2}}\left(|e\rangle|T^{(2)}_{aijk}\rangle - |e\rangle|T^{(1)}_{aijk}\rangle\right) \tag{A.2.9}$$

$$|D^{(2)}_{eaijk}\rangle = \frac{1}{\sqrt{6}}\left(\sqrt{2}|\bar{e}\rangle|\bar{a}\bar{i}\bar{j}\bar{k}\rangle - \sqrt{2}|\bar{e}\rangle|ai\bar{j}\bar{k}\rangle + |e\rangle|I^{-}_{1,aijk}\rangle + |e\rangle|I^{-}_{2,aijk}\rangle\right) \tag{A.2.10}$$

$$\begin{aligned}|D^{(3)}_{eaijk}\rangle = \frac{1}{\sqrt{6}}\Big(&|\bar{e}\rangle|\bar{a}\bar{i}\bar{j}\bar{k}\rangle + |\bar{e}\rangle|ai\bar{j}\bar{k}\rangle - |\bar{e}\rangle|a\bar{i}j\bar{k}\rangle - |\bar{e}\rangle|a\bar{i}\bar{j}k\rangle \\ &+ \sqrt{2}|e\rangle|I^{-}_{3,aijk}\rangle\Big)\end{aligned} \tag{A.2.11}$$

$$|D^{(4)}_{eaijk}\rangle = \frac{1}{\sqrt{6}}\left(\sqrt{2}|\bar{e}\rangle|a\bar{i}j\bar{k}\rangle - \sqrt{2}|\bar{e}\rangle|a\bar{i}\bar{j}k\rangle - |e\rangle|I^{-}_{1,aijk}\rangle + |e\rangle|I^{-}_{2,aijk}\rangle\right) \tag{A.2.12}$$

$$|D^{(5)}_{eaijk}\rangle = \frac{1}{\sqrt{6}}\left(2|e\rangle|T^{(3)}_{aijk}\rangle - |e\rangle|T^{(1)}_{aijk}\rangle - |e\rangle|T^{(2)}_{aijk}\rangle\right) \tag{A.2.13}$$

b) $i < j = k$

Out of all possible configurations of the kind $|e\kappa,\, a\gamma\, i\delta\, j\sigma\, j\rho\rangle$ one can construct *two doublet* ($S = 1/2$) and *one quartet* ($S = 3/2$) spin eigenfunctions. They are presented in Table A.4.

Table A.4: The quartet and the two doublet spin-adapted linear combinations originating from a 3h-1p dicationic state with magnetic spin quantum number $M_S = 1/2$. The remaining spin functions can be obtained simply by exchanging the α and β spins.

S	Norm	$\lvert\bar{e}, a\bar{i}j\bar{j}\rangle$	$\lvert e, \bar{a}\bar{i}j\bar{j}\rangle$	$\lvert e, aij\bar{j}\rangle$
3/2	$\frac{1}{\sqrt{3}}$	1	1	1
1/2	$\frac{1}{\sqrt{2}}$	0	1	−1
1/2	$\frac{1}{\sqrt{6}}$	2	−1	−1

Using the notations in Ref. [180], one can re-write the spin eigenfunctions as

$$|Q_{eaijj}\rangle = \frac{1}{\sqrt{3}}\left(|\bar{e}\rangle|a\bar{i}j\bar{j}\rangle + \sqrt{2}|e\rangle|S_{aijj}\rangle\right) \tag{A.2.14}$$

$$|D^{(1)}_{eaijj}\rangle = |e\rangle|T_{aijj}\rangle \tag{A.2.15}$$

$$|D^{(2)}_{eaijj}\rangle = \frac{1}{\sqrt{3}}\left(\sqrt{2}|\bar{e}\rangle|a\bar{i}j\bar{j}\rangle - |e\rangle|S_{aijj}\rangle\right) \tag{A.2.16}$$

c) $i = j < k$

Out of all possible configurations of the kind $|e\kappa,\, a\gamma\, i\delta\, i\sigma\, j\rho\rangle$ one can

Table A.5: The quartet and the two doublet spin-adapted linear combinations originating from a 3h-1p dicationic state with magnetic spin quantum number $M_S = 1/2$. The remaining spin functions can be obtained simply by exchanging the α and β spins.

S	Norm	$\lvert\bar{e}, a\bar{\imath}i\bar{\jmath}\rangle$	$\lvert e, \bar{a}\bar{\imath}i\bar{\jmath}\rangle$	$\lvert e, a\bar{\imath}ij\rangle$
$3/2$	$\frac{1}{\sqrt{3}}$	1	1	1
$1/2$	$\frac{1}{\sqrt{2}}$	0	1	-1
$1/2$	$\frac{1}{\sqrt{6}}$	2	-1	-1

construct *two doublet* ($S = 1/2$) and *one quartet* ($S = 3/2$) spin eigenfunctions. They are presented in Table A.5.

Using the notations in Ref. [180], one can re-write the spin eigenfunctions as

$$|Q_{eaiij}\rangle = \frac{1}{\sqrt{3}}\left(|\bar{e}\rangle|a\bar{\imath}i\bar{\jmath}\rangle + \sqrt{2}|e\rangle|S_{aiij}\rangle\right) \tag{A.2.17}$$

$$|D^{(1)}_{eaiij}\rangle = |e\rangle|T_{aiij}\rangle \tag{A.2.18}$$

$$|D^{(2)}_{eaiij}\rangle = \frac{1}{\sqrt{3}}\left(\sqrt{2}|\bar{e}\rangle|a\bar{\imath}i\bar{\jmath}\rangle - |e\rangle|S_{aiij}\rangle\right) \tag{A.2.19}$$

d) A special case has to be considered in a future implementation of the spin-free equations. If a virtual orbital in the expansion of the wave function of the Rydberg electron coincides with the particle orbital in the 3h-1p configuration, the configuration will vanish if the two particles have the same spin. This is also accounted for in the constraint for orthogonality of the wave functions of the dicationic core and the Rydberg electron Eq. (A.1.5). One can again consider three cases:

   i. $i < j < k$, configuration $|a, aijk\rangle$. In this case, the possible spin eigenfunctions are *a quartet* and *two doublets*. They are listed in Table A.6, where only the configurations for magnetic spin number $M_S = 1/2$ are presented.

$$|Q_{aaijk}\rangle = \frac{1}{\sqrt{3}}\left(|a\rangle|\bar{a}i\bar{\jmath}\bar{k}\rangle + |a\rangle|\bar{a}\bar{\imath}\bar{\jmath}k\rangle + |a\rangle|\bar{a}\bar{\imath}j\bar{k}\rangle\right) \tag{A.2.20}$$

$$|D^{(1)}_{aaijk}\rangle = \frac{1}{\sqrt{2}}\left(|a\rangle|\bar{a}\bar{\imath}\bar{\jmath}k\rangle - |a\rangle|\bar{a}\bar{\imath}j\bar{k}\rangle\right) \tag{A.2.21}$$

$$|D^{(2)}_{aaijk}\rangle = \frac{1}{\sqrt{6}}\left(2|a\rangle|\bar{a}i\bar{\jmath}\bar{k}\rangle - |a\rangle|\bar{a}\bar{\imath}\bar{\jmath}k\rangle - |a\rangle|\bar{a}\bar{\imath}j\bar{k}\rangle\right) \tag{A.2.22}$$

Table A.6: The quartet and the two doublet spin-adapted linear combinations originating from a $|a, aijk\rangle$ configuration with magnetic spin quantum number $M_S = 1/2$.

S	Norm	$\|a, \bar{a}i\bar{j}\bar{k}\rangle$	$\|a, \bar{a}\bar{i}j\bar{k}\rangle$	$\|a, \bar{a}\bar{i}\bar{j}k\rangle$
$3/2$	$\frac{1}{\sqrt{3}}$	1	1	1
$1/2$	$\frac{1}{\sqrt{2}}$	0	1	-1
$1/2$	$\frac{1}{\sqrt{6}}$	2	-1	-1

ii. $i < j = k$ (or $i = j < k$), configuration $|a, aijj\rangle$ ($|a, aiij\rangle$). The only possibility in this case is *a doublet* spin eigenfunction

$$\begin{aligned} |D_{aaijj}\rangle &= |a\rangle|\bar{a}\bar{i}j\bar{j}\rangle \\ |D_{aaiij}\rangle &= |a\rangle|\bar{a}\bar{i}i\bar{j}\rangle \end{aligned} \tag{A.2.23}$$

where $|D_{aaijj}\rangle$ ($|D_{aaiij}\rangle$) corresponds to magnetic spin quantum number $M_S = 1/2$.

Appendix B

ADC(2)/ISR method for properties of dicationic states

B.1 Derivation of the ISR(2) equations

In the following the derivation of the second-order representation of a general one-particle operator in terms of $(N-2)$-electron intermediate states is briefly sketched. The structure of the ISR matrix of the one-particle operator is shown in Fig. B.1.

The ISR expansions are based on the perturbation theoretical (PT) expansion of the N-electron ground state, and therefore it is helpful to recall the latter. In intermediate normalisation, the N-electron ground state can be expanded through second order according to

$$|\Psi_0'\rangle = |\Phi_0\rangle + |\Psi_0^{(1)}\rangle + |\Psi_0^{(2)}\rangle + O(3) \qquad \text{(B.1.1)}$$

The first-order term,

$$|\Psi_0^{(1)}\rangle = \frac{1}{4}\sum_{abkl} w_{abkl} c_a^\dagger c_b^\dagger c_k c_l |\Phi_0\rangle \qquad \text{(B.1.2)}$$

$\tilde{\boldsymbol{D}}_{11}(0-2)$	$\tilde{\boldsymbol{D}}_{12}(0-1)$
h.c.	$\tilde{\boldsymbol{D}}_{22}(0)$

Figure B.1: Block structure of the second-order ISR/ADC(2) matrix $\tilde{\boldsymbol{D}}$ for a single-particle operator $\hat{D}$. The numbers in brackets represent the orders of perturbation theory in the respective perturbation theoretical expansions.

simply reflects the admixture of double excitations. The second-order term is already rather involved, comprising contributions associated with single, double, triple, and quadruple excitations

$$|\Psi_0^{(2)}\rangle = |\Psi_{ph}^{(2)}\rangle + |\Psi_{2p-2h}^{(2)}\rangle + |\Psi_{3p-3h}^{(2)}\rangle + |\Psi_{4p-4h}^{(2)}\rangle \tag{B.1.3}$$

Fortunately, in the derivation of the ISR(2) expressions only the second-order term associated with the p-h excitations will come into play. To proceed to the normalised N-electron ground state, $|\Psi_0\rangle = N_0|\Psi_0'\rangle$, the normalisation constant, $N_0 = \langle\Psi_0'|\Psi_0'\rangle^{-\frac{1}{2}}$, needs to be expanded through second order

$$N_0 = 1 - \frac{1}{8}\sum_{abkl}|w_{abkl}|^2 + O(3) \tag{B.1.4}$$

As a result, the second-order expansion of the normalised ground state is given by

$$|\Psi_0(2)\rangle = (1 + X_0^{(2)})|\Phi_0\rangle + |\Psi_0^{(1)}\rangle + |\Psi^{(2)}\rangle \tag{B.1.5}$$

where

$$X_0^{(2)} = -\frac{1}{8}\sum_{abkl}|w_{abkl}|^2 \tag{B.1.6}$$

As already mentioned, only the p-h contribution to the second-order wave function,

$$|\Psi_{ph}^{(2)}\rangle = \sum_{ak} X_{ak}^{(2)} c_a^\dagger c_k|\Phi_0\rangle. \tag{B.1.7}$$

is needed in the ISR(2) derivation. Here, $X_{ak}^{(2)}$ denote the second-order expansion coefficients of the p-h admixtures to the ground state,

$$X_{ak}^{(2)} = \langle\Phi_0|c_k^\dagger c_a|\Psi_0^{(2)}\rangle \tag{B.1.8}$$

Note that the $X_{ak}^{(2)}$ coefficients through second order can be identified with the p-h components of the one-particle density matrix,

$$\rho_{ak} = \langle\Psi_0|c_k^\dagger c_a|\Psi_0\rangle = X_{ak}^{(2)} + O(3) \tag{B.1.9}$$

The intermediate 2h-states, forming the lowest excitation class, are simply obtained by symmetrical orthonormalisation of the precursor states, $|\Psi_{kl}^{\#}\rangle = c_k c_l|\Psi_0\rangle$,

$$|\tilde{\Psi}_{ij}\rangle = \sum_{kl}(S^{-\frac{1}{2}})_{kl,ij} c_k c_l|\Psi_0\rangle \tag{B.1.10}$$

where

$$S_{ij,kl} = \langle\Psi_0|c_j^\dagger c_i^\dagger c_k c_l|\Psi_0\rangle \tag{B.1.11}$$

is the overlap matrix of the precursor states. The low-order perturbation expansion of $\boldsymbol{S}$ is of the simple form

$$\boldsymbol{S} = \mathbf{1} + \boldsymbol{S}^{(2)} + O(3) \tag{B.1.12}$$

lacking a first-order contribution. More specifically, the expansion through second order can be written as

$$S_{ij,kl} = \delta_{ik}\delta_{jl}(1 + 2X_0^{(2)}) + \langle\Psi_0^{(1)}|c_j^\dagger c_i^\dagger c_k c_l|\Psi_0^{(1)}\rangle + O(3) \tag{B.1.13}$$

which shows that there are two distinct second-order contributions associated with the normalisation of the ground state and the first-order double-excitation admixtures.

Now the PT expansion through second order for the property matrix elements in the 2h diagonal block can be formulated,

$$\tilde{D}_{ij,i'j'} = \langle\tilde{\Psi}_{ij}|\hat{D}|\tilde{\Psi}_{i'j'}\rangle = \sum_{kl,k'l'}(S^{-\frac{1}{2}})_{ij,kl}\langle\Psi_0|c_l^\dagger c_k^\dagger \hat{D} c_{k'} c_{l'}|\Psi_0\rangle(S^{-\frac{1}{2}})_{k'l',i'j'} \tag{B.1.14}$$

In zeroth order, the intermediate 2h-states are simply given by the CI configurations, $|\Phi_{ij}\rangle = c_i c_j|\Phi_0\rangle$, and the zeroth-order ISR matrix elements can be evaluated according to

$$\tilde{D}^{(0)}_{ij,i'j'} = \langle\Phi_{ij}|\hat{D}|\Phi_{i'j'}\rangle \tag{B.1.15}$$

As is easily established, the first-order contributions vanish. In second order, the ISR matrix elements consist of three distinct terms,

$$\begin{aligned}\tilde{D}^{(2)}_{ij,i'j'} &= \sum_{kl}(S^{-\frac{1}{2}})^{(2)}_{ij,kl}\langle\Phi_{kl}|\hat{D}|\Phi_{i'j'}\rangle + \sum_{k'l'}\langle\Phi_{ij}|\hat{D}|\Phi_{k'l'}\rangle(S^{-\frac{1}{2}})^{(2)}_{k'l',i'j'} \\ &+ \langle\Phi_{ij}|\hat{D}c_{i'}c_{j'}|\Psi^{(2)}_{ph}\rangle + h.c. \\ &+ \langle\Psi_0^{(1)}|c_j^\dagger c_i^\dagger \hat{D} c_{i'} c_{j'}|\Psi_0^{(1)}\rangle\end{aligned} \tag{B.1.16}$$

associated with the orthonormalisation (first line on the right-hand side), the p-h admixtures in the ground state (second line), and the (first-order) 2p-2h admixtures in the ground state (third line), respectively. The evaluation of the first two contributions is rather straightforward, using here Eqs. (B.1.13, B.1.7, B.1.9). The evaluation of the term in the third line of Eq. (B.1.16) is more demanding. Here it is advisable to make use of the commutator relations

$$\left[c_j^\dagger c_i^\dagger, \hat{D}\right] = \sum_p d_{pi} c_p^\dagger c_j^\dagger - \sum_p d_{pj} c_p^\dagger c_i^\dagger .$$

$$\left[\hat{D}, c_{i'}c_{j'}\right] = \sum_q d_{i'q}c_{j'}c_q - \sum_q d_{j'q}c_{i'}c_q \tag{B.1.17}$$

and move the $\hat{D}$ operator either to the left or to the right-hand side of the c operators. To maintain an explicitly hermitian form, this reformulation can be arranged according to

$$\begin{aligned}\langle\Psi_0^{(1)}|c_j^\dagger c_i^\dagger \hat{D} c_{i'}c_{j'}|\Psi_0^{(1)}\rangle &= \tfrac{1}{2}\langle\Psi_0^{(1)}|\hat{D}c_j^\dagger c_i^\dagger c_{i'}c_{j'}|\Psi_0^{(1)}\rangle + h.c.\\ &+ \tfrac{1}{2}\langle\Psi_0^{(1)}|[c_j^\dagger c_i^\dagger, \hat{D}]c_{i'}c_{j'}|\Psi_0^{(1)}\rangle + h.c.\end{aligned} \tag{B.1.18}$$

Note that the h.c. contributions arise from moving $\hat{D}$ to the right-hand side. Inserting the explicit commutator expressions according to Eqs. (B.1.17) yields

$$\begin{aligned}\langle\Psi_0^{(1)}|c_j^\dagger c_i^\dagger \hat{D} c_{i'}c_{j'}|\Psi_0^{(1)}\rangle = &-\tfrac{1}{2}\sum_r d_{ri}\langle\Psi_0^{(1)}|c_j^\dagger c_r^\dagger c_{i'}c_{j'}|\Psi_0^{(1)}\rangle\\ &-\tfrac{1}{2}\sum_r d_{rj}\langle\Psi_0^{(1)}|c_r^\dagger c_i^\dagger c_{i'}c_{j'}|\Psi_0^{(1)}\rangle + h.c.\\ &+\tfrac{1}{2}\langle\Psi_0^{(1)}|\hat{D}c_j^\dagger c_i^\dagger c_{i'}c_{j'}|\Psi_0^{(1)}\rangle + h.c.\end{aligned} \tag{B.1.19}$$

The terms in the first line on the right-hand side can be seen to cancel the corresponding contributions arising from the first line on the right-hand side of Eq. (B.1.16). To evaluate the matrix elements in the second line of Eq. (B.1.19), one may move the creation operators to the left side of the operator product,

$$c_j^\dagger c_i^\dagger c_{i'}c_{j'} = \delta_{ii'}\delta_{jj'} - \delta_{ii'}c_{j'}c_j^\dagger + \delta_{ij'}c_{i'}c_j^\dagger + \delta_{ji'}c_{j'}c_i^\dagger - \delta_{jj'}c_{i'}c_i^\dagger + c_{i'}c_{j'}c_j^\dagger c_i^\dagger \tag{B.1.20}$$

The emerging terms can now be applied separately to the first-order double-excitation admixtures (B.1.2) in the N-electron ground state, yielding expressions of the type

$$c_{j'}c_j^\dagger|\Psi_0^{(1)}\rangle = \sum_{a<b,k\neq j,j'} w_{abkj}c_a^\dagger c_b^\dagger c_k c_{j'}|\Phi_0\rangle \tag{B.1.21}$$

that is, again sums over double excitations. Thus, the matrix elements $\langle\Psi_0^{(1)}|\hat{D}c_j^\dagger c_i^\dagger$ $c_{i'}c_{j'}|\Psi_0^{(1)}\rangle$ can be evaluated as matrix elements of a one-particle operator taken with respect to doubly-excited HF configurations. This gives rise to the 15 distinct contributions (B.2.9 – B.2.23).

The ISR matrix elements of the 2h/3h-1p coupling block are needed through first order. The zeroth-order contributions

$$\tilde{D}^{(0)}_{ij,a'i'j'k'} = \langle\Phi_{ij}|\hat{D}|\Phi_{a'i'j'k'}\rangle \tag{B.1.22}$$

can readily be evaluated. The first-order expressions are simply given by

$$\tilde{D}^{(1)}_{ij,a'i'j'k'} = \langle \Psi_0^{(1)} | c_j^\dagger c_i^\dagger \hat{D} | \Phi_{a'i'j'k'} \rangle \tag{B.1.23}$$

since there is no contribution associated with $|\tilde{\Psi}^{(1)}_{ij}\rangle = c_i c_j |\Psi_0^{(1)}\rangle$. Finally, the 3h-1p diagonal block is needed only in zeroth order

$$\tilde{D}_{aijk,a'i'j'k'} = \langle \Phi_{aijk} | \hat{D} | \Phi_{a'i'j'k'} \rangle \tag{B.1.24}$$

The explicit expressions are listed in B.2.

B.2 Dicationic ISR(2) expressions for one-particle operators

In the following the $(N-2)$-electron ISR of a general one-particle operator is given explicitly through second-order of perturbation theory (ISR(2)). The matrix elements

$$\tilde{D}_{IJ} = \langle \tilde{\Psi}_I^{N-2} | \hat{D} | \tilde{\Psi}_J^{N-2} \rangle, \;\; I, J \in \{2h, 3h\text{-}1p\} \tag{B.2.1}$$

need to be expanded through 2nd, 1st, and zeroth order (in the residual electron repulsion), depending on the respective matrix sub-blocks; the configuration space at the ISR(2) level is spanned by the 2h-configurations, $I \equiv ij, i < j$, and 3h-1p configurations, $I \equiv (aijk, i < j < k$. (As usual, $a, b, c, \ldots$ and $i, j, k, \ldots$ denote unoccupied (virtual) and occupied spin-orbitals, respectively, referring to the N-electron ground state.) A general one-particle operator can be written in the form

$$\hat{D} = \sum d_{pq} c_p^\dagger c_q \tag{B.2.2}$$

where $d_{pq} = \langle p | \hat{d} | q \rangle$ denote one-particle integrals of the respective operator.

For brevity we will use the notation

$$w_{abkl} = \frac{V_{ab[kl]}}{\epsilon_a + \epsilon_b - \epsilon_k - \epsilon_l} \tag{B.2.3}$$

where $V_{pq[rs]} = V_{pqrs} - V_{pqsr}$ denote anti-symmetrised Coulomb integrals, and ϵ_p are HF orbital energies. The N-electron ground-state expectation value,

$$D_0 = \langle \Psi_0 | \hat{D} | \Psi_0 \rangle \tag{B.2.4}$$

enters the following expressions in its 2nd-order PT expansion,

$$D_0(2) = D_0^{(0)} + D_0^{(2)} \tag{B.2.5}$$

where the zeroth-order term is obtained according to

$$D_0^{(0)} = \langle \Phi_0 | \hat{D} | \Phi_0 \rangle = \sum d_{kk} \tag{B.2.6}$$

Note that the first-order contribution vanishes, $D_0^{(1)} = 0$. Finally, $\rho^{(2)}_{ak}$ denote the second-order contributions to the one-particle density matrix elements,

$$\rho_{ak} = \langle \Psi_0 | c_k^\dagger c_a | \Psi_0 \rangle \tag{B.2.7}$$

2h diagonal block:

Here the expansions extend through 2nd order; the first-order contributions vanish.

$$\begin{aligned} \tilde{D}_{ij,i'j'} = {} & \delta_{ii'}\delta_{jj'}D_0(2) - \delta_{ii'}d_{j'j} - \delta_{jj'}d_{i'i} + \delta_{ij'}d_{i'j} + \delta_{ji'}d_{j'i} \\ & \left(-\delta_{ii'}\sum_a \rho^{(2)}_{aj} d_{j'a} - \delta_{jj'}\sum_a \rho^{(2)}_{ai} d_{i'a} + \delta_{ij'}\sum_a \rho^{(2)}_{aj} d_{i'a} + \delta_{ji'}\sum_a \rho^{(2)}_{ai} d_{j'a} \right) \\ & + h.c. + \sum_{\mu=1}^{15} D^{(2,\mu)}_{ij,i'j'} \end{aligned} \tag{B.2.8}$$

where

$$D^{(2,1)}_{ij,i'j'} = -\delta_{ii'}\tfrac{1}{2}\sum_{a,b,a',k} w^*_{a'bkj'} w_{abkj} d_{a'a} + h.c. \tag{B.2.9}$$

$$D^{(2,2)}_{ij,i'j'} = \delta_{ii'}\tfrac{1}{4}\sum_{a,b,k,k'} w^*_{abkk'} w_{abkj} d_{j'k'} + h.c. \tag{B.2.10}$$

$$D^{(2,3)}_{ij,i'j'} = \delta_{ii'}\tfrac{1}{4}\sum_{a,b,k,k'} w^*_{abk'j'} w_{abkj} d_{kk'} + h.c. \tag{B.2.11}$$

$$D^{(2,4)}_{ij,i'j'} = -\delta_{jj'}\tfrac{1}{2}\sum_{a,b,a',k} w^*_{a'bki'} w_{abki} d_{a'a} + h.c. \tag{B.2.12}$$

$$D^{(2,5)}_{ij,i'j'} = \delta_{jj'}\tfrac{1}{4}\sum_{a,b,k,k'} w^*_{abkk'} w_{abki} d_{i'k'} + h.c. \tag{B.2.13}$$

$$D^{(2,6)}_{ij,i'j'} = \delta_{jj'}\tfrac{1}{4}\sum_{a,b,k,k'} w^*_{abk'i'} w_{abki} d_{kk'} + h.c. \tag{B.2.14}$$

$$D^{(2,7)}_{ij,i'j'} = \delta_{ij'}\tfrac{1}{2}\sum_{a,b,a',k} w^*_{a'bki'} w_{abkj} d_{a'a} + h.c. \tag{B.2.15}$$

$$D^{(2,8)}_{ij,i'j'} = -\delta_{ij'}\tfrac{1}{4}\sum_{a,b,k,k'} w^*_{abkk'} w_{abkj} d_{i'k'} + h.c. \tag{B.2.16}$$

$$D^{(2,9)}_{ij,i'j'} = -\delta_{ij'}\tfrac{1}{4}\sum_{a,b,k,k'} w^*_{abk'i'} w_{abkj} d_{kk'} \;+ h.c. \tag{B.2.17}$$

$$D^{(2,10)}_{ij,i'j'} = \delta_{ji'}\tfrac{1}{2}\sum_{a,b,a',k} w^*_{a'bkj'} w_{abki} d_{a'a} \;+ h.c. \tag{B.2.18}$$

$$D^{(2,11)}_{ij,i'j'} = -\delta_{ji'}\tfrac{1}{4}\sum_{a,b,k,k'} w^*_{abkk'} w_{abki} d_{j'k'} \;+ h.c. \tag{B.2.19}$$

$$D^{(2,12)}_{ij,i'j'} = -\delta_{ji'}\tfrac{1}{4}\sum_{a,b,k,k'} w^*_{abk'j'} w_{abki} d_{kk'} \;+ h.c. \tag{B.2.20}$$

$$D^{(2,13)}_{ij,i'j'} = \sum_{a,b,a'} w^*_{a'bi'j'} w_{abij} d_{a'a} \tag{B.2.21}$$

$$D^{(2,14)}_{ij,i'j'} = -\tfrac{1}{4}\sum_{a,b,k} w^*_{abi'k} w_{abij} d_{j'k} \;+ h.c. \tag{B.2.22}$$

$$D^{(2,15)}_{ij,i'j'} = -\tfrac{1}{4}\sum_{a,b,k} w^*_{abkj'} w_{abij} d_{i'k} \;+ h.c. \tag{B.2.23}$$

The 2nd-order expansion of the ground-state expectation value of the property operator, $D_0(2)$, can be obtained using the property option of an ADC code for the one-particle Green's function (1p-GF), either at the ADC(2) or ADC(3) level [67]. Moreover, the 1p-GF ADC approach can be used to compute the one-particle density matrix elements, ρ_{ak}, resorting either to the so-called Dyson expansion method (DEM) or the $\Sigma(4+)$ method [67].

2h/3h-1p coupling block:

The expansions extend through 1st order.

$$\tilde{D}_{ij,a'i'j'k'} = \delta_{ii'}\delta_{jj'}d_{k'a'} + \delta_{ij'}\delta_{jk'}d_{i'a'} - \delta_{ii'}\delta_{jk'}d_{j'a'} \tag{B.2.24}$$

$$-\delta_{ii'}\delta_{jj'}\sum_{b,k} w^*_{a'bk'k} d_{bk} \tag{B.2.25}$$

$$-\delta_{ij'}\delta_{jk'}\sum_{b,k} w^*_{a'bi'k} d_{bk} \tag{B.2.26}$$

$$+\delta_{ii'}\delta_{jk'}\sum_{b,k} w^*_{a'bj'k} d_{bk} \tag{B.2.27}$$

$$-\delta_{ii'}\sum_{b} w^*_{a'bj'k'} d_{bj} \tag{B.2.28}$$

$$+\delta_{ji'}\sum_{b} w^*_{a'bj'k'} d_{bi} \tag{B.2.29}$$

$$-\delta_{ik'}\sum_{b} w^*_{a'bi'j'} d_{bj} \tag{B.2.30}$$

$$+\delta_{jk'}\sum_b w^*_{a'bi'j'}d_{bi} \tag{B.2.31}$$

$$+\delta_{ij'}\sum_b w^*_{a'bi'k'}d_{bj} \tag{B.2.32}$$

$$-\delta_{jj'}\sum_b w^*_{a'bi'k'}d_{bi} \tag{B.2.33}$$

3h-1p diagonal block:

Only zeroth-order terms are needed in the 3h-1p diagonal block, that is,

$$\tilde{D}_{aijk,a'i'j'k'} = \langle\Phi_{aijk}|\hat{D}|\Phi_{a'i'j'k'}\rangle \tag{B.2.34}$$

which yields

$$\begin{aligned}\tilde{D}_{aijk,a'i'j'k'} &= \delta_{aa'}\delta_{ii'}\delta_{jj'}\delta_{kk'}D_0(0) + \delta_{ii'}\delta_{jj'}\delta_{kk'}d_{aa'} \\ &+\delta_{aa'}\delta_{ii'}(-\delta_{jj'}d_{k'k} + \delta_{jk'}d_{j'k} - \delta_{kk'}d_{j'j} + \delta_{kj'}d_{k'j}) \\ &+\delta_{aa'}\delta_{kk'}(\delta_{ij'}d_{i'j} - \delta_{jj'}d_{i'i} + \delta_{ji'}d_{j'i}) \\ &-\delta_{aa'}\delta_{ij'}\delta_{jk'}d_{i'k} - \delta_{aa'}\delta_{ji'}\delta_{kj'}d_{k'i}\end{aligned} \tag{B.2.35}$$

References

[1] R. W. Fink, R. C. Jopson, H. Mark, and C. D. Swift, Rev. Mod. Phys. **38**, 513 (1966).

[2] D. S. Urch, in X-Ray Spectroscopy in Atomic and Solid State Physics, edited by J. Ferreira and M. Ramos (Springer US, 1988), vol. 187 of NATO ASI Series, pp. 155–175, ISBN 978-1-4612-8054-5.

[3] H. H. Jaffe and A. L. Miller, J. Chem. Educ. **43**, 469 (1966).

[4] L. S. Cederbaum, J. Zobeley, and F. Tarantelli, Phys. Rev. Lett. **79**, 4778 (1997).

[5] R. Santra, J. Zobeley, L. S. Cederbaum, and N. Moiseyev, Phys. Rev. Lett. **85**, 4490 (2000).

[6] U. Hergenhahn, J. Electron Spectrosc. Relat. Phenom. **184**, 78 (2011).

[7] T. Jahnke, H. Sann, T. Havermeier, K. Kreidi, C. Stuck, M. Meckel, M. Schöffler, N. Neumann, R. Wallauer, S. Voss, et al., Nat. Phys. **6**, 139 (2010).

[8] M. Mucke, M. Braune, S. Barth, M. Förstel, T. Lischke, V. Ulrich, T. Arion, U. Becker, A. Bradshaw, and U. Hergenhahn, Nat. Phys. **6**, 143 (2010).

[9] V. Averbukh and L. S. Cederbaum, Phys. Rev. Lett. **96**, 053401 (2006).

[10] A. Bande, K. Gokhberg, and L. S. Cederbaum, J. Chem. Phys. **135**, 144112 (2011).

[11] I. Cherkes and N. Moiseyev, Phys. Rev. B **83**, 113303 (2011).

[12] S. Barth, S. Marburger, O. Kugeler, V. Ulrich, S. Joshi, A. M. Bradshaw, and U. Hergenhahn, Chem. Phys. **329**, 246 (2006).

[13] P. H. P. Harbach, M. Schneider, S. Faraji, and A. Dreuw, J. Phys. Chem. Lett. **4**, 943 (2013).

[14] G. Öhrwall, M. Tchaplyguine, M. Lundwall, R. Feifel, H. Bergersen, T. Rander, A. Lindblad, J. Schulz, S. Peredkov, S. Barth, et al., Phys. Rev. Lett. **93**, 173401 (2004).

[15] A. I. Kuleff and L. S. Cederbaum, Phys. Rev. Lett. **98**, 083201 (2007).

[16] W. Pokapanich, H. Bergersen, I. L. Bradeanu, R. R. T. Marinho, A. Lindblad, S. Legendre, A. Rosso, S. Svensson, O. Björneholm, M. Tchaplyguine, et al., J. Am. Chem. Soc. **131**, 7264 (2009).

[17] W. Pokapanich, N. V. Kryzhevoi, N. Ottosson, S. Svensson, L. S. Cederbaum, G. Öhrwall, and O. Björneholm, J. Am. Chem. Soc. **133**, 13430 (2011).

[18] H.-K. Kim, J. Titze, M. Schöffler, F. Trinter, M. Waitz, J. Voigtsberger, H. Sann, M. Meckel, C. Stuck, U. Lenz, et al., P. Natl. Acad. Sci. USA **108**, 11821 (2011).

[19] H. K. Kim, H. Gassert, M. S. Schöffler, J. N. Titze, M. Waitz, J. Voigtsberger, F. Trinter, J. Becht, A. Kalinin, N. Neumann, et al., Phys. Rev. A **88**, 042707 (2013).

[20] S. Yan, P. Zhang, X. Ma, S. Xu, B. Li, X. L. Zhu, W. T. Feng, S. F. Zhang, D. M. Zhao, R. T. Zhang, et al., Phys. Rev. A **88**, 042712 (2013).

[21] S. Yan, P. Zhang, X. Ma, S. Xu, S. X. Tian, B. Li, X. L. Zhu, W. T. Feng, and D. M. Zhao, Phys. Rev. A **89**, 062707 (2014).

[22] R. Santra and L. S. Cederbaum, Phys. Rev. Lett. **90**, 153401 (2003).

[23] Y. Morishita, X.-J. Liu, N. Saito, T. Lischke, M. Kato, G. Prümper, M. Oura, H. Yamaoka, Y. Tamenori, I. H. Suzuki, et al., Phys. Rev. Lett. **96**, 243402 (2006).

[24] S. D. Stoychev, A. I. Kuleff, F. Tarantelli, and L. S. Cederbaum, J. Chem. Phys. **128**, 014307 (2008).

[25] E. Fasshauer, M. Förstel, S. Pallmann, M. Pernpointner, and U. Hergenhahn, New J. Phys. **16**, 103026 (2014).

[26] S. D. Stoychev, A. I. Kuleff, and L. S. Cederbaum, J. Am. Chem. Soc. **133**, 6817 (2011).

[27] V. Stumpf, K. Gokhberg, and L. S. Cederbaum, ArXiv e-prints (2015), `1505.02079`.

[28] K. Takakura, Acta Oncol. **35**, 883 (1996).

[29] E. Alizadeh, T. M. Orlando, and L. Sanche, Ann. Rev. Phys. Chem. **66**, 379 (2015).

[30] P. O'Neill, D. L. Stevens, and E. F. Garman, J. Synchrotron Radiat. **9**, 329 (2002).

[31] G. A. Grieves and T. M. Orlando, Phys. Rev. Lett. **107**, 016104 (2011).

[32] K. Gokhberg, P. Kolorenč, A. I. Kuleff, and L. S. Cederbaum, Nature **505**, 661 (2014).

[33] U. Hergenhahn, Int. J. Radiat. Biol. **88**, 871 (2012).

[34] N. V. Kryzhevoi and L. S. Cederbaum, Angew. Chem. Int. Ed. **50**, 1306 (2011).

[35] O. Carugo and K. D. Carugo, Trends Biochem. Sci. **30**, 213 (2005).

[36] H. Aksela, S. Aksela, and H. Pulkkinen, Phys. Rev. A **37**, 1798 (1988).

[37] G. B. Armen, H. Aksela, T. Åberg, and S. Aksela, J. Phys. B At. Mol. Opt. Phys. **33**, R49 (2000).

[38] J. A. de Gouw, J. van Eck, A. C. Peters, J. van der Weg, and H. G. M. Heideman, J. Phys. B At. Mol. Opt. Phys. **28**, 2127 (1995).

[39] P. Bolognesi, P. O'Keeffe, Y. Ovcharenko, M. Coreno, L. Avaldi, V. Feyer, O. Plekan, K. C. Prince, W. Zhang, and V. Carravetta, J. Chem. Phys. **133**, 034302 (2010).

[40] W. Wurth, G. Rocker, P. Feulner, R. Scheuerer, L. Zhu, and D. Menzel, Phys. Rev. B **47**, 6697 (1993).

[41] F. Federmann, O. Björneholm, A. Beutler, and T. Möller, Phys. Rev. Lett. **73**, 1549 (1994).

[42] O. Björneholm, F. Federmann, F. Fössing, and T. Möller, Phys. Rev. Lett. **74**, 3017 (1995).

[43] J. Mursu, H. Aksela, O.-P. Sairanen, A. Kivimäki, E. Nõmmiste, A. Ausmees, S. Svensson, and S. Aksela, J. Phys. B At. Mol. Opt. Phys. **29**, 4387 (1996).

[44] F. Trinter, M. S. Schöffler, H.-K. Kim, F. P. Sturm, K. Cole, N. Neumann, A. Vredenborg, J. Williams, I. Bocharova, R. Guillemin, et al., Nature **505**, 664 (2014).

[45] P. O'Keeffe, E. Ripani, P. Bolognesi, M. Coreno, M. Devetta, C. Callegari, M. Di Fraia, K. C. Prince, R. Richter, M. Alagia, et al., J. Phys. Chem. Lett. **4**, 1797 (2013).

[46] M. Kimura, H. Fukuzawa, K. Sakai, S. Mondal, E. Kukk, Y. Kono, S. Nagaoka, Y. Tamenori, N. Saito, and K. Ueda, Phys. Rev. A **87**, 043414 (2013).

[47] M. Kimura, H. Fukuzawa, T. Tachibana, Y. Ito, S. Mondal, M. Okunishi, M. Schöffler, J. Williams, Y. Jiang, Y. Tamenori, et al., J. Phys. Chem. Lett. **4**, 1838 (2013).

[48] M. Meyer, E. v. Raven, B. Sonntag, and J. Hansen, Phys. Rev. A **43**, 177 (1991).

[49] K. Ueda and H. Fukuzawa (private communication).

[50] G. Jabbari, T. Miteva, K. Gokhberg, P. O'Keeffe, A. Ciavardini, P. Bolognesi, M. Coreno, L. Avaldi, E. Keshavarz, M. Ghandehari, et al. (in preparation).

[51] D. Nordlund, H. Ogasawara, H. Bluhm, O. Takahashi, M. Odelius, M. Nagasono, L. G. M. Pettersson, and A. Nilsson, Phys. Rev. Lett. **99**, 217406 (2007).

[52] L. González, D. Escudero, and L. Serrano-Andrés, Chem. Phys. Chem. **13**, 28 (2012), ISSN 1439-7641.

[53] A. Szabo and N. Ostlund, Modern Quantum Chemistry: Introduction to Advanced Electronic Structure Theory (Courier Dover Publications, 1996).

[54] F. Jensen, Introduction to Computational Chemistry, Second edition (John Wiley & Sons, Ltd., 2007).

[55] K. Raghavachari and J. B. Anderson, J. Phys. Chem. **100**, 12960 (1996).

[56] T. Helgaker, P. Jørgensen, and J. Olsen, Molecular electronic-structure theory (John Wiley & Sons, Ltd., 2000).

[57] P. G. Szalay, T. Müller, G. Gidofalvi, H. Lischka, and R. Shepard, Chem. Rev. **112**, 108 (2012).

[58] I. Shavitt, Mol. Phys. **94**, 3 (1998).

[59] A. L. Fetter and J. D. Walecka, Quantum Theory of Many-Particle Systems (Dover Publications, 2003).

[60] R. D. Mattuck, A Guide to Feynman Diagrams in the Many-Body Problem (Dover Publications, 1992).

[61] J. Schirmer, L. S. Cederbaum, and O. Walter, Phys. Rev. A **28**, 1237 (1983).

[62] J. Schirmer, Phys. Rev. A **26**, 2395 (1982).

[63] J. Schirmer and A. Barth, Z. Phys. A **317**, 267 (1984).

[64] J. Schirmer, Phys. Rev. A **43**, 4647 (1991).

[65] F. Mertins and J. Schirmer, Phys. Rev. A **53**, 2140 (1996).

[66] J. Schirmer and A. B. Trofimov, J. Chem. Phys. **120**, 11449 (2004).

[67] A. B. Trofimov and J. Schirmer, J. Chem. Phys. **123**, 144115 (2005).

[68] Y. Velkov, T. Miteva, N. Sisourat, and J. Schirmer, J. Chem. Phys. **135**, 154113 (2011).

[69] J. Schirmer and F. Mertins, Int. J. Quant. Chem. **58**, 329 (1996).

[70] A. Barth and J. Schirmer, J. Phys. B At. Mol. Opt. Phys. **18**, 867 (1985).

[71] L. S. Cederbaum, W. Domcke, and J. Schirmer, Phys. Rev. A **22**, 206 (1980).

[72] A. Barth and L. S. Cederbaum, Phys. Rev. A **23**, 1038 (1981).

[73] A. B. Trofimov and J. Schirmer, J. Phys. B At. Mol. Opt. Phys. **28**, 2299 (1995).

[74] A. Trofimov, T. Moskovskaya, E. Gromov, N. Vitkovskaya, and J. Schirmer, J. Sruct. Chem. **41**, 483 (2000).

[75] A. B. Trofimov, T. E. Moskovskaya, E. V. Gromov, H. Köppel, and J. Schirmer, Phys. Rev. A **64**, 022504 (2001).

[76] O. Plekan, V. Feyer, R. Richter, M. Coreno, M. de Simone, K. Prince, A. Trofimov, E. Gromov, I. Zaytseva, and J. Schirmer, Chem. Phys. **347**, 360 (2008).

[77] The wave function ansatz as well as the derivation of the equations ware done by L. S. Cederbaum. The derivation of the matrix equations and the spin-free formulas was done by the author.

[78] A. Siegert, Phys. Rev. **56**, 750 (1939).

[79] V. I. Kukulin, V. M. Krasnopol'sky, and J. Horáček, Theory of Resonances (Springer Netherlands, Dordrecht, 1989).

[80] S. Klaiman and I. Gilary, in Advances in Quantum Chemistry (Academic Press, 2012), vol. 63, pp. 1–31, ISBN 9780123970091.

[81] D. J. Griffiths, Introduction to quantum mechanics (Prentice Hall, Inc., 1995).

[82] N. Moiseyev, Phys. Rep. **302**, 212 (1998).

[83] W. P. Reinhardt, Ann. Rev. Phys. Chem. **33**, 223 (1982).

[84] J. Aguilar and J. Combes, Comm. Math. Phys. **22**, 269 (1971).

[85] E. Balslev and J. Combes, Comm. Math. Phys. **22**, 280 (1971).

[86] U. V. Riss and H.-D. Meyer, J. Phys. B At. Mol. Opt. Phys. **26**, 4503 (1993).

[87] U. Fano, Phys. Rev. **124**, 1866 (1961).

[88] R. Santra and L. S. Cederbaum, Phys. Rev. **368**, 1 (2002).

[89] R. Santra, L. Cederbaum, and H.-D. Meyer, Chem. Phys. Lett. **303**, 413 (1999).

[90] R. Santra and L. S. Cederbaum, J. Chem. Phys. **117**, 5511 (2002).

[91] S. Feuerbacher, T. Sommerfeld, R. Santra, and L. S. Cederbaum, J. Chem. Phys. **118**, 6188 (2003).

[92] A. Ghosh, S. Pal, and N. Vaval, J. Chem. Phys. **139**, 064112 (2013).

[93] T.-C. Jagau, D. Zuev, K. B. Bravaya, E. Epifanovsky, and A. I. Krylov, J. Phys. Chem. Lett. **5**, 310 (2014).

[94] J. Muga, J. Palao, B. Navarro, and I. Egusquiza, Phys. Rep. **395**, 357 (2004).

[95] T. Sommerfeld and R. Santra, Int. J. Quant. Chem. **82**, 218 (2001).

[96] R. Santra, J. Breidbach, J. Zobeley, and L. S. Cederbaum, J. Chem. Phys. **112**, 9243 (2000).

[97] N. Vaval and L. S. Cederbaum, J. Chem. Phys. **126**, 164110 (2007).

[98] V. Averbukh and L. S. Cederbaum, J. Chem. Phys. **123**, 204107 (2005).

[99] G. Howat, T. Åberg, and O. Goscinski, J. Phys. B At. Mol. Opt. Phys. **11**, 1575 (1978).

[100] P. W. Langhoff, in Electron-Molecule and Photon-Molecule Collisions, edited by T. Rescigno, V. McKoy, and B. Schneider (Plenum Press, New York and London, 1979).

[101] A. U. Hazi, in Electron-Molecule and Photon-Molecule Collisions, edited by T. Rescigno, V. McKoy, and B. Schneider (Plenum Press, New York and London, 1979).

[102] P. Kolorenč, V. Averbukh, K. Gokhberg, and L. Cederbaum, J. Chem. Phys. **129**, 244102 (2008).

[103] V. Averbukh and L. S. Cederbaum, J. Chem. Phys. **125**, 094107 (2006).

[104] V. Stumpf, P. Kolorenč, K. Gokhberg, and L. S. Cederbaum, Phys. Rev. Lett. **110**, 258302 (2013).

[105] V. Stumpf, N. V. Kryzhevoi, K. Gokhberg, and L. S. Cederbaum, Phys. Rev. Lett. **112**, 193001 (2014).

[106] G. Jabbari, S. Klaiman, Y.-C. Chiang, F. Trinter, T. Jahnke, and K. Gokhberg, J. Chem. Phys. **140**, 224305 (2014).

[107] L. S. Cederbaum and F. Tarantelli, J. Chem. Phys. **98**, 9691 (1993).

[108] L. S. Cederbaum and F. Tarantelli, J. Chem. Phys. **99**, 5871 (1993).

[109] E. Pahl, L. S. Cederbaum, and F. Tarantelli, Phys. Rev. A **60**, 1070 (1999).

[110] E. Pahl, J. Brand, L. S. Cederbaum, and F. Tarantelli, Phys. Rev. A **60**, 1079 (1999).

[111] S. Scheit, L. S. Cederbaum, and H.-D. Meyer, J. Chem. Phys. **118**, 2092 (2003).

[112] S. Scheit, V. Averbukh, H.-D. Meyer, N. Moiseyev, R. Santra, T. Sommerfeld, J. Zobeley, and L. S. Cederbaum, J. Chem. Phys. **121**, 8393 (2004).

[113] S. Scheit, Ph.D. thesis, Ruprecht-Karls-Universität Heidelberg (2007).

[114] Y.-C. Chiang, Ph.D. thesis, Ruprecht-Karls-Universität Heidelberg (2012).

[115] E. Pahl, H.-D. Meyer, and L. S. Cederbaum, Z. Phys. D **38**, 215 (1996).

[116] J. C. Fuggle and S. F. Alvarado, Phys. Rev. A **22**, 1615 (1980).

[117] C. Nicolas and C. Miron, J. Electron Spectrosc. Relat. Phenom. **185**, 267 (2012).

[118] P. V. Demekhin, S. Scheit, S. D. Stoychev, and L. S. Cederbaum, Phys. Rev. A **78**, 043421 (2008).

[119] Y.-C. Chiang, F. Otto, H.-D. Meyer, and L. S. Cederbaum, J. Chem. Phys. **136**, 114111 (2012).

[120] T. F. O'Malley, Phys. Rev. **150**, 14 (1966).

[121] J. N. Bardsley, J. Phys. B At. Mol. Opt. Phys. **1**, 349 (1968).

[122] L. S. Cederbaum and W. Domcke, J. Phys. B At. Mol. Opt. Phys. **14**, 4665 (1981).

[123] P. V. Demekhin, Y.-C. Chiang, S. D. Stoychev, P. Kolorenč, S. Scheit, A. I. Kuleff, F. Tarantelli, and L. S. Cederbaum, J. Chem. Phys. **131**, 104303 (2009).

[124] T. Jahnke, A. Czasch, M. S. Schöffler, S. Schössler, A. Knapp, M. Käsz, J. Titze, C. Wimmer, K. Kreidi, R. E. Grisenti, et al., Phys. Rev. Lett. **93**, 163401 (2004).

[125] N. Moiseyev, R. Santra, J. Zobeley, and L. S. Cederbaum, J. Chem. Phys. **114**, 7351 (2001).

[126] Y.-C. Chiang, F. Otto, H.-D. Meyer, and L. S. Cederbaum, J. Chem. Phys. **136**, 114111 (2012).

[127] A. W. K. Leung and W. H. Breckenridge, J. Chem. Phys. **111**, 9197 (1999).

[128] A. W. K. Leung, R. R. Julian, and W. H. Breckenridge, J. Chem. Phys. **110**, 8443 (1999).

[129] A. Leung, R. Julian, and W. Breckenridge, J. Chem. Phys. **111**, 4999 (1999).

[130] A. Kramida, Y. Ralchenko, J. Reader, and N. A. Team, NIST Atomic Spectra Database (version 5.1) (National Institute of Standards and Technology, Gaithersburg, MD) (2013), URL `http://physics.nist.gov/asd`.

[131] D. E. Woon and T. H. Dunning, Jr., J. Chem. Phys. **98**, 1358 (1993).

[132] The exponents of the diffuse s-functions are 0.0739 and 0.0234. The exponents of the d-functions are: 2.3300 and 7.3800 for the two compact d-functions, and 0.2330 and 0.0738 for the two diffuse d-functions.

[133] D. Woon and J. T. H. Dunning, J. Chem. Phys. **100**, 2975 (1994).

[134] M. W. Schmidt, K. K. Baldridge, J. A. Boatz, S. T. Elbert, M. S. Gordon, J. H. Jensen, S. Koseki, N. Matsunaga, K. A. Nguyen, S. Su, et al., J. Comp. Chem. **14**, 1347 (1993).

[135] A. W. K. Leung, J. G. Kaup, D. Bellert, J. G. McCaffrey, and W. H. Breckenridge, J. Chem. Phys. **111**, 2484 (1999).

[136] C. H. Greene, A. S. Dickinson, and H. R. Sadeghpour, Phys. Rev. Lett. **85**, 2458 (2000).

[137] P. Piecuch, S. A. Kucharski, K. Kowalski, and M. Musiał, Computer Phys. Comm. **149**, 71 (2002).

[138] K. Raghavachari, G. W. Trucks, J. A. Pople, and M. Head-Gordon, Chem. Phys. Lett. **157**, 479 (1989).

[139] T. Van Mourik and T. H. Dunning, Int. J. Quant. Chem. **76**, 205 (2000).

[140] A. K. Wilson, D. E. Woon, K. A. Peterson, and T. H. Dunning, Jr., J. Chem. Phys. **110**, 7667 (1999).

[141] P. R. Herman, P. E. Larocque, and B. P. Stoicheff, J. Chem. Phys. **89**, 4535 (1988).

[142] Y. Tanaka, K. Yoshino, and D. E. Freeman, J. Chem. Phys. **59**, 5160 (1973).

[143] B. R. Brooks and H. F. Schaefer, J. Chem. Phys. **70**, 5092 (1979).

[144] B. R. Brooks, W. D. Laidig, P. Saxe, N. C. Handy, and H. F. Schaefer III, Phys. Scr. **21**, 312 (1980).

[145] T. Miteva, S. Klaiman, E. V. Gromov, and K. Gokhberg, J. Chem. Phys. **140**, 204320 (2014).

[146] A. Nicklass, M. Dolg, H. Stoll, and H. Preuss, J. Chem. Phys. **102**, 8942 (1995).

[147] K. Kaufmann, W. Baumeister, and M. Jungen, J. Phys. B At. Mol. Opt. Phys. **22**, 2223 (1989).

[148] V. Averbukh, I. B. Müller, and L. S. Cederbaum, Phys. Rev. Lett. **93**, 263002 (2004).

[149] W. T. Pollard and R. A. Friesner, J. Chem. Phys. **100**, 5054 (1994).

[150] H.-D. Meyer, U. Manthe, and L. S. Cederbaum, Chem. Phys. Lett. **165**, 73 (1990).

[151] H.-D. Meyer, G. A. Worth, M. H. Beck, A. Jäckle, U. Manthe, M. Ehara, A. Raab, M.-C. Heitz, S. Sukiasyan, C. Cattarius, et al., The MCTDH Package, Version 8.4, See http://mctdh.uni-hd.de/ (2007).

[152] F. Trinter, J. B. Williams, M. Weller, M. Waitz, M. Pitzer, J. Voigtsberger, C. Schober, G. Kastirke, C. Müller, C. Goihl, et al., Phys. Rev. Lett. **111**, 093401 (2013).

[153] N. Sisourat, N. V. Kryzhevoi, P. Kolorenč, S. Scheit, T. Jahnke, and L. S. Cederbaum, Nat. Phys. **6**, 508 (2010).

[154] T. Ouchi, K. Sakai, H. Fukuzawa, I. Higuchi, P. V. Demekhin, Y.-C. Chiang, S. D. Stoychev, A. I. Kuleff, T. Mazza, M. Schöffler, et al., Phys. Rev. A **83**, 053415 (2011).

[155] R. G. Parr and R. G. Pearson, J. Am. Chem. Soc. **105**, 7512 (1983).

[156] M. Mantina, A. C. Chamberlin, R. Valero, C. J. Cramer, and D. G. Truhlar, J. Phys. Chem. A **113**, 5806 (2009).

[157] U. Hohm and K. Kerl, Mol. Phys. **69**, 803 (1990).

[158] K. I. Dmitrieva and G. I. Plindov, Phys. Scr. **27**, 402 (1983).

[159] T. Miteva, Y.-C. Chiang, P. Kolorenč, A. I. Kuleff, L. S. Cederbaum, and K. Gokhberg, J. Chem. Phys. **141**, 164303 (2014).

[160] E. Fasshauer, M. Pernpointner, and K. Gokhberg, J. Chem. Phys. **138**, 014305 (2013).

[161] Y. Neela, A. Mahadevi, and G. Sastry, Struct. Chem. **24**, 67 (2013).

[162] J. S. Rao, T. C. Dinadayalane, J. Leszczynski, and G. N. Sastry, J. Phys. Chem. A **112**, 12944 (2008).

[163] C. Lee, W. Yang, and R. G. Parr, Phys. Rev. B **37**, 785 (1988).

[164] A. D. Becke, J. Chem. Phys. **98**, 5648 (1993).

[165] A. D. Becke, J. Chem. Phys. **98**, 1372 (1993).

[166] A. D. McLean and G. S. Chandler, J. Chem. Phys. **72**, 5639 (1980).

[167] M. J. Frisch, G. W. Trucks, H. B. Schlegel, G. E. Scuseria, M. A. Robb, J. R. Cheeseman, G. Scalmani, V. Barone, B. Mennucci, G. A. Petersson, et al., Gaussian 09 Revision D.01, Gaussian Inc. Wallingford CT 2009.

[168] H. Ohtaki and T. Radnai, Chem. Rev. **93**, 1157 (1993).

[169] J. Wenzel, M. Wormit, and A. Dreuw, J. Comp. Chem. **35**, 1900 (2014).

[170] J. Wenzel, M. Wormit, and A. Dreuw, J. Chem. Theory Comput. **10**, 4583 (2014).

[171] M. Wormit, D. R. Rehn, P. H. Harbach, J. Wenzel, C. M. Krauter, E. Epifanovsky, and A. Dreuw, Mol. Phys. **112**, 774 (2014).

[172] Y. Shao, Z. Gan, E. Epifanovsky, A. T. Gilbert, M. Wormit, J. Kussmann, A. W. Lange, A. Behn, J. Deng, X. Feng, et al., Mol. Phys. **113**, 184 (2015).

[173] V. Stumpf (private communication).

[174] D. E. Woon and T. H. Dunning, J. Chem. Phys. **103**, 4572 (1995).

[175] Baig, M. A., Mahmood, S., Kalyar, M. A., Rafiq, M., Amin, N., and Haq, S. U., Eur. Phys. J. D **44**, 9 (2007).

[176] L. Ahrens, Geochim. Cosmochim. Acta **2**, 155 (1952).

[177] F. Merkt, Ann. Rev. Phys. Chem. **48**, 675 (1997).

[178] M. B. Robin, Higher Excited States of Polyatomic Molecules, vol. I (Academic Press, New York and London, 1974).

[179] T. Miteva, Y.-C. Chiang, P. Kolorenč, A. I. Kuleff, K. Gokhberg, and L. S. Cederbaum, J. Chem. Phys. **141**, 064307 (2014).

[180] F. Tarantelli, Chem. Phys. **329**, 11 (2006).